

UNIVERSITY OF LIVERPOOL

**Electrochemical and surface study of  
lithium-rich transition metal oxides used  
as cathodes in lithium-ion batteries**

---

*Thesis submitted in accordance with the requirements of the University of  
Liverpool for the Degree of Doctor in Philosophy*

José Antonio Coca Clemente

August 2019

Supervisors: Professor Laurence J. Hardwick and  
Professor Vin Dhanak



## **Abstract**

Lithium-ion (Li-ion) batteries are the present state-of-the-art energy storage technology used in mobile phones and electric vehicles. This thesis focuses on different lithium intercalation compounds that can be used as Li-ion cathode materials in order to improve the electrochemical performance of lithium-ion batteries, with particular focus on the study of Li-rich mixed metal oxides, where oxygen is a fundamental part of the redox activity of these compounds.

A general background about Li-ion batteries is presented in Chapter 1 and a detailed explanation of the experimental methods, specially focused on X-ray photoelectron spectroscopy (XPS), is explained within Chapter 2.

Chapter 3 of this thesis investigates how the effect of synthesis route of lithium manganese mixed metal oxides, with the formula  $\text{LiNi}_{1-x-y}\text{Co}_x\text{Mn}_y\text{O}_2$ , can affect the electrochemical performance of the material. Four  $\text{LiNi}_{1/3}\text{Co}_{1/3}\text{Mn}_{1/3}\text{O}_2$  samples were synthesised using two synthetic methods: resorcinol-formaldehyde sol-gel polymerisation and hydroxide co-precipitation synthesis; these four samples were compared with a commercial sample. Using XPS, Raman and scanning electron microscopy, a direct relationship between the particle size and the electrochemical performance, as well as the link between the used synthetic method and the surface reactivity was shown.

Chapter 4 studies the electrochemical behaviour of two Li-rich transition metal oxides:  $\text{Li}_{1.2}\text{Ni}_{0.13}\text{Mn}_{0.54}\text{Co}_{0.13}\text{O}_2$  and  $\text{Li}_{1.2}\text{Ni}_{0.32}\text{Mn}_{0.4}\text{Co}_{0.08}\text{O}_2$ . The anionic redox activity and the formation of  $\text{O}^{\text{n-}}$  species is shown via XPS and Raman spectroscopy at different

voltages, and show the importance of the oxygen redox activity in order to obtain a high electrochemical performance.

In Chapter 5, Li-rich intercalation compounds with rock-salt type structures with the general formula of  $\text{Li}_{4+x}\text{Ni}_{1-x}\text{WO}_6$  is reported, where a third-row transition metal is used in order to stabilise the structure. In this chapter, the studied material is the non-stoichiometric  $\text{Li}_{4.15}\text{Ni}_{0.85}\text{WO}_6$  and a detailed study in XPS and Raman at different voltages shows the formation of stable peroxo-type species that can explain the high capacity obtained, as well as the observed large voltage hysteresis ( $> 2.0$  V) that is characteristic of this material.

## **Acknowledgments**

I would like to thank Prof. Laurence Hardwick and Prof. Vin Dhanak for their support and guidance throughout my thesis, as well as all the current and past members of the Hardwick's group for their help and guidance during my PhD, and my mentors and special colleagues in the lab: Dr Laura Cabo-Fernández, Dr Nick Drewett, Dr David Hesp, Dr Christopher Sole and Dr Filipe Braga; nothing of this would have been possible without you guys. I also like to thank to Prof. Matthew Rosseinsky's group, especially to Dr Zoe Taylor, Dr Michael Pitcher and Dr Arnaud Perez for letting me be part of a great project, and Jack Swallow and Leanne Jones in their help in some of the last measurements during my PhD and the long drive to Diamond.

Special thanks to all the people that form (and have formed) part of the Stephenson Institute for Renewable Energy; thanks to Stefano Mensa for accompany me in the long hours of teaching and lab demonstrations and for being a great flat mate, and to Julia Fernández for keeping on with the Spanish legacy in the University of Liverpool.

To Carmen, who always was there for a walk around Liverpool and to go for a pint and nice burgers.

To my football mates, I already miss to play with them.

To all my friends in Spain that were supporting me 2000 kilometers away, specially to Fernando, Carlos and Nadja.

To my new mates from CIC Energigune, that are helping me a lot with this new period of my life in Spain.

To Pablo and Heike, who are great hosts and friends.

To my family, who they always were supporting me in happy and difficult moments.

*In beloved memory to my brother Pedro and my grandmother Isabel.*

## **Contents**

Abstract.....	i
Acknowledgments .....	iii
List of Figures .....	ix
List of Tables .....	xiii
Abbreviations.....	xiv
<b>Chapter 1. Introduction .....</b>	<b>1</b>
1.1. Overview of the chapter.....	1
1.2. The Li-ion cell .....	2
1.3. Lithium intercalation compounds used as cathode materials .....	6
1.3.1. Layered structures .....	8
1.3.2. Manganese spinel cathodes .....	10
1.3.3. Phospho-olivine cathodes.....	11
1.4. Lithium-rich compounds and the anionic redox behaviour .....	12
1.5. The importance of the surface behaviour in Li-ion batteries.....	16
1.6. Summary and outlook for thesis .....	18
1.7. References.....	21
<b>Chapter 2. Experimental Methods.....</b>	<b>29</b>
2.1. Overview of the chapter.....	29

2.2. Electrochemical characterisation techniques .....	30
2.2.1. Galvanostatic cycling .....	30
2.2.2. Differential capacity .....	33
2.2.3. Factors that can affect the electrochemical measurements .....	34
2.2.4. Cell components.....	36
2.2.5. Cleaning cycled electrodes.....	38
2.3. Structural characterisation techniques .....	38
2.3.1. X-Ray Photoelectron Spectroscopy (XPS) .....	39
2.3.2. Hard X-Ray Photoelectron Spectroscopy .....	58
2.3.3. Raman microscopy .....	61
2.3.4. X-ray diffraction.....	63
2.3.5. X-ray absorption spectroscopy.....	63
2.3.6. Scanning electron microscopy .....	65
2.3.7. Inductively couple plasma optical emission spectroscopy.....	65
2.3.8. Nitrogen adsorption/desorption isotherms .....	66
2.4. Preparation of the samples .....	67
2.5. References.....	71

<b>Chapter 3. Effect of the synthetic routes on the surface properties and electrochemical performance of <math>\text{LiNi}_{1-x-y}\text{Co}_x\text{Mn}_y\text{O}_2</math>.....</b>	<b>76</b>
---	-----------



3.1. Overview of the chapter.....	76
3.2. Introduction.....	77
3.3. Results.....	78
3.3.1. Crystal structure and morphology .....	78
3.3.2. Electrochemical Properties.....	83
3.3.3. Strength of M-O vibration bonds .....	86
3.3.4. Surface behaviour and its relationship with the synthetic method.....	87
3.4. Discussion.....	92
3.5. Conclusions.....	95
3.6. References.....	97

#### **Chapter 4. Electrochemical and surface behaviour for Li-rich row 1 transition**

<b>metal oxides.....</b>	<b>101</b>
4.1. Overview of the chapter.....	101
4.2. Introduction.....	102
4.3. Results.....	103
4.3.1. Crystal structure and morphology .....	103
4.3.2. Electrochemical Properties.....	106
4.3.3. Surface behaviour and anion redox reactions .....	110
4.3.4. Raman measurements and formation of O <sup>n-</sup> in the bulk.....	113

4.4. Discussion.....	116
4.5. Conclusions.....	119
4.6. References.....	120
<b>Chapter 5. Electrochemical and surface behaviour of Li-rich nickel tungsten oxides .....</b>	<b>123</b>
5.1. Overview of the chapter.....	123
5.2. Introduction.....	124
5.3. Results.....	125
5.3.1. Electrochemical properties .....	125
5.3.2. Charge compensation mechanism .....	129
5.3.3. Formation of stable O-O bonds .....	144
5.4. Discussion .....	147
5.5. Conclusions.....	149
5.6. References.....	150
<b>Chapter 6. Conclusions and further work.....</b>	<b>152</b>
<b>CURRICULUM VITAE .....</b>	<b>157</b>

## **List of Figures**

**Figure 1.1.** Schematic of the electrochemical process in a typical commercial battery during charge and discharge.

**Figure 1.2.** Schematic representation of layered  $\text{LiNi}_{1-x-y}\text{Co}_x\text{Mn}_y\text{O}_2$ .

**Figure 1.3.** Schematic representation of  $\text{LiMn}_2\text{O}_4$  spinels.

**Figure 1.4.** Schematic representation of  $\text{LiFePO}_4$ .

**Figure 1.5.** Schematic representation of  $\text{Li}_2\text{IrO}_3$ .

**Figure 2.1.** Electrochemical measurements of  $\text{LiCo}_{1/3}\text{Ni}_{1/3}\text{Mn}_{1/3}\text{O}_2$  using (a) continuous and (b) cyclic galvanostatic cycling. Graph (c) represents the cyclability of  $\text{LiCo}_{1/3}\text{Ni}_{1/3}\text{Mn}_{1/3}\text{O}_2$  at different C-rates.

**Figure 2.2.** Example of differential capacity plot of  $\text{LiCo}_{1/3}\text{Ni}_{1/3}\text{Mn}_{1/3}\text{O}_2$ .

**Figure 2.3.** (a) Process of making a coin cell. (b) Assembled Swagelok cell. (c) Ar-filled glovebox.

**Figure 2.4.** (a) Schematic of how the photoemission works. (b) Relative band levels and Fermi-level alignment between sample and analyser. (c) Picture of the X-ray photoelectron spectrometer used in the laboratory.

**Figure 2.5.** (a) X-ray gun. (b) Aluminium foil that covers the gun.

**Figure 2.6.** Doublet separation of Ni 2p of one of the studied materials ( $\text{Li}_{4.15}\text{Ni}_{0.85}\text{WO}_6$ ).

**Figure 2.7.** XPS survey spectrum of manganese acetate measured using two different anodes: Al  $\text{K}\alpha_1$  and Mg  $\text{K}\alpha_1$ .

**Figure 2.8.** XPS spectrum of C1s peak of a typical analysed electrode with the presence of different species and different type of bonds.

**Figure 2.9.** (a) XPS spectra of C1s with the observation of adventitious carbon in the surface of pure Li foil. (b) XPS spectra of C1s after sputtering of the surface of Li foil.

**Figure 2.10.** (a) Transfer chamber with its different components and (b) once it is connected to XPS. (c) Isolation valve when is open and (d) closed.

**Figure 2.11.** (a) Calculated inelastic mean free path. (b) Schematic view of XPS probe depths estimated for the O1s core peak at increasing photon energies.

**Figure 2.12.** Example of measured HAXPES spectra for a studied material ( $\text{Li}_{4.15}\text{Ni}_{0.85}\text{WO}_6$ ) with a kinetic energy up to 6 keV.

**Figure 2.13.** Example of Raman spectrum of  $\text{LiCo}_{1/3}\text{Ni}_{1/3}\text{Mn}_{1/3}\text{O}_2$ .

**Figure 2.14.** Example of X-ray absorption near-edge structure of different W-based compounds.

**Figure 3.1.** PXRD patterns of the different samples and their comparison with the literature standard.

**Figure 3.2.** SEM images of the particles prepared by the different synthetic routes.

**Figure 3.3.** Comparison of the electrochemical performance of the studied materials.

**Figure 3.4.** Raman spectra of the different measured samples where the vibration bonds are represented.

**Figure 3.5.** Survey scan of the different samples in XPS.

**Figure 3.6.** Comparison of XPS spectrum from the different samples where their core-level peaks are shown: a) Ni  $2p_{3/2}$ , b) Co  $2p_{3/2}$ , c) Mn  $2p_{3/2}$  and d) O 1s.

**Figure 4.1.** Schematic representation of  $\text{Li}_{1.2}\text{Ni}_{0.13}\text{Mn}_{0.54}\text{Co}_{0.13}\text{O}_2$ .

**Figure 4.2.** SEM images of the samples prepared via sol-gel synthetic route: a)  $\text{Li}_{1.2}\text{Ni}_{0.13}\text{Mn}_{0.54}\text{Co}_{0.13}\text{O}_2$  and b)  $\text{Li}_{1.2}\text{Ni}_{0.32}\text{Mn}_{0.4}\text{Co}_{0.08}\text{O}_2$ .

**Figure 4.3.** A comparison of X-ray diffraction spectrum between the studied samples.

**Figure 4.4.** Comparison of the cyclability at a constant C-rate of 100 mA g<sup>-1</sup> and a variation of C-rate every 10 cycles and the differential capacity for (a) Li<sub>1.2</sub>Ni<sub>0.13</sub>Mn<sub>0.54</sub>Co<sub>0.13</sub>O<sub>2</sub>, (b) Li<sub>1.2</sub>Ni<sub>0.32</sub>Mn<sub>0.4</sub>Co<sub>0.08</sub>O<sub>2</sub> and (c) LiNi<sub>1/3</sub>Mn<sub>1/3</sub>Co<sub>1/3</sub>O<sub>2</sub>.

**Figure 4.5.** Comparison between first and second charge / discharge process and the expected loss of Li atoms in the stoichiometry of the material after the first two cycles for (a) Li<sub>1.2</sub>Ni<sub>0.13</sub>Mn<sub>0.54</sub>Co<sub>0.13</sub>O<sub>2</sub> and (b) Li<sub>1.2</sub>Ni<sub>0.32</sub>Mn<sub>0.4</sub>Co<sub>0.08</sub>O<sub>2</sub>.

**Figure 4.6.** X-ray photoelectron spectroscopy data collected at O 1s energies in the first two charge / discharge cycles of (a) Li<sub>1.2</sub>Ni<sub>0.13</sub>Mn<sub>0.54</sub>Co<sub>0.13</sub>O<sub>2</sub> and (b) Li<sub>1.2</sub>Ni<sub>0.32</sub>Mn<sub>0.4</sub>Co<sub>0.08</sub>O<sub>2</sub>.

**Figure 4.7.** Variation of the oxidation state for O, Ni, Co and Mn for (a) Li<sub>1.2</sub>Ni<sub>0.13</sub>Mn<sub>0.54</sub>Co<sub>0.13</sub>O<sub>2</sub> and (b) Li<sub>1.2</sub>Ni<sub>0.32</sub>Mn<sub>0.4</sub>Co<sub>0.08</sub>O<sub>2</sub>.

**Figure 4.8.** *Ex situ* Raman spectra for the pristine electrodes of (a) Li<sub>1.2</sub>Ni<sub>0.13</sub>Mn<sub>0.54</sub>Co<sub>0.13</sub>O<sub>2</sub> and (b) Li<sub>1.2</sub>Ni<sub>0.32</sub>Mn<sub>0.4</sub>Co<sub>0.08</sub>O<sub>2</sub> and at different states of charge / discharge in the first two cycles for (c) Li<sub>1.2</sub>Ni<sub>0.13</sub>Mn<sub>0.54</sub>Co<sub>0.13</sub>O<sub>2</sub> and (d) Li<sub>1.2</sub>Ni<sub>0.32</sub>Mn<sub>0.4</sub>Co<sub>0.08</sub>O<sub>2</sub>.

**Figure 5.1.** The rock-salt structure of Li<sub>4.15</sub>Ni<sub>0.85</sub>WO<sub>6</sub> viewed along the [010] direction (a) and honeycomb-like ordering around W in the W/Ni-rich layer (b).

**Figure 5.2.** Electrochemical performance of Li<sub>4.15</sub>Ni<sub>0.85</sub>WO<sub>6</sub> as cathode material.

**Figure 5.3.** Differential capacity of the first two cycles and their difference in the redox processes.

**Figure 5.4.** Differential capacity plots of the voltage window opening experiment performed on Li<sub>4.15</sub>Ni<sub>0.85</sub>WO<sub>6</sub> with upper cut-off voltages of 4, 4.5 and 5 V.

**Figure 5.5.** X-ray absorption spectroscopy data of cycled Li<sub>4.15</sub>Ni<sub>0.85</sub>WO<sub>6</sub>.

**Figure 5.6.** X-ray photoemission spectroscopy data collected at O 1s and W 4f energies on the first two charge / discharge cycles of  $\text{Li}_{4.15}\text{Ni}_{0.85}\text{WO}_6$ .

**Figure 5.7.** O 1s and W 4f X-ray photoemission spectroscopy data collected on standard W compounds.

**Figure 5.8.** Evolution of oxidised oxygen  $\text{O}^{\text{n-}}$  (a) and oxidation state for the redox active centres (b) on the first two charge / discharge cycles of  $\text{Li}_{4.15}\text{Ni}_{0.85}\text{WO}_6$ .

**Figure 5.9.** Survey spectra of HAXPES measurements at (a) 2.1 keV and (b) 6.45 keV.

**Figure 5.10.** HAXPES data collected for O 1s using an energy of 2.1 keV and 6.45 keV on the first two charge / discharge cycles of  $\text{Li}_{4.15}\text{Ni}_{0.85}\text{WO}_6$ .

**Figure 5.11.** HAXPES data collected for W 4f using an energy of (a) 2.1 keV and (b) 6.45 keV on the first two charge / discharge cycles of  $\text{Li}_{4.15}\text{Ni}_{0.85}\text{WO}_6$ .

**Figure 5.12.** Evolution of oxidised oxygen  $\text{O}^{\text{n-}}$  (a) and oxidation state of oxygen (b) on the first two charge / discharge cycles of  $\text{Li}_{4.15}\text{Ni}_{0.85}\text{WO}_6$ .

**Figure 5.13.** HAXPES data collected for O 1s for (a) first and (b) second cycle and the evolution of oxidised oxygen  $\text{O}^{\text{n-}}$  (c) and oxidation state of oxygen (d) on the first two charge / discharge cycles of  $\text{Li}_{4.15}\text{Ni}_{0.85}\text{WO}_6$  in beamline P09 of PETRAIII (Hamburg, Germany).

**Figure 5.14.** Experimental Raman spectra of  $\text{WO}_2(\text{O}_2)\text{H}_2\text{O}$  (black) and its comparison with  $\text{Li}_{4.15}\text{Ni}_{0.85}\text{WO}_6$  charged at 5V (red).

**Figure 5.15.** *Ex situ* Raman spectra for different states of charge / discharge of  $\text{Li}_{4.15}\text{Ni}_{0.85}\text{WO}_6$ .

## **List of Tables**

**Table 2.1.** XPS spin-orbit doublet intensity ratios due to the electronic occupancy of the orbitals.

**Table 2.2.** Quantification of chemical bonds from C 1s deconvolution.

**Table 3.1.** Elemental analysis of the different  $\text{LiCo}_{1/3}\text{Ni}_{1/3}\text{Mn}_{1/3}\text{O}_2$  samples using ICP-OES.

**Table 3.2.** Cell parameters of the different  $\text{LiCo}_{1/3}\text{Ni}_{1/3}\text{Mn}_{1/3}\text{O}_2$  samples.

**Table 3.3.** A comparison between the surface area and porosity of the samples using BET measurements, as well as the approximate diameter of the particles measured in SEM.

**Table 3.4.** Percentage of contribution from the different species of Ni, Co and Mn observed in XPS for the different studied samples.

**Table 3.5.** Comparison of the pristine electrode and electrodes charged at 4.35 V and 4.6 V for the co-precipitation and sol-gel polymerisation samples.

**Table 4.1.** Elemental analysis of the different samples using ICP-OES.

**Table 4.2.** A comparison between the surface area and porosity of the samples using BET measurements, as well as the approximate diameter of the particles measured in SEM.

**Table 4.3.** Cell parameters of  $\text{Li}_{1.2}\text{Ni}_{0.13}\text{Mn}_{0.54}\text{Co}_{0.13}\text{O}_2$  and  $\text{Li}_{1.2}\text{Ni}_{0.32}\text{Mn}_{0.4}\text{Co}_{0.08}\text{O}_2$ .

**Table 4.4.** A comparison of the Raman shifts and percentage of area for the different measured bands in  $\text{Li}_{1.2}\text{Ni}_{0.13}\text{Mn}_{0.54}\text{Co}_{0.13}\text{O}_2$  and  $\text{Li}_{1.2}\text{Ni}_{0.32}\text{Mn}_{0.4}\text{Co}_{0.08}\text{O}_2$ .

## **Abbreviations**

BET – Brunauer-Emmett-Teller analysis

COM –  $\text{LiCo}_{1/3}\text{Ni}_{1/3}\text{Mn}_{1/3}\text{O}_2$ , commercial sample

CP –  $\text{LiCo}_{1/3}\text{Ni}_{1/3}\text{Mn}_{1/3}\text{O}_2$ , co-precipitation sample

DFT – Density functional theory

$E_B$  – Binding energy

$E_K$  – Kinetic energy

FWHM – Full width at half maximum

HAXPES – Hard X-ray photoelectron spectroscopy

ICP-OES – Inductively couple plasma optical emission spectroscopy

$\text{IMFP}_e$  – Inelastic mean free path

LIB – Lithium-ion battery

LRNMC151 –  $\text{Li}_{1.2}\text{Ni}_{0.13}\text{Mn}_{0.54}\text{Co}_{0.13}\text{O}_2$

LRNMC451 –  $\text{Li}_{1.2}\text{Ni}_{0.32}\text{Mn}_{0.4}\text{Co}_{0.08}\text{O}_2$

NMC111 –  $\text{LiCo}_{1/3}\text{Ni}_{1/3}\text{Mn}_{1/3}\text{O}_2$

PXRD – Powder x-ray diffraction

SEI – Solid-electrolyte interphase

SEM – Scanning electron microscopy

SG –  $\text{LiCo}_{1/3}\text{Ni}_{1/3}\text{Mn}_{1/3}\text{O}_2$ , sol-gel polymerisation sample

THF – Tetrahydrofuran

XANES – X-ray absorption near-edge structure

XPS – X-ray photoelectron spectroscopy

XRD – X-ray diffraction



# Chapter 1.

## Introduction

*“For Frodo.”*

Aragorn, son of Arathorn

*The Lord of the Rings: The Return of the King*

### 1.1. Overview of the chapter

Sony Corporation released the first commercial lithium-ion battery in 1991. Since then, secondary Li-ion batteries have played a major role in our day-to-day life as an essential part in electrical portable devices such as smartphones and laptops,<sup>1,2</sup> and the key of avoiding the production of greenhouse gases in electric vehicles with the present day example of Tesla Model S car with a driving range of 600 km.<sup>3</sup> The increasing demand of next-generation Li-ion batteries for the improvement in the functionality of mobile electronics and a better autonomy in both electric and hybrid vehicles requires an exhaustive research for new materials that can increase the capacity, charging rate and long life of the battery, and also improve the safety performance and reduces its price.

An intercalation reaction involves the insertion of guest species (in this case  $\text{Li}^+$ ) into normally unoccupied interstitial sites in the crystal structure of an existing stable host material. Lithium intercalation compounds that are candidate materials for the active electrode materials characteristically reversibly deintercalate and reintercalate  $\text{Li}^+$  in its

## ***Chapter 1. Introduction***

---

structure during an electrochemical process.

Normally, lithium intercalation compounds have a 1:1 Li:M ratio (where M is a transition metal such as Mn or Ni), and transition metals are the only redox-active elements. Lithium-rich intercalation compounds (special compounds where Li/M ratio is higher than 1) show additional redox transitions that were not observed before: anion redox; oxygen is an active component in this type of materials, increasing significantly the obtained capacity of them.<sup>4</sup>

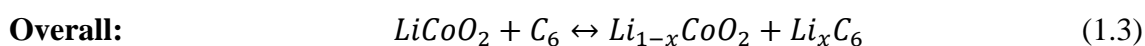
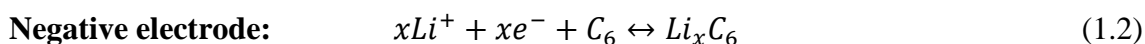
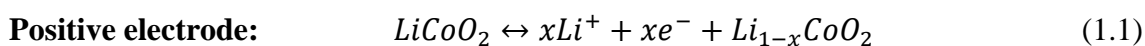
In this chapter, a description of rechargeable Li-ion batteries and a presentation of different lithium intercalation compounds as possible cathodic components in Li-ion batteries are described. A summary of the last years of research about anion redox and their importance in novel lithium intercalation compounds is also described. Finally, the importance of X-ray photoelectron spectroscopy (XPS) in the study of the surface of the electrodes is also discussed.

### **1.2. The Li-ion cell**

Li-ion cells are composed of two lithium intercalation materials, one of them used as positive electrode (cathode) and other as negative electrode (anode) separated by a separator impregnated with a non-aqueous electrolyte solution composed of an organic solvent and lithium salts (e.g. a solution of hexafluorophosphate,  $\text{LiPF}_6$ , in ethylene carbonate-diethyl carbonate), which enable ion transfer between the two electrodes. In the case of the commercial Li-ion battery introduced by Sony in 1991,<sup>5</sup> the positive electrode was a lithiated transition metal oxide ( $\text{LiCoO}_2$ ) and the negative electrode was graphite. Graphite replaced early cells that contained pure lithium metal due to safety issues such as dendrite formation consequently leading to short-circuit of the cell (and

even risk of explosion).<sup>6</sup>

Once these electrodes are connected externally, the electrochemical reactions proceed in tandem at both electrodes, with a cell potential of 3-4 V, thereby liberating electrons and enabling the current to be tapped by the user. An electrochemical reaction of a typical Li-ion cell (as shown in **Figure 1.1.**) during charge and discharge step can be described as follows:



During the charge process, an external current is applied (whereby electrons move through the external circuit from positive to negative electrode) causing  $Li^+$  ions to deintercalate from the positive electrode, diffusing into the electrolyte and migrating towards the negative electrode, maintaining charge neutrality due to the oxidation of the cathodic material; these  $Li^+$  ions are then intercalated into the negative electrode.

During the discharge process,  $Li^+$  ions are deintercalated from the negative electrode and diffused into the electrolyte.  $Li^+$  ions from the electrolyte are intercalated into the positive electrode and, to maintain charge neutrality, a corresponding number of electrons flow through the external circuit and the positive electrode is being reduced. This way electrical energy may be stored in both charge and discharge on demand by shuttling  $Li^+$  ions between positive and negative electrode. Consequently, the properties of a battery are highly dependent on the choice of its components.<sup>7-9</sup>

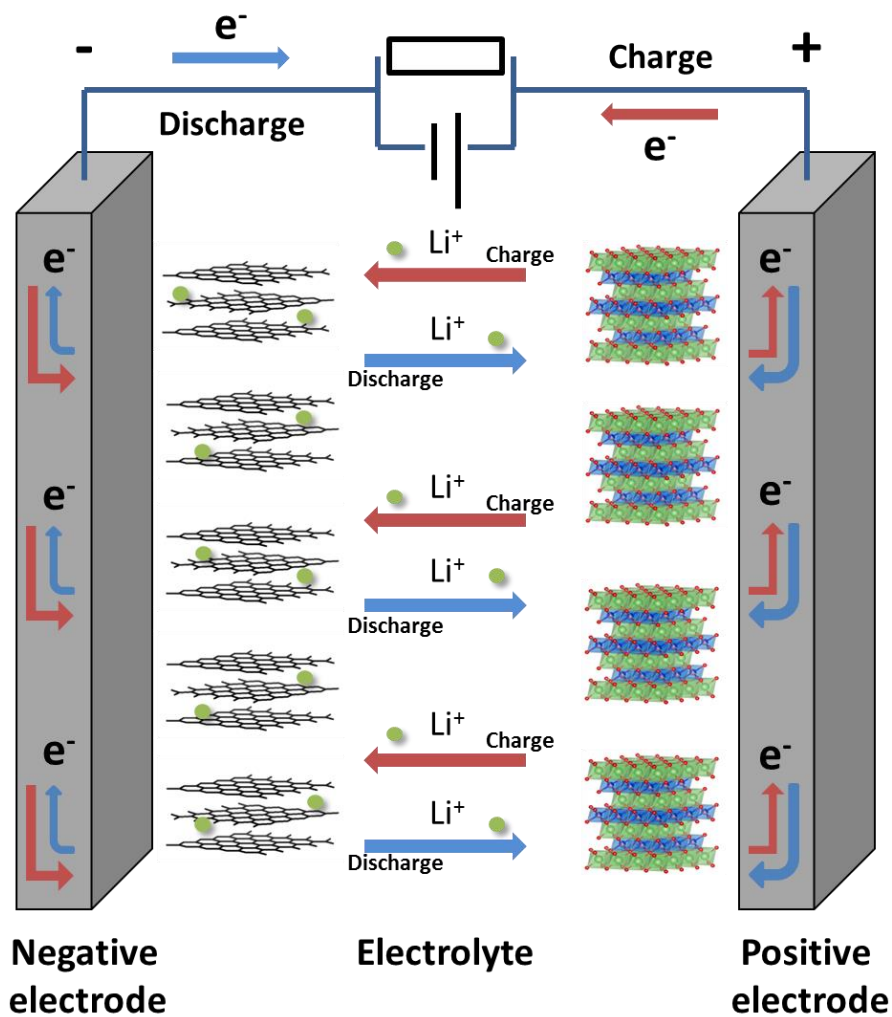


**Figure 1.1.** Schematic of the electrochemical process in a typical commercial battery during charge and discharge. During charge,  $Li^+$  ions deintercalate from the positive electrode ( $LiCoO_2$ ) and move to the negative electrode; the opposite way occurs during the discharge ( $Li_xC_6$ ).

Several cells can be integrated into a module and several modules can be integrated into a battery pack. An example of this could be the 85 kWh battery pack in a typical Tesla car, which consists in a pack that contains 7104 cells.<sup>3</sup>

The theoretical specific capacity ( $C_{specific}$ ,  $mAh\ g^{-1}$ ) of the active electrode materials measures the amount of charge that can be reversibly stored per unit mass and can be

estimated based on the electrochemical reactions involved in the charge / discharge processes according to the following equation:

$$C_{specific} = \frac{xF}{3.6nM} \quad (1.4)$$

where  $x$  is the number of electrons transferred in the electrochemical reaction involving the electrode,  $F$  is the Faraday's constant (96485 C mol<sup>-1</sup>),  $n$  is the number of moles of a chosen electroactive material that take place in the reaction, and  $M$  is the molecular weight of the same electroactive material.

Thus, for electric vehicles, decreasing the molar mass or increasing the number of moles of lithium is of considerable importance.

In the case of a commercial Li-ion battery, the theoretical specific capacity of the negative electrode (considering C<sub>6</sub>) can be calculated and its value is 372 mAh g<sup>-1</sup>. The cathodic reaction for LiCoO<sub>2</sub>, with a practical number of 0.5 electrons transferred (obtained experimentally),<sup>3, 10-12</sup> has a practical specific capacity of 137 mAh g<sup>-1</sup>.

Another important characteristic of Li-ion batteries is their high specific energy (energy per unit mass, Wh kg<sup>-1</sup>), and energy density (energy per unit volume, Wh L<sup>-1</sup>). The greater the energy density of the battery, the more energy may be stored or transported for the same amount of volume; this means that a high energy density allows to reduce the size of a battery, explaining why Li-ion batteries are widely used in small portable devices such as mobile phones.

A positive electrode with high electrochemical intercalation potential can be used to develop a high energy density battery with a given negative electrode. This is because the energy density of the device equals the product of the specific capacity of the electrode materials and the working voltage that is determined by the differential electrochemical potentials between the positive and negative electrode.<sup>13-15</sup>

## Chapter 1. Introduction

---

Cell voltage is determined by the compatibility of the whole system, including the anode, cathode, and electrolyte. In particular, the difference in electrochemical potential between the anode ( $\mu_A$ ) and the cathode ( $\mu_C$ ) is known as the open circuit potential (OCP, also known as working potential):

$$OCP = \frac{\mu_A - \mu_C}{e} \quad (1.5)$$

where  $e$  is the magnitude of the electronic charge. A big OCP means a good electrochemical performance. For Li-ion batteries, the usual value for OCP is ~4 V.

Usually, the positive electrode consists of a mix of the lithium metal oxide, a conductive carbon additive (which enhances the electrical contact between cathode material particles) and a binder (which is used to hold electrode components together). In order to estimate the specific capacity of a Li-ion battery is required, not only to take into consideration the positive electrode, but also binders, conductive additives, electrolyte, current collectors and packaging. Therefore, the practical energy density is always less than that estimated based on the battery chemistry.<sup>3</sup>

### 1.3. Lithium intercalation compounds used as cathode materials

Materials that are able to insert and remove ions are known as intercalation compounds, and this property makes them widely used as active electrode materials (like anodes and cathodes) in Li-ion batteries. Graphite is an ideal negative electrode material due to its low potential *vs.* Li/Li<sup>+</sup> of reaction and high capacity of 372 mAh g<sup>-1</sup> – although there is a wide research of other compounds in order to increase the anodic properties.<sup>16-</sup>  
<sup>18</sup> Intercalation compounds used as positive electrodes are the focus of the thesis. These are usually lithiated transition metal oxides with a characteristic structure that allows the facile insertion (intercalation) and extraction (deintercalation) of Li<sup>+</sup> ions.

The choice of cathode material is crucial in determining the performance of a Li-ion battery because of its importance during charge and discharge. The characteristics for cathode materials may be summarised as follows<sup>10, 19</sup>:

- Stability and safety.
- Contain a readily reducible / oxidisable ion (such as a transition metal).
- Material should possess no or reversible structural changes.
- High open circuit potential.
- Limited potential variation as function of  $\text{Li}^+$ .
- High gravimetric and volumetric capacity.
- High rate capability.
- To be stable with electrolyte with the operating limit of the potential.
- None or low toxicity.
- Low cost.

It is important to note that the choice of cathode material is influenced by the application for which the battery is intended, limiting the range of cathode materials that can be applied commercially in different devices.<sup>10, 20</sup> For example, the portable devices required small batteries with high energy density, while the hybrid vehicle batteries focussed on charge / discharge rates and cost.

Along the years, cathode materials with different metals and structures have been tested. The most common and well-known types are layered lithium transition metal oxides ( $\text{LiMO}_2$ ), lithium manganese spinels ( $\text{LiMn}_2\text{O}_4$ ) and olivines ( $\text{LiMPO}_4$ ), where  $M = \text{Co}, \text{Fe}, \text{Mn}, \text{Ni}, \text{etc.}$

### 1.3.1. Layered structures

The layered lithium transition metal oxides,  $\text{LiMO}_2$  ( $M = \text{Co}, \text{Ni}, \text{Mn}, \text{V}, \text{Cr}$  or  $\text{Fe}$ ) have an  $\alpha\text{-NaFeO}_2$  structure<sup>21</sup> which can be viewed as a distorted rock-salt structure consisting of layers of  $\text{Li}^+$  ions (where intercalation / deintercalation of the  $\text{Li}^+$  ions takes place) separating layers of  $[\text{MO}_6]^{n-}$  octahedra (see **Figure 1.2.**). The layered oxides are widely used as the positive electrodes in rechargeable batteries due to their ability to reversibly deintercalate / intercalate  $\text{Li}^+$  ions.<sup>22</sup>

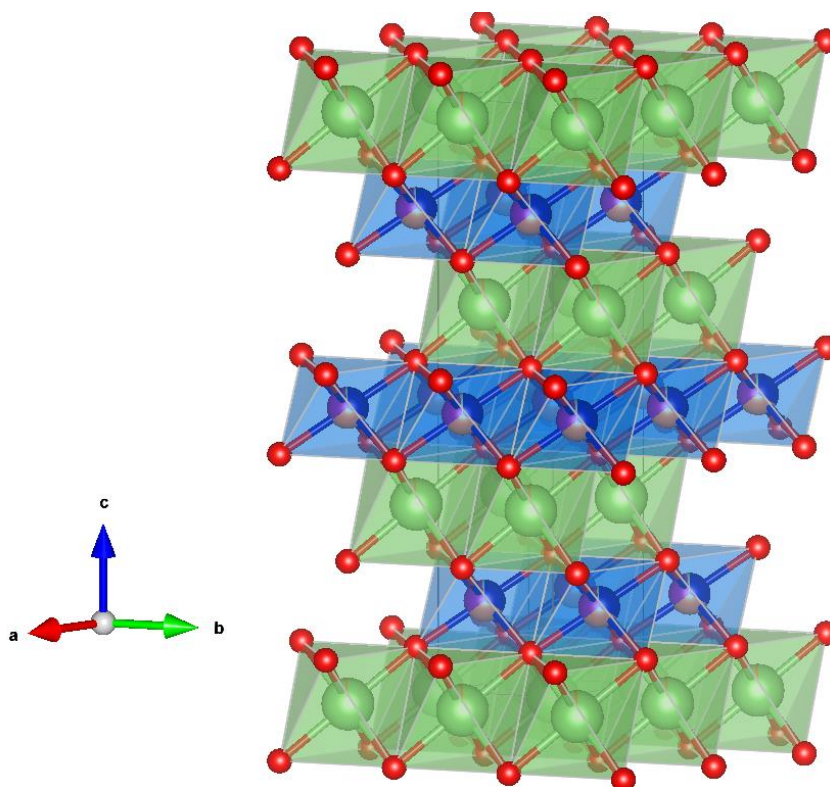


**Figure 1.2.** Schematic representation of layered  $\text{LiNi}_{1-x-y}\text{Co}_x\text{Mn}_y\text{O}_2$  with  $\alpha\text{-NaFeO}_2$  crystal structure type with space group  $R\bar{3}m$ , with alternating layer of edge-sharing  $\text{LiO}_6^-$  and  $\text{MO}_6^-$  octahedra. Li atoms (green), O atoms (red) and the combination of transition metals (blue, magenta and orange) are represented. In the case of layered  $\text{LiCoO}_2$  the structure is the same, with an atom of Co instead of a combination of Ni, Co and Mn atoms. Figure drawn using VESTA software based on a CIF file obtained from ICSD database (Code 171750) and the bibliography.<sup>23</sup>



LiCoO<sub>2</sub> is a main example of layered oxide and it is used within most of the commercial Li-ion cells. It has a practical specific capacity of 137 mAh g<sup>-1</sup>, which can be increased to 170 mAh g<sup>-1</sup> by the extension of the voltage window between 2.75 and 4.4 V vs. Li/Li<sup>+</sup>. Nevertheless, high material cost, toxicity and poor thermal stability encourage investigations into alternatives of it.

The isostructural LiNiO<sub>2</sub> is more attractive than LiCoO<sub>2</sub> as it is relatively cheap, less toxic and also has a more negative redox potential (0.25 V), making it less susceptible to oxidative electrolyte decomposition.<sup>24</sup> The LiNiO<sub>2</sub> has the same layered structure as LiCoO<sub>2</sub>, although it has a higher specific capacity (up to 200 mAh g<sup>-1</sup>)<sup>25</sup>. However, lithium and nickel ions have comparable ionic radii, making them easily interchangeable and leading to a greater degree of lithium/nickel disorder on cycling, impeding Li<sup>+</sup> ion mobility. This and other problems (such as its low thermal stability) mean that the LiNiO<sub>2</sub> is unsuitable as a cathode material. However, the introduction of cobalt can increase the thermal stability on a charge state and improve the structural stability. This has resulted in the development of more stable compounds with the stoichiometry Li(Ni<sub>1-x</sub>Co<sub>x</sub>)O<sub>2</sub>.

Another compound is LiNi<sub>0.5</sub>Mn<sub>0.5</sub>O<sub>2</sub>, which has advantages such as low cost and high discharge capacity, long cycling stability and thermal safety<sup>26-30</sup>. An additional property of LiNi<sub>0.5</sub>Mn<sub>0.5</sub>O<sub>2</sub> is that nickel in the system can undergo multi-electron transfer reaction – the material cycles between Ni<sup>2+</sup> and Ni<sup>4+</sup>, a two electron process – which provides a high degree of charge storage.

Since the first researches in 2003 from Yabuuchi *et al.*<sup>31</sup> and Koyama *et al.*,<sup>32</sup> researchers have focussed their attention on the combination of Co, Mn and Ni forming a series with the general formula LiNi<sub>1-x-y</sub>Mn<sub>x</sub>Co<sub>y</sub>O<sub>2</sub>, best known as NMC, which have been shown to be relatively stable and inexpensive,<sup>33, 34</sup> and they have demonstrated a

## Chapter 1. Introduction

---

good working voltage range (2.5 – 4.6 V vs. Li/Li<sup>+</sup>), theoretical capacity (278 mAh g<sup>-1</sup>) and practical gravimetric capacity (~200 mAh g<sup>-1</sup>), very good cyclability<sup>35</sup> and satisfactory structural and thermal stabilities.<sup>36,37</sup> The electrochemical properties of these series is related with the Ni:Mn:Co ratio, and usually a greater amount of Ni leads to a larger capacity.

### 1.3.2. Manganese spinel cathodes

The LiMn<sub>2</sub>O<sub>4</sub> material and its derivatives<sup>38-40</sup> attracted great interest due to high abundance, low cost, favourable charge density and stability when overcharged.<sup>25</sup> The LiMn<sub>2</sub>O<sub>4</sub> has spinel structure which has cubic closed-packed oxygen ions with *Fd3m* structure<sup>41</sup> as shown in **Figure 1.3**.

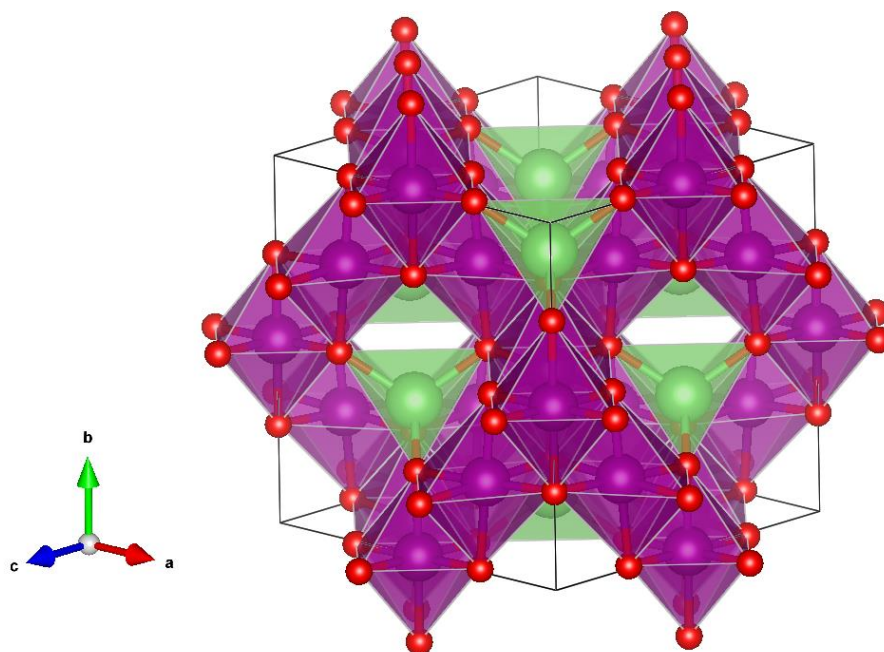


**Figure 1.3.** Schematic representation of LiMn<sub>2</sub>O<sub>4</sub> spinels with MgAl<sub>2</sub>O<sub>4</sub> crystal structure type with space group *Fd3m*, which cubic closed-packed oxygen ions. It is represented the Li atoms (green), O atoms (red) and Mn atoms (magenta). Figure drawn using VESTA software based on a CIF file obtained from ICSD database (Code 50415) and the bibliography.<sup>41</sup>

The disadvantages of the  $\text{LiMn}_2\text{O}_4$  are lower specific capacity and considerable problems in the storage and cycle life at high temperatures. The compound also undergoes a structural transformation during lithium intercalation – going from cubic  $\text{LiMn}_2\text{O}_4$  to tetragonal  $\text{Li}_2\text{Mn}_2\text{O}_4$  – which results in a loss of capacity.<sup>25</sup> However, advances have been made by discovering that capacity fading during cycling is primarily due to structural instability and Mn dissolution.<sup>42-44</sup>

### 1.3.3. Phospho-olivine cathodes

Recently, there has been a great interest in phospho-olivines ( $\text{LiMPO}_4$ , where  $\text{M} = \text{Fe}^{2+}, \text{Co}^{2+}, \text{Ni}^{2+}, \text{Mn}^{2+}$ ) as cathode materials. A commonly investigated material of this type is lithium iron phosphate ( $\text{LiFePO}_4$ ), considered to have very promising properties. The advantages of this material are that it is inexpensive, stable and nontoxic.<sup>45</sup>

However, the performance of the  $\text{LiFePO}_4$  is limited due to poor electrical conductivity of the active material. Consequently most recent research has focused on overcoming these problems using a wide range of techniques, such as reducing the particle size, doping the transition metal<sup>46, 47</sup> and producing small carbon coated  $\text{LiFePO}_4$  particles.<sup>48, 49</sup> An example of this structure is shown in **Figure 1.4**.

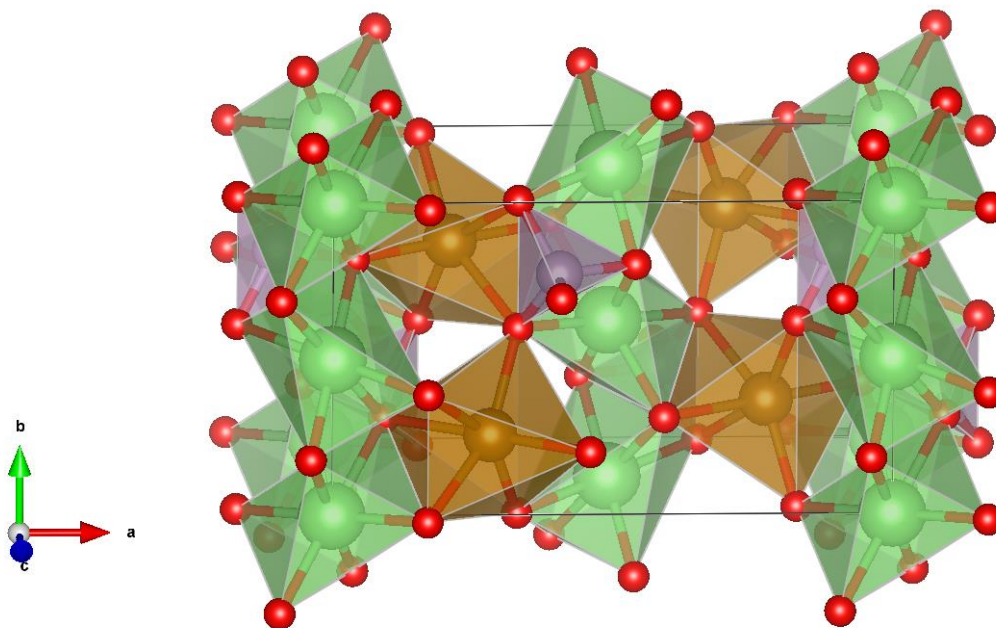


**Figure 1.4.** Schematic representation of  $\text{LiFePO}_4$  with orthorhombic  $\text{Mg}_2\text{SiO}_4$  crystal structure type with space group  $Pmnb$ . Gold structure represents the  $\text{FeO}_6$  octahedra, grey structure is the  $\text{PO}_4$  tetrahedra and Li atoms are represented in green. O atoms are represented in red. Figure drawn using VESTA software based on a CIF file obtained from ICSD database (Code 154117) and the bibliography.<sup>50</sup>

#### 1.4. Lithium-rich compounds and the anionic redox behaviour

Layered  $\text{LiMO}_2$  compounds can be considered as a progressive substitution of excess  $\text{Li}^+$  for  $\text{M}^{3+}$  in the  $[\text{MO}_2]$  layers, with a 1:1 Li:M ratio. A derivation from this type of compounds corresponds to a material with the general formula of  $\text{Li}(\text{Li}_{1/3}\text{M}_{2/3})\text{O}_2$ , alternatively noted  $\text{Li}_2\text{MO}_3$ , with conforms a “Li-rich” oxide (with  $\text{Li}/\text{M} > 1$ ). Among the numerous compounds with Li-rich  $\text{Li}_2\text{MO}_3$  structure type ( $\text{M} = \text{Mn}, \text{Ru}, \text{Ti}, \text{Zr}, \text{Sn}, \text{Pt} \dots$ ),  $\text{Li}_2\text{MnO}_3$  is the most studied so far. It exhibits an O3-type structure described in the monoclinic system (space group  $C2/m$ ) to take into account the distortion induced by the ordered distribution of the  $\text{Mn}^{4+}/\text{Li}^+$  cations in the mixed  $[\text{Li}_{1/3}\text{Mn}_{2/3}]\text{O}_2$  layer<sup>51</sup> so that  $\text{Li}^+$

ions are surrounded by six Mn atoms to form a honeycomb pattern.<sup>52-54</sup>

At first,  $\text{Li}_2\text{MnO}_3$  was considered to be inactive due to the charge of  $\text{Mn}^{4+}$  (considered impossible to be oxidised), but researchers discovered that using different treatments the electrochemical performance of  $\text{Li}_2\text{MnO}_3$  is superior to  $\text{LiMnO}_2$ .<sup>55, 56</sup>

Different investigations were focused on this material, in the most of the cases a combination of this compound with  $\text{LiMO}_2$  giving Li-rich compounds with a general formula of  $x\text{Li}_2\text{MnO}_3-(1-x)\text{LiMO}_2$  ( $M = \text{Mn, Ni, Co, Cr, Fe}$ ) was undergone. One of the most studied materials with this formula is  $0.5\text{Li}_2\text{MnO}_3-0.5\text{LiNi}_{1/3}\text{Mn}_{1/3}\text{Co}_{1/3}\text{O}_2$ , also written as  $\text{Li}_{1.2}\text{Ni}_{0.13}\text{Mn}_{0.54}\text{Co}_{0.13}\text{O}_2$ . These materials gave a different electrochemical profile than the classical  $\text{LiMO}_2$  compounds with capacities exceeding  $200\text{mAh g}^{-1}$ ,<sup>4</sup> and several theories were made in order to explain the relationship between crystal structure and electrochemical performance.<sup>57-60</sup> This resulted in a proposal of the anionic redox activity; in other words, oxygen is active for these type of materials, and it is taking place the oxidation of  $\text{O}^{2-}$  driving to the formation of peroxo-like species  $(\text{O}_2)^{n-}$  and charge compensating the extraction of  $\text{Li}^+$  ions by the removal of electrons from lattice oxygen; that allows to have more capacity than expected for this material.<sup>4, 61-63</sup>

Beyond the classical lithium intercalation compounds based on 3d metals, Tarascon *et al.*<sup>64, 65</sup> synthesised a different type of material using 4d metals and proposed the first experimental evidence for Li-driven reversible formation of peroxo-superoxo  $(\text{O}_2)^{n-}$  species in these materials with the synthesis of  $\text{Li}_2\text{Ru}_{1-y}\text{Sn}_y\text{O}_3$  (with that discover applied to  $\text{Li}_{1.2}\text{Ni}_{0.13}\text{Mn}_{0.54}\text{Co}_{0.13}\text{O}_2$  afterwards). On that basis, there is only a single redox active cation (Ru), and the high capacity of such materials is explained as due to cumulative cationic ( $\text{M}^{n+} \leftrightarrow \text{M}^{n+1} + e^-$ ) and anionic ( $2\text{O}^{2-} \leftrightarrow (\text{O}_2)^{n-} + ne^-$ ) reversible redox processes. The strong overlapping of the  $\text{M}(\text{nd})\text{-O}(\text{sp})$  bands is put forward as the driving force for

## Chapter 1. Introduction

---

Li-driven reversible formation of  $(\text{O}_2)^{n-}$  species in these materials.

The existence of anionic network redox activity with the formation of reversible  $(\text{O}_2)^{n-}$  species in intercalation compounds contributes to the production of high capacity than, otherwise, should be too much lower than actually is with the previously believed limit of  $1 e^-$  per transition metal. However, there are some issues derived from the anionic redox process, such as the evolution of gaseous  $\text{O}_2$  at high potential.<sup>57, 66</sup> Oxygen loss produces holes in the crystal structure of these materials,<sup>62</sup> therefore there is a great effort to study alternative  $\text{Li}_2\text{MO}_3$  based on 4d and even 5d metal cations that can avoid the formation of  $\text{O}_2$  gas;<sup>67, 68</sup> one example is  $\text{Li}_2\text{IrO}_3$ , which is widely studied nowadays.<sup>69, 70</sup>  $\text{Li}_2\text{IrO}_3$  has a rock-salt structure, which can be observed in **Figure 1.5**. The advantage of using 5d metals is because 5d orbitals are more spatially expanded and less correlated than 4d orbital, hence promoting covalence. Enhancing the covalence of the  $\text{LiM}_2$  layers via 5d metals helped to visualise the (O-O) peroxo-like dimmers for the first time.<sup>62</sup>

Over recent years, different studies have focused their attention on the combination of two different metal centres in its structure, usually in the same proportion. The general formula can therefore be considered as  $\text{Li}_2\text{M}_{0.5}\text{M}'_{0.5}\text{O}_3$  (where the sum of the oxidation states of these metal centres has to be equal to +4 in order to retain charge neutrality), or  $\text{Li}_4\text{MM}'\text{O}_6$  (where the sum of the oxidation states of the two metal centres in this case is equal to +8). Some examples of them are  $\text{Li}_4\text{MTeO}_6$  ( $\text{M}^{2+} = \text{Co}, \text{Ni}, \text{Cu}, \text{Zn}$ )<sup>71, 72</sup> and  $\text{Li}_4\text{MSbO}_6$  ( $\text{M}^{3+} = \text{Al}, \text{Cr}, \text{Ga}, \text{Fe}, \text{Mn}$ ).<sup>73, 74</sup> These structures retain the close-packed arrangement of oxygen ions with octahedrally coordinated metals forming an ordered honeycomb array, separated by a fully occupied lithium layer.

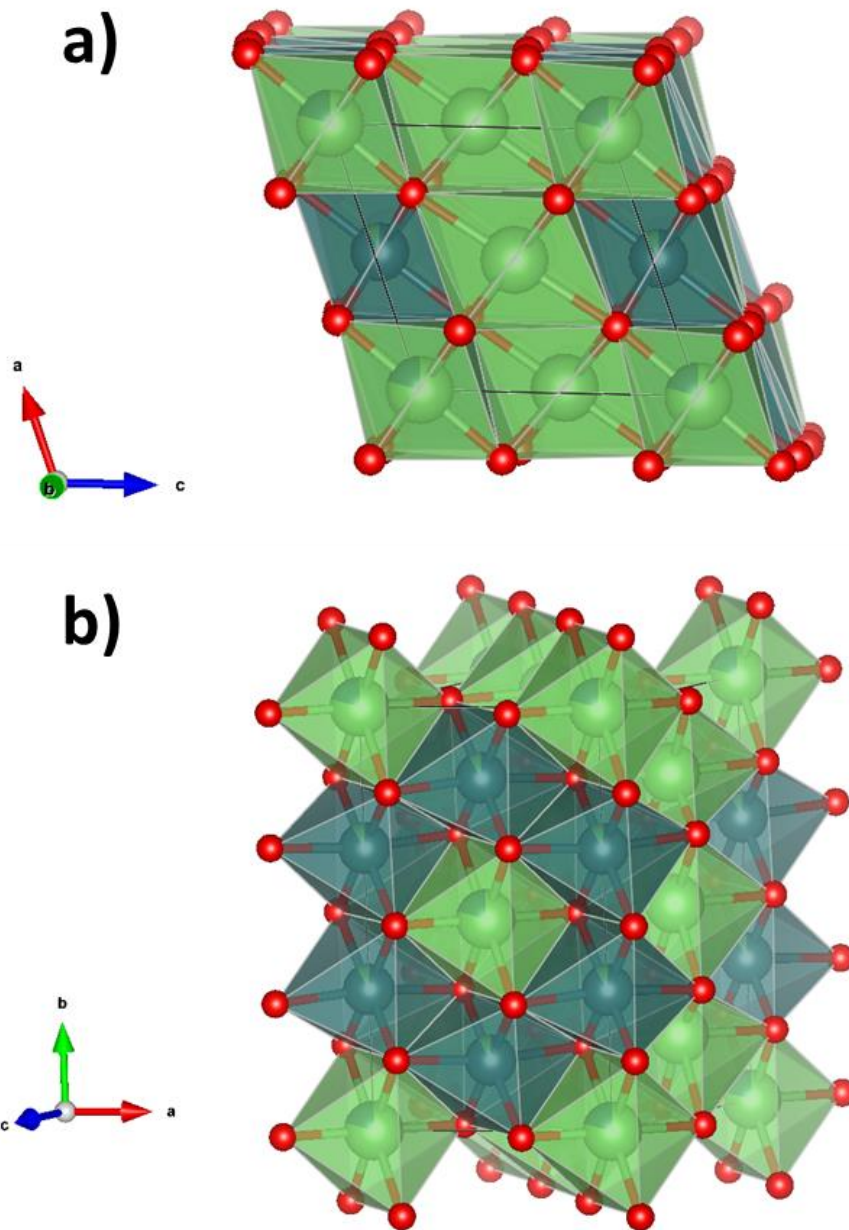


**Figure 1.5.** Schematic representation of  $\text{Li}_2\text{IrO}_3$  with  $\text{Na}_5\text{ReO}_6$  crystal structure type with space group  $C2/m$  of a)  $[010]$  direction and b) basal plane layer showing the honeycomb of edge-sharing  $\text{IrO}_6$  octahedra. Marine structure represents the  $\text{FeO}_6$  octahedra,  $\text{Li}$  atoms are represented in green and  $\text{O}$  atoms are represented in red. Figure drawn using VESTA software based on a CIF file obtained from ICSD database (Code 246025) and the bibliography.<sup>75</sup>

## Chapter 1. Introduction

---

Despite the big amount of these Li-rich compounds with rock-salt superstructures discovered in the last years, few of them have been studied electrochemically as possible cathodes in Li-ion batteries. The possible explanation of this is because of the presence of a high-valency heavy metal cation, which is redox inactive. However, some researchers such as McCalla *et al.*<sup>70</sup> studied the electrochemical behaviour of several Li-rich compounds with the presence of Ni in its structure in order to observe the evolution of the O-O peroxo-like dimers in lithium intercalation compounds; some examples are  $\text{Li}_4\text{NiTeO}_6$  and  $\text{Li}_4\text{NiMoO}_6$ .<sup>63, 76-78</sup> One of the observed problems inherent of these materials are a large hysteresis (difference in voltage between the charge and discharge process), where most of the discharge capacity is recovered below 2 V, being a recurrent problem in materials that show anionic redox activity.<sup>61, 79, 80</sup>

Although such low energy efficiency is counter-productive to their use in practical Li-ion batteries, understanding the origin of this feature will help in the design of future cathode materials.

### 1.5. The importance of the surface behaviour in Li-ion batteries

The most important electrochemical interactions take place at the interface between the electrolyte and cathode (and electrolyte and anode) where the  $\text{Li}^+$  ions move in one or another direction depending on if deintercalation or reintercalation is taking place (**Figure 1.1**). There are different issues that are happening in the surface of the lithium intercalation materials that can affect the obtained capacity of Li-ion batteries: i) a change in the structure of the lithium intercalation compound due to the deintercalation of  $\text{Li}^+$  ions; ii) the degradation of the electrolyte, forming a passivation layer in the surface of



the cathode known as *solid electrolyte interphase* (SEI);<sup>81-83</sup> iii) the adsorption of contaminants onto the surface that can affect the accessibility of Li<sup>+</sup> ions.<sup>84-86</sup>

Surface reactivity plays a major role in the capacity and cycle life of these materials. Understanding the surface chemistry is critical in developing synthetic methods that lead to greater materials to permit their future commercialisation.

Some characterisation techniques are very important in order to determinate the structure and the composition of the different cathode materials, and how they can be affected by electrochemical cycling or the exposure to air during the synthesis in the laboratory. One of the most important techniques is *X-ray photoelectron spectroscopy*, where the X-ray photons can only penetrate onto the first layers of the sample (1-2 nm) and any modification of the surface can affect the final result and the quantification of the peaks.<sup>87-91</sup>

X-ray photoelectron spectroscopy (XPS) can provide not only information about surface composition, such as presence of impurities and chemical functionalities, but also can study the chemical mapping to evaluate the surface structures or irregularities, near-surface variation of composition and surface aggregation.<sup>92</sup>

The application of the XPS technique on lithium intercalation compounds can help to understand the electrochemical reactivity, associated stability of electrochemical interfaces and their chemical states. It can also help to observe the change in the surface structure of these lithium intercalation compounds during charge and discharge processes, i.e. the deintercalation and reintercalation of Li<sup>+</sup> ions at the applied voltage, and the change in the oxidation state of the active redox centres in these compounds during charge compensation mechanism,<sup>62</sup> as well as the presence of any chemical species that was not taking into consideration beforehand.

## ***Chapter 1. Introduction***

---

Thus, XPS is a powerful surface technique that can be widely used among battery materials to study the composition and thickness of the passivation layer from SEI and other decomposition products that can affect the final capacity,<sup>82, 93-95</sup> as well as the presence of contaminants and any change in the structure of the lithium intercalation compounds used as positive and negative electrodes in Li-ion batteries.<sup>96-98</sup>

In the last decade of research regarding lithium-rich compounds led by Tarascon *et al.*,<sup>61, 99</sup> XPS turned out to be an important technique in observing the formation of  $(O_2)^{n-}$  species in this type of materials<sup>70</sup> and to discover that the active redox centres sometimes do not reach the expected oxidation state during the charge / discharge process, as it is going to be discussed further in this thesis.

Other important application of XPS is in the study of commercial batteries that present failures. Dismantling and analysing their components via XPS can help to obtain relevant chemical information and try to understand any important issue associated with these device failures that can be significant to industry.

### **1.6. Summary and outlook for thesis**

The electrochemical activity and reversibility of cathode materials in Li-ion batteries are dependant on the crystal structure and the surface behaviour. Li-rich compounds demonstrate higher specific capacities than typical lithium intercalation compounds due to anionic redox activity, where oxygen has a major role in its electrochemical behaviour and the total capacity of these type of materials, increasing their value more than expected initially.

The utilisation of different structural characterisation techniques is crucial in order to follow the chemical changes in these lithium intercalation materials during electrochemical cycling.

In this thesis, different electrochemical and structural characterisation techniques are applied, and their electrochemical behaviour during different potentials and cycles are widely discussed. The most readily used characterisation technique in this thesis is X-ray photoelectron spectroscopy in order to understand the surface behaviour of compounds of interest.

Various lithium intercalation compounds are studied, especially focused on Li-rich materials. In *Chapter 3*, different synthetic routes for  $\text{LiNi}_{1/3}\text{Mn}_{1/3}\text{Co}_{1/3}\text{O}_2$  were used to compare their capacity and try to find a link between their capacity and their morphology and surface properties. The use of different structural characterisation techniques was crucial in order to understand their electrochemical performance.

The synthetic method with better electrochemical results was used in *Chapter 4* to synthesise two different Li-rich materials with a general formula of  $0.5\text{Li}_2\text{MnO}_3\text{-}0.5\text{LiNi}_{1-x-y}\text{Mn}_x\text{Co}_y\text{O}_2$ . In the case of  $\text{Li}_{1.2}\text{Ni}_{0.13}\text{Mn}_{0.54}\text{Co}_{0.13}\text{O}_2$ , which is a very well-known Li-rich compound, presents a high capacity due to the oxidation of oxygen at high voltage, and therefore an exhaustive study of the material at different stages of charge and discharge was made using X-ray photoelectron spectroscopy. The electrochemical and surface properties were compared with  $\text{Li}_{1.2}\text{Ni}_{0.32}\text{Mn}_{0.4}\text{Co}_{0.08}\text{O}_2$ , which is also a Li-rich material with a similar stoichiometry and it was expected to have a similar electrochemical behaviour as well as surface properties.

In *Chapter 5*, a novel family of Li-rich intercalation compounds with rock-salt type structures with the general formula of  $\text{Li}_{4+x}\text{Ni}_{1-x}\text{WO}_6$  is reported. It is expected that the

## ***Chapter 1. Introduction***

---

use of a heavy metal cation ( $W^{6+}$ ) gives a high stabilisation of the material during cycling, and forming stable O-O bonds to achieve a high capacity. The electrochemical and surface study of the non-stoichiometric  $Li_{4.15}Ni_{0.85}WO_6$  was done in order to observe the evolution of oxygen and the formation of stable  $O^{n-}$  species at high voltages, especially focus on X-ray phototelectron spectroscopy. Additional studies with different synchrotron-based techniques were also carried out.

## 1.7. References

1. D. Deng, M. G. Kim, J. Y. Lee and J. Cho, *Energy Environ. Sci.*, 2009, **2**, 818-837.
2. H. Takeshita, *Proc. Conf. Power*, 2000.
3. D. Deng, *Energy Sci. Eng.*, 2015, **3**, 385-418.
4. P. Rozier and J. M. Tarascon, *J. Electrochem. Soc.*, 2015, **162**, A2490-A2499.
5. T. Nagaura and K. Tozawa, *Prog. Batteries Solar Cells*, 1990, **9**, 209.
6. M. M. Thackeray, C. Wolverton and E. D. Isaacs, *Energy Environ. Sci.*, 2012, **5**, 7854-7863.
7. D. Linden and T. Reddy, *Handbook of Batteries*, McGraw-Hill, 2002.
8. K. E. Aifantis, S. A. Hackney and R. V. Kumar, *High energy density lithium batteries*, John Wiley & Sons, 2010.
9. M. Armand and J.-M. Tarascon, *Nature*, 2008, **451**, 652-657.
10. M. S. Whittingham, *Chem. Rev.*, 2004, **104**, 4271-4302.
11. K. Mizushima, P. Jones, P. Wiseman and J. Goodenough, *Mater. Res. Bull.*, 1980, **15**, 783-789.
12. G. Amatucci, J. Tarascon and L. Klein, *J. Electrochem. Soc.*, 1996, **143**, 1114-1123.
13. A. K. Padhi, K. S. Nanjundaswamy and J. B. Goodenough, *J. Electrochem. Soc.*, 1997, **144**, 1188-1194.
14. J. B. Goodenough, *Acc. Chem. Res.*, 2012, **46**, 1053-1061.
15. J. B. Goodenough and K.-S. Park, *J. Am. Chem. Soc.*, 2013, **135**, 1167-1176.
16. M. Li, W. Wang, M. Yang, F. Lv, L. Cao, Y. Tang, R. Sun and Z. Lu, *RSC Adv.*, 2015, **5**, 7356-7362.

## Chapter 1. Introduction

---

17. W. J. Lee, T. H. Hwang, J. O. Hwang, H. W. Kim, J. Lim, H. Y. Jeong, J. Shim, T. H. Han, J. Y. Kim and J. W. Choi, *Energy Environ. Sci.*, 2014, **7**, 621-626.
18. F. Lyu, Z. Sun, B. Nan, S. Yu, L. Cao, M. Yang, M. Li, W. Wang, S. Wu, S. Zeng, H. Liu and Z. Lu, *ACS Appl. Mater. Interfaces*, 2017, **9**, 10699-10707.
19. G.-A. Nazri and G. Pistoia, *Lithium batteries: science and technology*, Springer Science, 2008.
20. M. Winter, K. Moeller, J. Besenhard, G. Nazri and G. Pistoia, *Lithium batteries: science and technology*, Springer Science, 2004, **148**.
21. J. Akimoto, Y. Gotoh and Y. Oosawa, *J. Solid State Chem.*, 1998, **141**, 298-302.
22. F. Gamble, J. Osiecki, M. Cais, R. Pisharody, F. DiSalvo and T. Geballe, *Science*, 1971, **174**, 493-497.
23. S. C. Yin, Y. H. Rho, I. Swainson and L. F. Nazar, *Chem. Mater.*, 2006, **18**, 1901-1910.
24. S. Campbell, C. Bowes and R. McMillan, *J. Electroanal. Chem. Interfacial Electrochem.*, 1990, **284**, 195-204.
25. A. Patil, V. Patil, D. W. Shin, J.-W. Choi, D.-S. Paik and S.-J. Yoon, *Mater. Res. Bull.*, 2008, **43**, 1913-1942.
26. T. Ohzuku and Y. Makimura, *Chem. Lett.*, 2001, 642-643.
27. Z. Lu, D. MacNeil and J. Dahn, *Electrochem. Solid-State Lett.*, 2001, **4**, A191-A194.
28. X.-Q. Yang, J. McBreen, W.-S. Yoon and C. P. Grey, *Electrochem. Commun.*, 2002, **4**, 649-654.
29. K. Shaju, G. S. Rao and B. Chowdari, *Electrochim. Acta*, 2002, **48**, 145-151.

30. J.-S. Kim, C. Johnson and M. Thackeray, *Electrochem. Commun.*, 2002, **4**, 205-209.
31. N. Yabuuchi and T. Ohzuku, *J. Power Sources*, 2003, **119**, 171-174.
32. Y. Koyama, I. Tanaka, H. Adachi, Y. Makimura and T. Ohzuku, *J. Power Sources*, 2003, **119**, 644-648.
33. E. Rossen, C. Jones and J. Dahn, *Solid State Ionics*, 1992, **57**, 311-318.
34. M. S. Islam, R. A. Davies and J. D. Gale, *Chem. Mater.*, 2003, **15**, 4280-4286.
35. R. Robert, C. Villeveille and P. Novák, *J. Mater. Chem. A*, 2014, **2**, 8589-8598.
36. S. K. Martha, H. Sclar, Z. S. Framowitz, D. Kovacheva, N. Saliyski, Y. Gofer, P. Sharon, E. Golik, B. Markovsky and D. Aurbach, *J. Power Sources*, 2009, **189**, 248-255.
37. C. S. Johnson, N. Li, C. Lefief, J. T. Vaughey and M. M. Thackeray, *Chem. Mater.*, 2008, **20**, 6095-6106.
38. L. C. Ferracin, F. A. Amaral and N. Bocchi, *Solid State Ionics*, 2000, **130**, 215-220.
39. M. M. Doeff, A. Anapolsky, L. Edman, T. J. Richardson and L. De Jonghe, *J. Electrochem. Soc.*, 2001, **148**, A230-A236.
40. S.-T. Myung, S. Komaba and N. Kumagai, *J. Electrochem. Soc.*, 2001, **148**, A482-A489.
41. H. Berg, J. O. Thomas, W. Liu and G. C. Farrington, *Solid State Ionics*, 1998, **112**, 165.
42. S. Patoux, L. Sannier, H. Lignier, Y. Reynier, C. Bourbon, S. Jouanneau, F. Le Cras and S. Martinet, *Electrochim. Acta*, 2008, **53**, 4137-4145.

## Chapter 1. Introduction

---

43. A. Butz, M. Wohlfahrt-Mehrens, R. Oesten and R. Huggins, *Ionics*, 1996, **2**, 405-411.
44. T. Kulova, E. Karseeva, A. Skundin, E. I. Kachibaya, R. Imnadze and T. Paikidze, *Russ. J. Electrochem.*, 2004, **40**, 494-499.
45. A. Manthiram, *Electrochem. Soc. Interface*, 2009, **18**, 44.
46. M. Thackeray, *Nat. Mater.*, 2002, **1**, 81-82.
47. K. Striebel, J. Shim, V. Srinivasan and J. Newman, *J. Electrochem. Soc.*, 2005, **152**, A664-A670.
48. A. Yamada, S.-C. Chung and K. Hinokuma, *J. Electrochem. Soc.*, 2001, **148**, A224-A229.
49. M. Takahashi, S. Tobishima, K. Takei and Y. Sakurai, *J. Power Sources*, 2001, **97**, 508-511.
50. C. Delacourt, J. Rodríguez-Carvajal, B. Schmitt, J.-M. Tarascon and C. Masquelier, *Solid State Sci.*, 2005, **7**, 1506-1516.
51. P. Strobel and B. Lambert-Andron, *J. Solid State Chem.*, 1988, **75**, 90-98.
52. J.-S. Kim, C. S. Johnson, J. T. Vaughey, M. M. Thackeray, S. A. Hackney, W. Yoon and C. P. Grey, *Chem. Mater.*, 2004, **16**, 1996-2006.
53. J. Bréger, M. Jiang, N. Dupré, Y. S. Meng, Y. Shao-Horn, G. Ceder and C. P. Grey, *J. Solid State Chem.*, 2005, **178**, 2575-2585.
54. Y. S. Meng, G. Ceder, C. P. Grey, W. S. Yoon, M. Jiang, J. Bréger and Y. Shao-Horn, *Chem. Mater.*, 2005, **17**, 2386-2394.
55. M. H. Rossouw and M. M. Thackeray, *Mater. Res. Bull.*, 1991, **26**, 463-473.
56. P. Kalyani, S. Chitra, T. Mohan and S. Gopukumar, *J. Power Sources*, 1999, **80**, 103-106.



57. Z. Lu and J. R. Dahn, *J. Electrochem. Soc.*, 2002, **149**, A815-A822.
58. H. Koga, L. Croguennec, M. Ménétrier, P. Mannesiez, F. Weill and C. Delmas, *J. Power Sources*, 2013, **236**, 250-258.
59. J. Cho, Y. J. Kim, T. J. Kim and B. Park, *Angew. Chem. Int. Ed.*, 2001, **113**, 3471-3473.
60. H. Koga, L. Croguennec, M. Ménétrier, K. Douhil, S. Belin, L. Bourgeois, E. Suard, F. Weill and C. Delmas, *J. Electrochem. Soc.*, 2013, **160**, A786-A792.
61. G. Assat, D. Foix, C. Delacourt, A. Iadecola, R. Dedryvère and J.-M. Tarascon, *Nat. Commun.*, 2017, **8**, 2219.
62. K. Luo, M. R. Roberts, R. Hao, N. Guerrini, D. M. Pickup, Y.-S. Liu, K. Edström, J. Guo, A. V. Chadwick and L. C. Duda, *Nat. Chem.*, 2016, **8**, 684.
63. D.-H. Seo, J. Lee, A. Urban, R. Malik, S. Kang and G. Ceder, *Nat. Chem.*, 2016, **8**, 692.
64. M. Sathiya, G. Rouse, K. Ramesha, C. P. Laisa, H. Vezin, M. T. Sougrati, M. L. Doublet, D. Foix, D. Gonbeau, W. Walker, A. S. Prakash, M. Ben Hassine, L. Dupont and J. M. Tarascon, *Nat. Mater.*, 2013, **12**, 827.
65. M. Sathiya, K. Ramesha, G. Rouse, D. Foix, D. Gonbeau, A. S. Prakash, M. L. Doublet, K. Hemalatha and J. M. Tarascon, *Chem. Mater.*, 2013, **25**, 1121-1131.
66. C. Johnson, J. Kim, C. Lefief, N. Li, J. Vaughey and M. Thackeray, *Electrochem. Commun.*, 2004, **6**, 1085-1091.
67. Y. Xie, M. Saubanere and M.-L. Doublet, *Energy Environ. Sci.*, 2017, **10**, 266-274.
68. H. Chen and M. S. Islam, *Chem. Mater.*, 2016, **28**, 6656-6663.

## Chapter 1. Introduction

---

69. P. E. Pearce, A. J. Perez, G. Rouse, M. Saubanère, D. Batuk, D. Foix, E. McCalla, A. M. Abakumov, G. Van Tendeloo, M.-L. Doublet and J.-M. Tarascon, *Nat. Mater.*, 2017, **16**, 580.
70. E. McCalla, A. M. Abakumov, M. Saubanère, D. Foix, E. J. Berg, G. Rouse, M.-L. Doublet, D. Gonbeau, P. Novák, G. Van Tendeloo, R. Dominko and J.-M. Tarascon, *Science*, 2015, **350**, 1516-1521.
71. V. Kumar, N. Bhardwaj, N. Tomar, V. Thakral and S. Uma, *Inorg. Chem.*, 2012, **51**, 10471-10473.
72. V. Nalbandyan, M. Avdeev and M. Evstigneeva, *J. Solid State Chem.*, 2013, **199**, 62-65.
73. E. Zvereva, *Dalton Trans.*, 2013, **42**, 1550.
74. N. Bhardwaj, A. Gupta and S. Uma, *Dalton Trans.*, 2014, **43**, 12050-12057.
75. M. J. O'Malley, H. Verweij and P. M. Woodward, *J. Solid State Chem.*, 2008, **181**, 1803-1809.
76. N. Yabuuchi, Y. Tahara, S. Komaba, S. Kitada and Y. Kajiya, *Chem. Mater.*, 2016, **28**, 416-419.
77. J. Lee, D.-H. Seo, M. Balasubramanian, N. Twu, X. Li and G. Ceder, *Energy Environ. Sci.*, 2015, **8**, 3255-3265.
78. M. Sathiya, K. Ramesha, G. Rouse, D. Foix, D. Gonbeau, K. Guruprakash, A. S. Prakash, M. L. Doublet and J. M. Tarascon, *Chem. Commun.*, 2013, **49**, 11376-11378.
79. J. R. Croy, M. Balasubramanian, K. G. Gallagher and A. K. Burrell, *Acc. Chem. Res.*, 2015, **48**, 2813-2821.

80. J. R. Croy, K. G. Gallagher, M. Balasubramanian, Z. Chen, Y. Ren, D. Kim, S.-H. Kang, D. W. Dees and M. M. Thackeray, *J. Phys. Chem. C*, 2013, **117**, 6525-6536.
81. P. Verma, P. Maire and P. Novák, *Electrochim. Acta*, 2010, **55**, 6332-6341.
82. K. Edström, T. Gustafsson and J. O. Thomas, *Electrochim. Acta*, 2004, **50**, 397-403.
83. V. A. Agubra and J. W. Fergus, *J. Power Sources*, 2014, **268**, 153-162.
84. C. Wagner, *J. Electron. Spectrosc. Relat. Phenom.*, 1980, **18**, 345-349.
85. T. L. Barr and S. Seal, *J. Vac. Sci. Technol. A*, 1995, **13**, 1239-1246.
86. S. Oswald, K. Nikolowski and H. Ehrenberg, *Anal. Bioanal. Chem.*, 2009, **393**, 1871-1877.
87. J. F. Watts, *Surface science techniques*, 1994, 5-23.
88. D. P. Woodruff, *Modern techniques of surface science*, Cambridge university press, 2016.
89. M. P. Seah and W. Dench, *Surf. Interface Anal.*, 1979, **1**, 2-11.
90. Y.-W. Chung, *Practical guide to surface science and spectroscopy*, Academic Press, 2001.
91. J. C. Vickerman and I. S. Gilmore, *Surface analysis: the principal techniques*, John Wiley & Sons, 2011.
92. D. R. Baer and V. Shutthanandan, *doi:10.1016/B978-0-12-803581-8.09285-7*.
93. C. Xu, B. Sun, T. Gustafsson, K. Edström, D. Brandell and M. Hahlin, *J. Mater. Chem. A*, 2014, **2**, 7256.
94. M. Herstedt, H. Rensmo, H. Siegbahn and K. Edström, *Electrochim. Acta*, 2004, **49**, 2351-2359.

## ***Chapter 1. Introduction***

---

95. J. Zheng, M. H. Engelhard, D. Mei, S. Jiao, B. J. Polzin, J.-G. Zhang and W. Xu, *Nat. Energy*, 2017, **2**, 17012.
96. M. I. Nandasiri, L. E. Camacho-Forero, A. M. Schwarz, V. Shutthanandan, S. Thevuthasan, P. B. Balbuena, K. T. Mueller and V. Murugesan, *Chem. Mater.*, 2017, **29**, 4728-4737.
97. M. Winter, *Zeitschrift für physikalische Chemie*, 2009, **223**, 1395-1406.
98. V. Shutthanandan, M. Nandasiri, J. Zheng, M. H. Engelhard, W. Xu, S. Thevuthasan and V. Murugesan, *J. Electron. Spectrosc. Relat. Phenom.*, 2018.
99. D. Foix, M. Sathiya, E. McCalla, J.-M. Tarascon and D. Gonbeau, *J. Phys. Chem. C*, 2016, **120**, 862-874.

# Chapter 2.

## Experimental Methods

*"You sort of start thinking anything's possible if you've got enough nerve."*

Ginny Weasley

*Harry Potter and the Half-Blood Prince*

### 2.1. Overview of the chapter

There is a particular interest in understanding the behaviour and the modification of the structure of lithium intercalation compounds; therefore, several characterisation techniques exist in order to investigate this type of materials. There are two main categories used for their study: electrochemical characterisation techniques and structural characterisation techniques.

The electrochemical characterisation techniques are used to study the electrochemical behaviour of the lithium intercalation compound as potential cathode material for lithium-ion batteries, where the capacity is measured and the redox transitions are also studied.

The structural characterisation techniques help to know what are the structure, morphology, stoichiometry, vibration modes and even the oxidation state of the different elements that form part of the studied material.

### **2.2. Electrochemical characterisation techniques**

In practice, the capacity of a battery decreases on cycling, normally as a result of degradation of the electrolyte or electrodes. The magnitude of this decrease in capacity and the rate at which it occurs has important implications on whether or not a battery is suitable for the different applications. A battery undergoes many charge / discharge cycles, so provides an easy tool for comparison between electrode materials.

The main technique used in the study of lithium-ion batteries is the galvanostatic cycling, where a controlled current is passed between a working and counter electrode, with the resulting potential typically measured as a function of time (but also as a function of the capacity).

Another important tool for the characterisation of the electrochemical processes undergone in a cell is the analysis of the change in the capacity of the active material with respect to the change in cell voltage ( $dQ/dV$ ). This is known as the differential capacity, and it is a type of plot which enables a quick characterisation of redox reactions in a battery providing important information about the electrochemical reactions taking place (due to a very similar profile if it is compared with cyclic voltammetry and other similar voltammetries). This plot is very useful in order to observe the voltage hysteresis between the charge and discharge peaks.

#### **2.2.1. Galvanostatic cycling**

A galvanostatic cycle is composed by two processes: charge and discharge. During charge the working cathode is oxidised by the positive current until a predefined upper potential limit is reached. During discharge the reverse process occurs, with a negative current being applied and the working cathode being reduced until a predefined lower

potential limit is reached. In galvanostatic cycling the current is continually reversed in this way after each transition.

The voltage profile is a useful tool in the investigation of materials and careful examination may allow the elucidation of useful electrochemical information. It is important that the voltage range selected includes the potentials at which the redox processes of lithium ion insertion and removal take place, but not the potentials at which detrimental oxidation and reduction of the electrolyte occurs.

The units for the capacity in a commercial battery are usually expressed in Ampere hours (Ah), where several cells are connected in parallel. In the studied materials, where individual cells are measured in a lab environment, the used units are milliAmpere hours (mAh). As the obtained capacity is directly related with the mass of the active material in the cathode of the cell, the used units are expressed in mAh g<sup>-1</sup> and it is called *specific capacity*. Another factor to take into account is the charge and discharge rate given by the C-rate, which is a measure of the current rate at which a battery is charged or discharged relatively to its maximum capacity (i.e. the time that the battery spends to be fully charged or fully discharged; for example, a C-rate of 1C means the current used will fully charge or discharge the cell in one hour, this is why the units are expressed in mA g<sup>-1</sup>).

Data plots are usually represented as voltage versus capacity. The increasing voltage represents the capacity during charge; when the voltage rises to a certain point, it starts to decrease, which correspond to the discharge. The obtained curves usually have plateaus that correspond to a redox reaction that is taking place at certain voltage.

When one charge and the following discharge are being completed, it means that one complete cycle has been done. Characterisation of Li-ion cells and batteries usually involves the galvanostatic charge and discharge during various cycles. One of the

## Chapter 2. Experimental Methods

applications where galvanostatic cycling can be used is in the study of the cyclability, which is a measure of the capacity retention during cycling, and may be easily illustrated by plotting the total charge capacity and/or total discharge capacity against cycle number. This is an important tool in order to observe easily the evolution of the capacity of the material, which is usually related of a loss of the capacity after several cycles. An example of galvanostatic cycling and cyclability is shown in **Figure 2.1**.

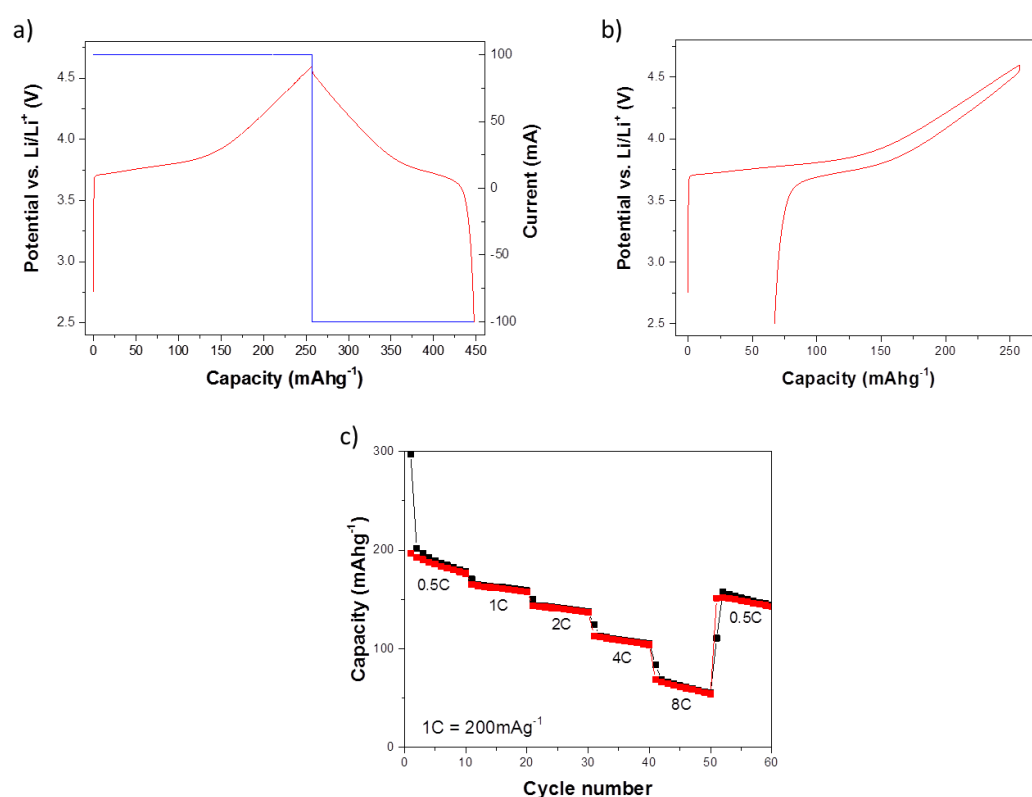


**Figure 2.1.** Electrochemical measurements of  $\text{LiCo}_{1/3}\text{Ni}_{1/3}\text{Mn}_{1/3}\text{O}_2$  using (a) continuous and (b) cyclic galvanostatic cycling. The blue line in graph (a) represents the current that is passing through the cathode during charge and discharge using a current of 100 mA. Graph (c) represents the cyclability of  $\text{LiCo}_{1/3}\text{Ni}_{1/3}\text{Mn}_{1/3}\text{O}_2$  at different C-rates (100, 200, 400, 800, 1600 and 100  $\text{mA g}^{-1}$ ) during 60 cycles. The black dots represent the capacity during charge and the red dots represent the capacity during discharge.



### 2.2.2. Differential capacity

The plot starts at a baseline of  $dQ/dV = 0$  mAh/V and exhibits peaks at the voltages at which chemical reactions occur (with the positive differential capacity peaks relating to charging of the active material, and the negative peaks relating to the discharge), as can be observed in **Figure 2.2**.

Since electrochemical processes at certain voltages may be attributed to certain redox reactions (i.e. the oxidation or reduction of transition metal ions in a cathode material), this enables differences between cycles or materials to be easily identified (i.e. an increasing peak attributed to a specific transition metal ion indicates increased participation in the electrochemical processes).

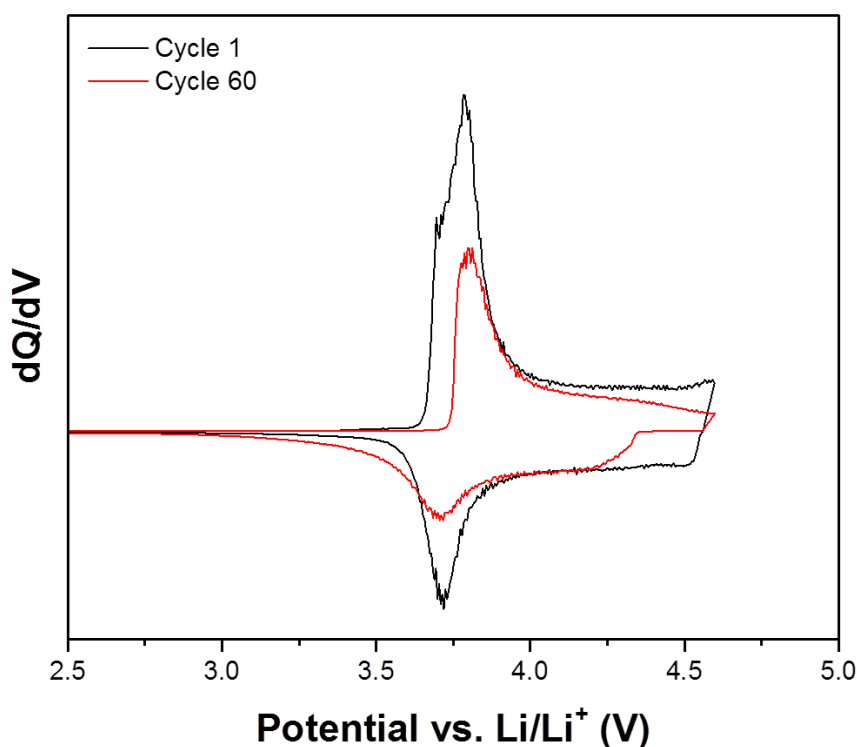


**Figure 2.2.** Example of differential capacity plot of  $\text{LiCo}_{1/3}\text{Ni}_{1/3}\text{Mn}_{1/3}\text{O}_2$  and its comparison between 1<sup>st</sup> and 60<sup>th</sup> cycle.

## Chapter 2. Experimental Methods

---

### 2.2.3. Factors that can affect the electrochemical measurements

Theoretically the profiles during charge and discharge should coincide, although this is not the case in practice (this can be observed in **Figure 2.1a.**). This may be due to a variety of factors, such as Ohmic loss<sup>1</sup> (voltage drop due to resistance of the cell components and interconnects), work function at the solid electrolyte interphase, resistance to ion transfer through the electrolyte, porosity, thickness of the casting material and its density after compressing the cathode<sup>2,3</sup>.

The C-rate is another important factor: using high C-rates, the movement of the Li<sup>+</sup> ions is too quick and the intercalation / deintercalation cycle of these ions is incomplete and therefore becoming less reversible, which means that the capacity decreases; in other words: the high is the C-rate, the low is the capacity.

Other important factors that can affect the capacity of the materials are:

#### *1) Solid electrolyte interphase (SEI) and cathode electrolyte interface (CEI)*

The SEI layer<sup>4</sup> is a passivation layer that contains various electrolyte reduction / decomposition products (organic and inorganic).<sup>5</sup> It protects the electrode from side reactions acting as an electronic insulator preventing the continuous reduction of electrolyte as the film thickness reaches a certain limit, and protects the fast deterioration of Li-ion batteries.<sup>6-11</sup> These surface films control the electrochemical behaviour of Li electrodes and in fact determine the safety, shelf life, and cycle life of Li-ion batteries. But the formation of this layer has some disadvantages: the diffusion of Li<sup>+</sup> ions through the electrolyte is becoming more difficult, which decreases the capacity of the battery. Similarly, there is a lesser-known analogous layer on the cathode side of a Li-ion battery, termed the *cathode electrolyte interface* (CEI),<sup>12</sup> which forms via oxidative reactions between cathode and electrolyte.

### *2) Composition of the casting*

An electrode usually is composed by the active material (the lithium intercalation compound in this case), a conductive carbon and a binder. In order to prepare the cathodic electrode, it is necessary to do a casting with a mixture of these three components on the surface of a current collector. The binders used in the casting for the electrochemical measurements can affect the behaviour of the material and the oxidation states that each transition metal have in the uncycled material or after several cycles, as well as their influence on the electrode performance.

Poly(vinylidene difluoride), known as PVDF, is the most commonly used binder in Li-ion batteries as a result of its good electrochemical stability and high adhesion to electrode materials and current collectors. However, the stability of this binder towards reducing agents is not satisfactory because of the presence of fluorine, affecting the thermal runaway<sup>13</sup> and, therefore, the surface stability causing a distortion in the peaks measured in X-ray photoelectron spectroscopy and other characterisation techniques. Nowadays, there is an increasing interest in using alternatives such as carboxymethyl cellulose sodium salt (CMC).<sup>14-20</sup>

The used solvent to disperse the mixture of components before doing the casting is another important factor to obtain the best electrochemical performance in the measured cell. In the case of CMC, as it is a salt, the used solvent is water; but for PVDF, as it is an organic polymer, an organic solvent is needed. The most common and widely used is N-methyl-2-pyrrolidone (NMP) due to a better mix between the different components of the slurry, but it is very toxic and it needs temperatures of around 200 °C and long time to evaporate completely. An alternative with similar characteristics is tetrahydrofuran (THF), which is very volatile and it evaporates in few seconds at room temperature.

## ***Chapter 2. Experimental Methods***

---

### **2.2.4. Cell components**

To evaluate the electrochemical performance of the samples, composite electrodes were fabricated by tape-casting method, consisted in a mixture of active material: conductive additive: binder in a ratio of 84:8:8% or 80:10:10% by weight, depending of the studied material. The active material corresponds to the compound of interest, the conductive additive was Carbon Super-C and the binder was poly(vinylidene difluoride-co-hexafluoropropylene) co-polymeric binder (PVDF-HFP). The components were added in a vial in this order: 1) binder, 2) conductive additive, 3) active material. Finally, the electrode materials were dispersed in tetrahydrofuran (THF), stirring the mixture for at least 2 hours.

Electrode slurries were cast onto an aluminium current collector using a doctor blade to a thickness of approximately 20  $\mu\text{m}$  once dried (**Figure 2.3a.**). Once dried, castings were punched to make circular electrodes with a diameter of 10 mm. Electrodes were dried under vacuum at 70 °C before assembly in an Ar-filled glovebox ( $\text{O}_2$ ,  $\text{H}_2\text{O}$  < 1 ppm).

2025 type coin cells were assembled according to the configuration shown in **Figure 2.3a.** The prepared electrodes were used as cathodes; 1M  $\text{LiPF}_6$  in ethylene carbonate and dimethyl carbonate was used as electrolyte, impregnated in a borosilicate glass fibre separator (Whatman, Grade CG/C) with excess volume, and a Li metal counter electrode (0.75 mm thickness x 16 mm diameter, Sigma-Aldrich) was used as an anode. Finally, coin cells were hermetically sealed, ensured by the use of a polypropylene O-ring gasket.

Alternatively, home-built battery-type Swagelok cells were used to study the electrode after electrochemical measurements (several cycles, only charge and/or only discharge) using different structural characterisation techniques because of their facility of being disassembled with unscrewing them (while coin cells need clippers to be

disassembled). Swagelok cell's configuration is very similar to coin cells; in this case, two glass fibre separators were used. Two stainless steel meshes were employed to ensure electric contact through the electrodes (**Figure 2.3b.**).

Electrochemical charge / discharge measurements were carried out at 30 °C using a Maccor Series 4000 battery cycler. The cycling procedures and currents were varied depending on the active material tested and are described in subsequent results chapters. Tests were performed with at least two electrodes to confirm reproducibility of results. Reported results are either the average of these tests or the best performing electrodes.

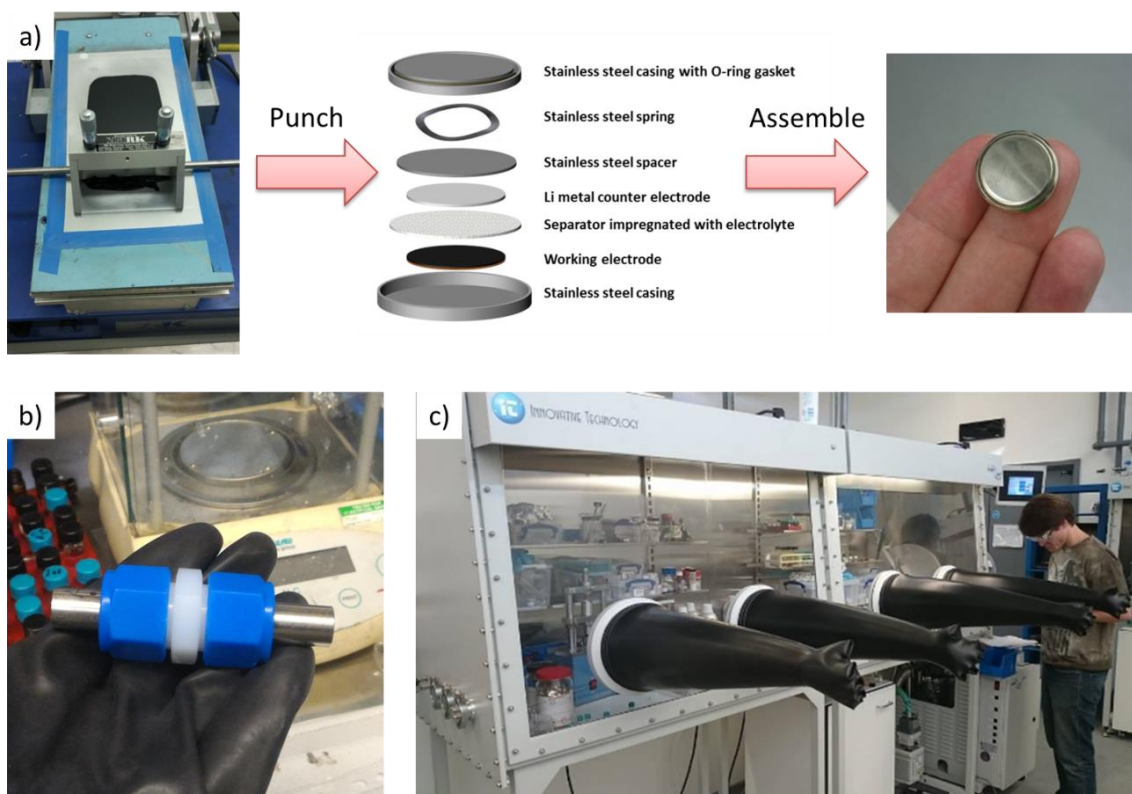


**Figure 2.3.** (a) Process of making a coin cell, with the casting of the slurry and its uniform distribution using a doctor blade, as well as the description of the different parts that form part of the coin cell. (b) Assembled Swagelok cell. (c) Ar-filled glovebox where the cells were assembled.

## ***Chapter 2. Experimental Methods***

---

### **2.2.5. Cleaning cycled electrodes**

In order to understand the electrochemical behaviour of the lithium intercalation materials studied in this thesis, different structural characterisation techniques were used. The electrodes were measured at different voltages during charge / discharge and at different cycles using Swagelok cells and unscrewed inside the Ar-filled glovebox.

For XPS measurements, it is necessary to remove any residual electrolyte and glass fibre that can be attached onto the surface, as well as the possible formation of a CEI, because this layer can be very thick and therefore the elements of interest cannot be detected. For that purpose, the electrodes were washed in a small vial using few drops (~1 ml) of dimethyl carbonate (DMC) to impregnate the electrode, and the adsorbed species in the surface can be dissolved in this liquid. Finally, DMC was removed and the electrodes were dried under vacuum overnight in the antechamber of the glovebox without exposure to air in order to avoid any modification of the oxidation state of the present elements. After drying, electrodes were put inside the glovebox, ready to their transportation and study using different characterisation techniques.

### **2.3. Structural characterisation techniques**

Understanding the structure of the studied materials is essential in order to understand their electrochemical behaviour. In this research, several structural characterisation techniques were used: X-ray diffraction (allows information of the crystal structure), scanning electron microscopy (shows the morphology of the samples at the nanoscale), inductively couple plasma optical emission spectroscopy (elemental analysis of the samples), X-ray absorption near edge spectroscopy (gives information of the atomic structure of the material), Raman spectroscopy (vibrational technique that gives

information about what kind of bonds are formed between the different elements of a given compound) and X-ray photoelectron spectroscopy, which is an important tool for the analysis of the surface of a sample, providing both qualitative and quantitative information on the elements present (except for hydrogen and helium) on a given surface.<sup>21</sup> X-ray photoelectron spectroscopy is the most widely used surface analysis technique because it is surface sensitive, and any modification of the surface can affect the final result and the quantification of the peaks, including chemical and oxidation state,<sup>22</sup> therefore this technique is very useful to study how the compound behaves at different voltages during an electrochemical measurement. Since the average depth of analysis for an XPS measurement is approximately 5 nm, not only the electronic processes of lithium intercalation in thin film electrodes<sup>23</sup> can be investigated with this technique, but also the surface of bulk materials.

### 2.3.1. X-Ray Photoelectron Spectroscopy (XPS)

XPS is based in the photoelectric effect<sup>24</sup> where the incident photons have energies in the range of X-rays and, after falling on the surface of a material, electrons overcome the work function (the minimum amount of energy that an individual electron needs to escape from the surface) and are emitted from the core into the vacuum as photoelectrons:

$$E_K = h\nu - E_B - \phi \quad (2.1)$$

Where  $\phi$  is the work function of the sample;  $E_B$  is the atomic core level binding energy of the electron in the atom (dependant on the type of atom and its chemical environment) relative to the Fermi level ( $E_F$ );  $h\nu$  describes the energy of the X-ray excitation source and  $E_K$  is the kinetic energy of the emitted electron which is measured by the spectrometer. An example of this emission is represented in **Figure 2.4a.** and **2.4b.**,

## Chapter 2. Experimental Methods

where is taking place the photoemission of an inner electron of an oxygen atom. Typically, the sample is placed in an ultrahigh vacuum environment (less than  $10^{-8}$  mbar) to avoid any loss of energy for the electrons, and exposed to an X-ray of known energy.

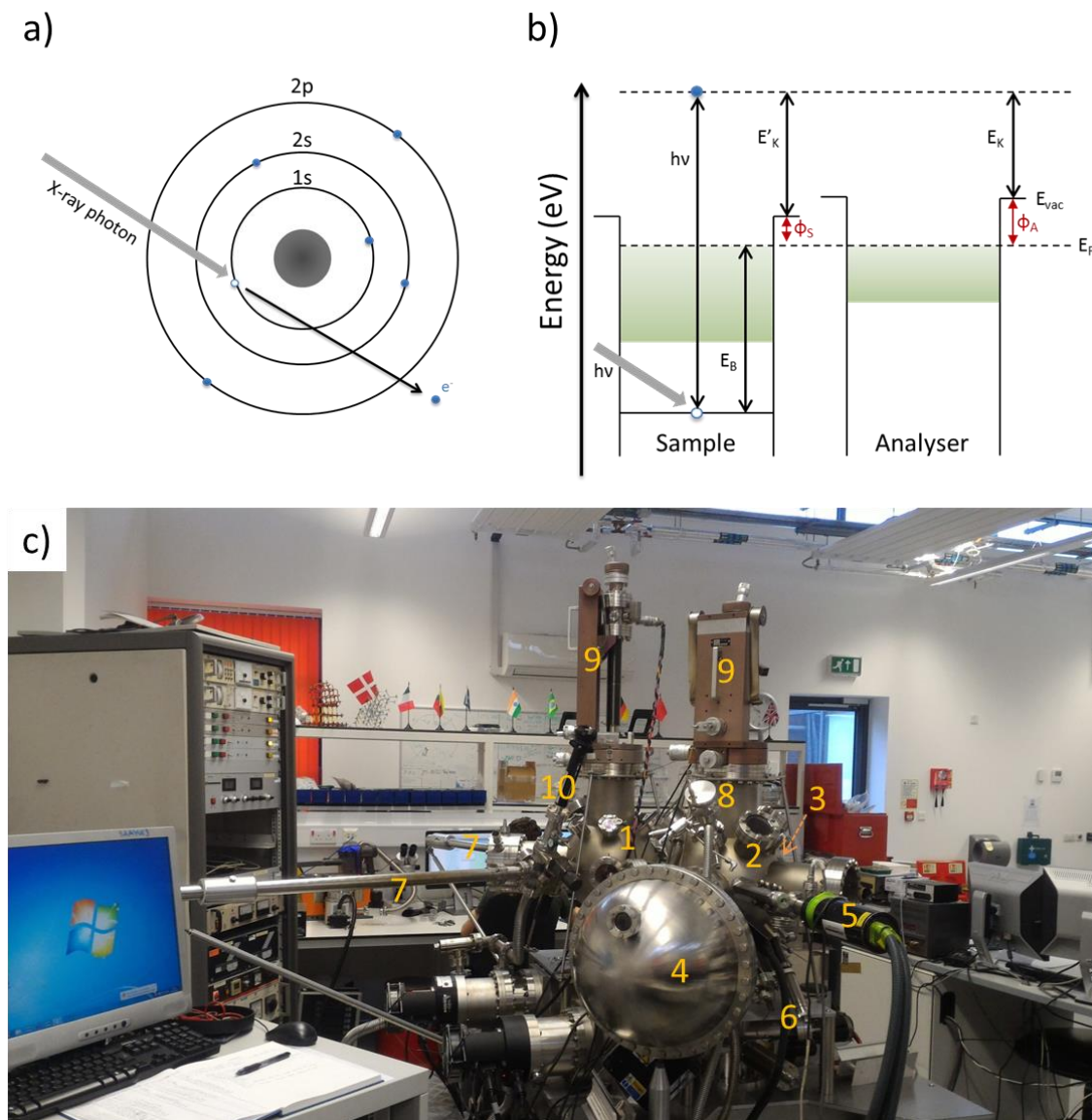


**Figure 2.4.** (a) Schematic of how the photoemission works, where the energy from X-rays come to an oxygen atom and produces the emission of a photoelectron from the 1s orbital. (b) Relative band levels and Fermi-level alignment between sample and analyser. (c) Picture of the X-ray photoelectron spectrometer used in the laboratory.



**Figure 2.4c.** represents the XPS spectrometer used for measuring the samples exposed in this thesis; it is a 3-chamber surface science ultrahigh vacuum system formed by: 1) a preparation chamber, 2) an analysis chamber, 3) a STM chamber, 4) electron energy analyser, 5) X-ray gun, 6) evaporator, 7) transfer arms, 8) UV gun, 9) 4-axis manipulators and 10) transfer chamber.

The energy of an ejected core electron is characteristic of the element from which it was emitted, and is a function of its binding energy. An XPS spectrum may be obtained by plotting the number of these electrons as a function of kinetic (or binding) energy, the peaks of which provide considerable information – their corresponding energy is characteristic of the elements present; their area is a measure of the relative amount of that element, and their precise position and shape indicates that element's chemical state. Thus, comparison with tabulated data makes it possible to identify the elements present in the sample's surface, as well as their chemical and oxidation state.

### 2.3.1.1. Photoemission

The definition of photoemission is the emission of electrons from a sample via the photoelectron effect. The measurement of the energy of these electrons is known as photoemission spectroscopy, where XPS is one of these techniques. When an electron is moving through the sample, it results in a photoelectron kinetic energy ( $E_K$ ) that is related to the photon energy, its binding energy ( $E_B$ ), and the work function of the sample ( $\phi$ ) as described in equation (2.1).

The photoemission process takes place when the electrons overcome the work function, and are emitted into the vacuum. This work function is the energy difference between the Fermi level ( $E_F$ ) and the vacuum level ( $E_{vac}$ ).

## Chapter 2. Experimental Methods

---

In connecting a sample electrically to the analyser, the Fermi levels of the two systems align, resulting in the situation shown in **Figure 2.4b**. Electrons in the sample have a binding energy ( $E_B$ ) with respect to the Fermi level. Incident photons transfer their energy ( $h\nu$ ) to the electrons, producing photoelectrons, which escape the sample after overcoming the  $E_B$  and the work function of the sample ( $\phi_s$ ), so that they have a vacuum kinetic energy ( $E'_K$ ) of:

$$E'_K = h\nu - E_B - \phi_s \quad (2.2)$$

As the analyser is connected to the sample and has its own work function ( $\phi_A$ ), the measured  $E_K$  is:

$$E_K = E'_K - (\phi_A - \phi_s) = h\nu - E_B - \phi_s - (\phi_A - \phi_s) = h\nu - E_B - \phi_A \quad (2.3)$$

which can be re-written as:

$$E_B = h\nu - E_K - \phi_A \quad (2.4)$$

where now the measurement of the photoemission is independent of the work function of the sample but depends of the work function of the analyser ( $\phi_A$ ). This helps to simplify the calculation of the binding energy (converting the measurements of the kinetic energy) because it is not necessary to know beforehand the work function of each material but only the work function of the used analyser, which is a constant.

### 2.3.1.2. X-Ray Source

In order to analyse the spectra of a certain material, it is necessary to obtain photoelectrons with a frequency in the X-ray range. These are obtained by bombarding a target material with high energy electrons.<sup>25</sup>

The X-ray source corresponds in an X-ray gun, which consists in an isolated rod, coated at the end with the target material in order to produce different photon energies;

the most common is to use two different target materials. The combination of the rod and the target material is known as *anode*. Close to the target material there is a filament (one filament for each target material) that can produce electrons when a current is passing through it; the current is increased manually and then fixed to a certain point, usually when the emission of electrons is observed. A high positive voltage (between 12 and 17 kV, depending of the studied material) is applied to the anode in order to accelerate the electrons and bombard the target material, producing the emission of X-rays with different energies, which are then directed towards a sample.

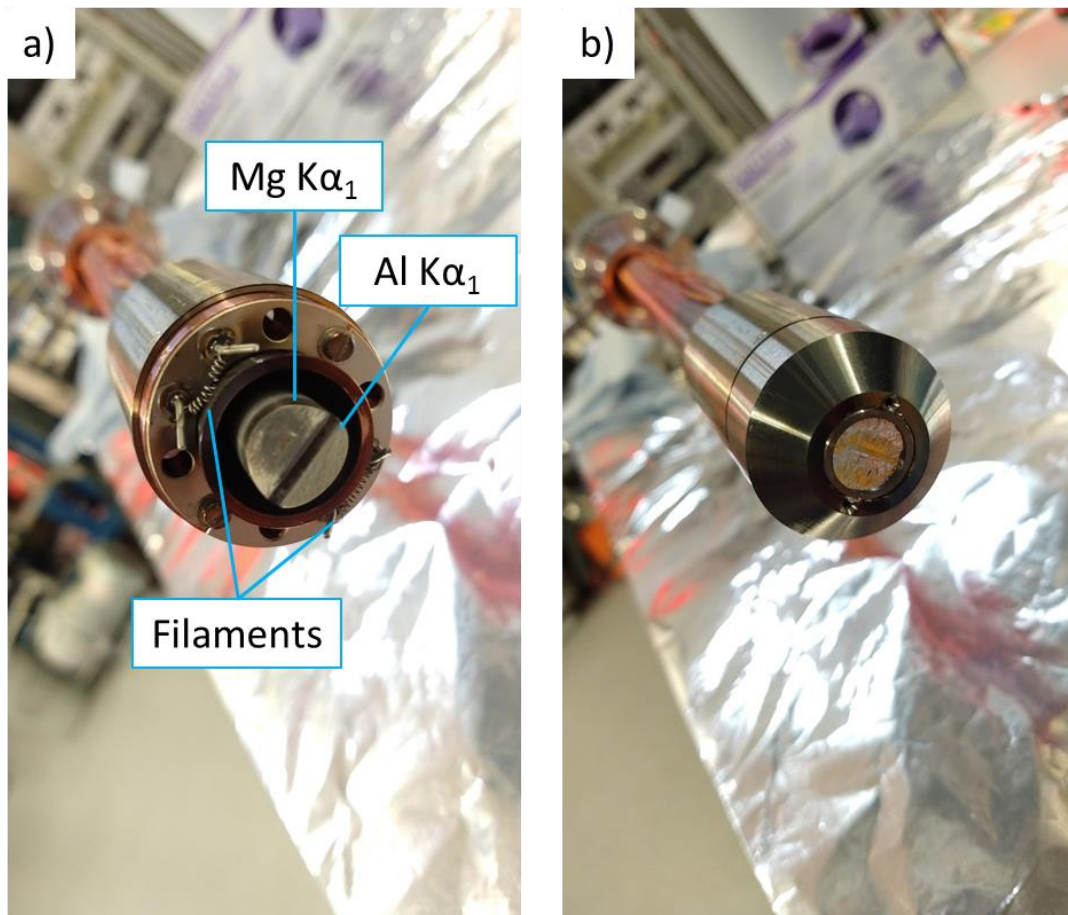


**Figure 2.5.** (a) X-ray gun where it is possible to observe the dual anode formed by Al K $\alpha_1$  and Mg K $\alpha_1$  and their corresponding filaments. (b) Aluminium foil that covers the gun to avoid the excess of energy.

## ***Chapter 2. Experimental Methods***

---

The photons that are incident on a sample have different energies; this is known as a non-monochromatic X-ray source, resulting in extra features in the spectra, such as the formation of satellites (secondary features that mirror the photoemission processes, but have lower intensities). The primary emission lines used in non-monochromatic XPS are usually Al  $K\alpha_1$  (1486.6 eV) and Mg  $K\alpha_1$  (1253.6 eV), both of which have a natural linewidth  $<1$  eV, with magnesium generally favoured because of its slightly narrower linewidth<sup>26</sup> (the most of the results presented in this thesis correspond to the use of magnesium anode). It is possible to use a monochromatic X-ray source using a quartz crystal and selecting Al  $K\alpha_1$  line; this is very useful for photovoltaic materials, where it is important to quantify the valence band.<sup>27, 28</sup> For this research, the used spectrometer has non-monochromatic X-ray source with a dual anode formed by Al  $K\alpha_1$  and Mg  $K\alpha_1$  as it is shown in **Figure 2.5a**.

As a high voltage is being applied, there is an excess of energy that can modify the final result of the measurement, therefore it is usual that the X-rays pass through a thin film of aluminium to avoid the excess of energy against the sample (**Figure 2.5b**).

### *2.3.1.3. Spectrometer*

The spectrometer used in XPS can be divided into two parts: the analyser, which only allows electrons of certain energy to pass through, and the detector, which counts the number of electrons that were allowed to pass through the analyser. Then, by sweeping across the possible kinetic energies, and counting at each point, a spectrum can be generated.

The analyser used in XPS consists of two concentric, hemispherical plates through where a potential is applied. An incident electron will traverse around if its kinetic energy

is such that the deflecting potentials keep it on a concentric course with respect to the plates, this is known as *pass energy*.<sup>25</sup> Electrons with energy bigger than the pass energy will collide with the external plate; if it is smaller, electrons fall in the internal plate. In both cases, the number of electrons that reach the detector is very small; in this case, a multiplier is used to increment the signal until reach to a limited energy. By changing the potential applied across the plates, it is possible to alter the pass energy and theoretically sweep through the range of kinetic energies required.

The spectrum that can be measured in XPS covers a kinetic energy between 0 eV and the maximum emission energy of the X-ray source; this is known as *region*. When the whole region is measured in XPS to observe which elements are present in the sample (known as *survey spectrum*), a high constant pass energy (CPE) is applied, and therefore the obtained intensity (measured in counts per second, or CPS, which is the number of electrons ejected from the sample – usually defined as “counts” – received by the analyser per unit time) is high because a big number of electrons are passing through the analyser. When specific regions of limited kinetic energy are measured (i.e. the core-level peak of a certain element), usually the CPE is smaller in order to obtain a better resolution (the smaller the pass energy, the smaller the intensity and the individual regions can be observed more in detail).

### 2.3.1.4. Spectral Features

When the electrons reach the detector, a spectrum is measured. XPS spectrum can be defined as a series of peaks with binding energies representative of each orbital of each element contained in a sample. Usually the XPS spectrum is displayed as a function of decreasing  $E_B$ .

## Chapter 2. Experimental Methods

---

If photoemission results in an electron that has not lost any energy and it is originated from a non-valence orbital (i.e. core electrons), then the peak is described as a core-level peak. These are identified using spectroscopic notation of the form  $nl_j$ , representing the principle, azimuthal, and total angular momentum quantum numbers,<sup>29</sup> respectively. The value of  $j$  is obtained according to  $|l \pm m_s|$ , where  $m_s$  is the spin momentum ( $m_s = 1/2$ ). For  $l = 0$ ,  $j = 1/2$  is the only possible value, and so  $s$  orbitals result in a singlet. For  $l > 0$ ,  $j$  can take two values and so results in a doublet, separated by a specific energy; this is known as the spin-orbit splitting.<sup>22, 30, 31</sup> Depending of the occupancy of each of the doublet orbitals ( $2j + 1$ ), the intensity of the ratios between the doublet peaks can vary. This is shown in **Table 2.1**.

**Table 2.1.** XPS spin-orbit doublet intensity ratios due to the electronic occupancy of the orbitals.

<b>l</b>	<b>j</b>	<b>Occupancy</b>	<b>Ratio</b>
<b>s (l = 0)</b>	1/2	2	-
<b>p (l = 1)</b>	1/2, 3/2	2, 4	1:2
<b>d (l = 2)</b>	3/2, 5/2	4, 6	2:3
<b>f (l = 3)</b>	5/2, 7/2	6, 8	3:4

The energy of this doublet separation is characteristic of each core electron of each element and it usually depends on the oxidation state of the element (with some exceptions), therefore it may be a direct relationship between the doublet separation and the oxidation state; this property is very useful in order to calculate the oxidation state of a studied material with very good accuracy using databases with previous measurements of similar materials to compare the results,<sup>32, 33</sup> above all if there are transition metals in

the compound of interest. This characteristic can be applied in the Ni 2p spectrum used as an example in **Figure 2.6**. The ratio in this case is not exactly 1:2, and this can be due to different reasons (such as distortion of the baseline from the proximity of other core-level or an Auger peak).

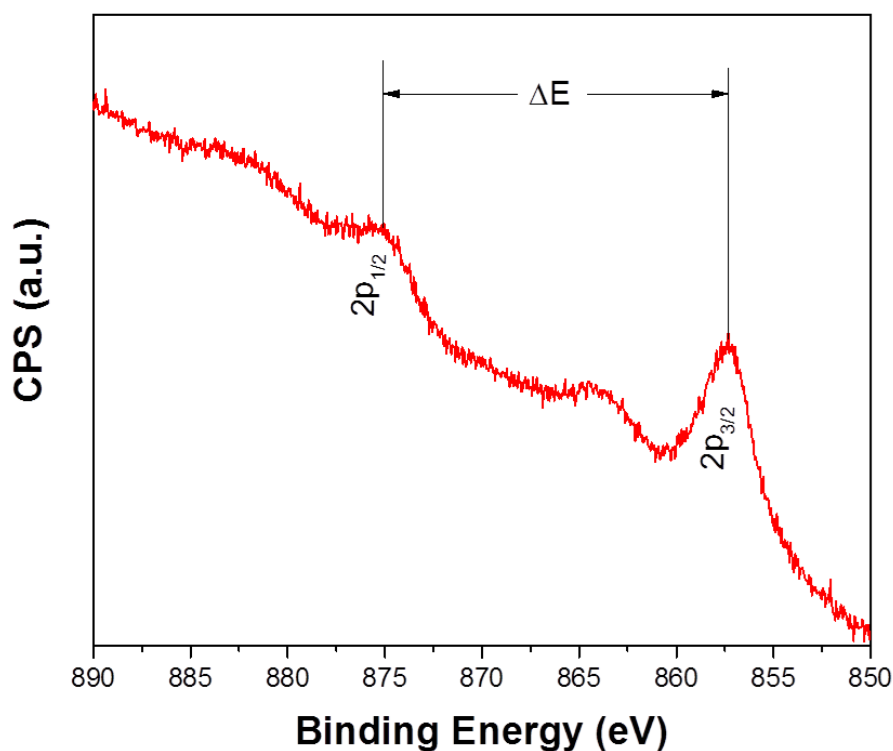


**Figure 2.6.** Doublet separation of Ni 2p of one of the studied materials ( $\text{Li}_{4.15}\text{Ni}_{0.85}\text{WO}_6$ ), where its characteristics satellites can also be observed.

It is very common to have different core-level peaks of a certain element. However, one of them is the most predominant and usually corresponds to the electron to an inner orbital. In the case of a non-metal element from the second row (such as oxygen), the most intense peak corresponds to 1s bond; for the transition metals for the fourth row for instance is the peak from the 2p bond. These predominant peaks are the most widely used

## Chapter 2. Experimental Methods

of each element because other minor peaks are a reflection of this one. This can be observed in the survey scan for manganese acetate shown in **Figure 2.7.**, where the peaks of each element are represented; Mn 2p has higher intensity than Mn 3p and Mn 3s, and therefore this is the peak that usually is measured.

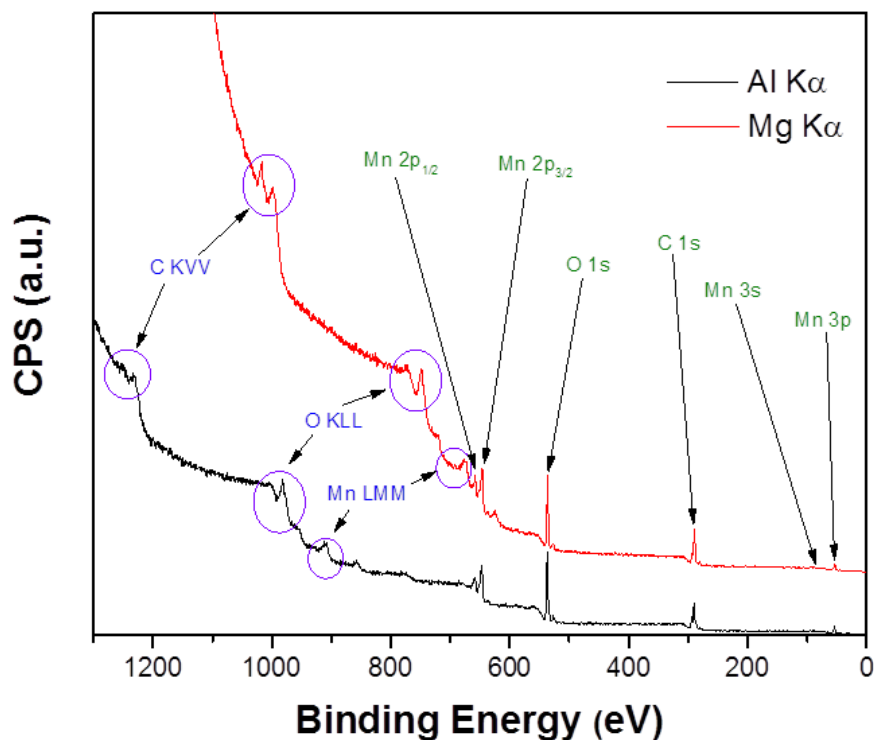


**Figure 2.7.** XPS survey spectrum of manganese acetate measured using two different anodes: Al  $K\alpha_1$  and Mg  $K\alpha_1$ . It is possible to observe the different elements that form part of the compound: C, O and Mn. C 1s and O 1s are the most intense core-level peaks of each element, while Mn 2p (and the corresponding spin-orbit splitting) is the most intense peak for Mn. Auger electrons (violet circles) are also observed.

During the second stage of the photoemission process, there is a finite probability that the photoelectron will lose energy as a result of inelastic scattering as it moves



through the sample due to collisions with other electrons and plasma excitations. This manifests as a rising background of secondary electrons, increasing with  $E_B$ , onto which the photoemission peaks are superimposed, as seen in the example in **Figure 2.7**.

After photoemission, the core-hole left by the photoemitted electron can be filled by an electron from a higher orbital relaxing into it, causing the emission of a second, Auger electron, whose kinetic energy is related to the energy level differences and is independent of the photon energy,<sup>25</sup> therefore the obtained Auger peaks depend of the chosen X-ray source and appear at different  $E_B$  depending of which anode is used (Mg  $K\alpha_1$  or Al  $K\alpha_1$ ). Due to the multitude of orbitals that can be involved in the Auger process, these features manifest in XPS spectra as broad, energy-expansive features with multiple peaks and sometimes can overlap a core-level peak. An example of these Auger peaks was represented in **Figure 2.7**.

### 2.3.1.5. Chemical shifts

The atomic binding energies vary for different elements and this allows us to determine what elements are present in a sample. However, it is the information about the chemical environments within a material that XPS can provide which makes it such a powerful technique.

The  $E_B$  of an electron arises from the electrostatic interaction between itself and the positive nuclear charge of an atom, but is also dependent upon the presence of other electrons around the atom. Changes in electron density surrounding an atom can affect the measured  $E_B$ . This can be explained using ionic bonding: for a cation, there is less electron density surrounding the atom because some electrons have been transferred to the anion, which results in less nuclear screening, and therefore a lower measured

## Chapter 2. Experimental Methods

---

photoelectron  $E_K$  (and thus, a higher  $E_B$ ); the opposite way is followed by the anions. In other words: a higher oxidation state results in a larger  $E_B$  shift, and a more negative oxidation state means a lower  $E_B$  ( $\dots > E_B^{2+} > E_B^+ > E_B^0 > E_B^- > E_B^{2-} > \dots$ ).

In the case of covalent or mixed bonding materials, similar trends apply, given that most inorganic materials can be assigned formal oxidation states, but the size of the  $E_B$  shifts are also dependent upon the level of covalency, the strength of the bonds, and also the differences in electronegativity between two atoms. A larger electronegativity difference will result in a larger  $E_B$  and a longer bond length results in smaller  $E_B$  shifts (i.e. ionic bonds give larger  $E_B$  than covalent bonds because the first ones have stronger bonds and therefore smaller bond lengths than the second ones).

These shifts can be observed in **Figure 2.8.**, where a deconvolution of C 1s peak is done; the analysed sample correspond to one studied electrode with the presence of the active material, the binder (PVDF) and the conductive carbon additive, and there were C-C, C-H, C-O, C=O and C-F species. In the plot, C-F bond, which has the biggest difference in electronegativity between the atoms, appears at high  $E_B$ , whereas C-C and C-H bonds have the smallest  $E_B$ . In the case of the bonds between carbon and oxygen, C=O has a stronger bond than C-O, and therefore appear at a higher  $E_B$ . The reason why it is possible to observe different C-F and C=O species in the C 1s peak is due to the covalency of the bonds formed in the compounds; depending of the electronegativity of a neighbour atom, the covalency of these bonds can be weaker or stronger, thus affecting the shift in the position.

Core-level peaks in XPS have finite width and, in order to analyse a peak, a fitting is necessary, especially if there is possibility of the peaks overlapping, demonstrated by the many spectral features in **Figure 2.8.** For fitting, the most common background used in

XPS is a Shirley background, which is an iterative background that can split a region into many  $E_B$  steps and calculate the background of the next step depending on the background and intensity values of the previous steps.<sup>34</sup> Usually, the most of the core-level peaks are mixed Gaussian-Lorentzian (Voigt) peak profiles,<sup>29</sup> and this is the type of fitting used in this thesis.

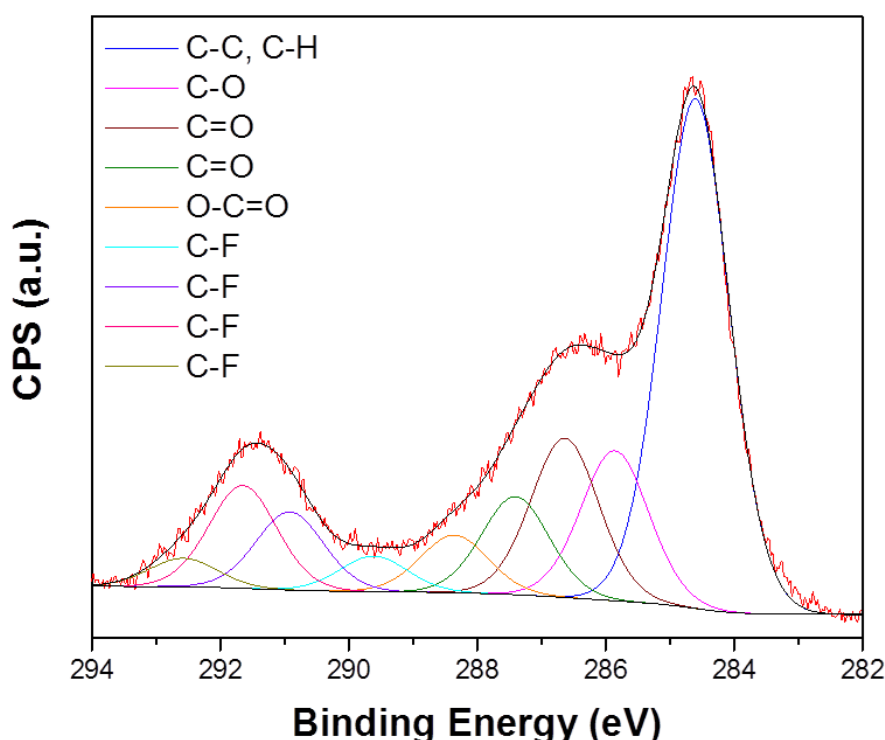


**Figure 2.8.** XPS spectrum of C 1s peak of a typical analysed electrode with the presence of different species and different type of bonds (C-C, C-O, C=O, C-F) coming from PVDF binder and conductive additive. The deconvolution shows the presence of several C=O and C-F peaks. These peaks with different energies are due to different factors, such as the electronegativity and oxidation state of a neighbour atom, if the effective nuclear charge is more positive or more negative, etc. The NIST X-ray Photoelectron Spectroscopy Database<sup>35</sup> was used as reference to assign the type of bonds that have been formed.

## ***Chapter 2. Experimental Methods***

---

The goal of peak fitting is to extract the intensity and  $E_B$  of the different chemical species present in a sample by adding peaks with variable position, area and full width at half maximum (FWHM), and try to match as closely as possible the measured data with a standard spectra database or any previous studies of similar materials.

Each chemical environment can be represented by an individual peak/doublet present for each orbital, and whilst a perfect fit to the experimental data can be achieved by adding an infinite number of peaks, constraints to the fitting must be imposed in order for a model to be physically representative. In the case of spin-orbit split doublets, the energy difference of the splitting and area ratio between the peaks is known, and generally, the FWHM between the peaks of a spin-orbit split doublet should be the same size for a single chemical environment (although there are some exceptions). These constraints can also be applied for a single peak, where their different components can be compared with more accuracy, as the example shown in **Figure 2.8**.

XPS analysis can be used to quantify the amount of each element that is present in a sample but sometimes the intensity of the peaks can vary due to different factors (distortion of the baseline, overlapped peaks, etc.) and therefore it is not reliable to calculate the ratio and stoichiometry of the compound from the areas of the peaks using this technique, above all with the present of numerous elements in a measured sample. In this case there are different elemental techniques such as ICP-OES that can obtain accurate %wt ratio of key elements. However, the fitting of each individual core-level peak can provide an approximate percentage of the different species that form part of a certain element, in spite of the potential problems described before. For example, if in the deconvolution of an O 1s peak there is approximately 50% of the area due to a metal oxide and the other 50% from the metal hydroxide, it means that the half of the metal-

oxygen bond is due to the formation of an oxide and the other half is from the formation of the hydroxide. This important characteristic can also be applied in **Figure 2.8.**; doing a proper deconvolution, it is possible to quantify the area of each formed chemical bond and the total contribution of C-O and C-F species according to **Table 2.2.**

**Table 2.2.** Quantification of chemical bonds from C 1s deconvolution in **Figure 2.8.**, where the binding energy position, type of chemical bond and the area are shown.

<b>E<sub>B</sub> (eV)</b>	<b>Chemical Bond</b>	<b>Area (%)</b>	<b>Total contribution (%)</b>
284.6	C-C, C-H	41.8	41.8
285.86	C-O	12.3	38.11
286.63	C=O	13.05	
287.4	C=O	8.03	
288.35	O-C=O	4.73	
289.61	C-F	2.91	20.09
290.92	C-F	6.41	
291.65	C-F	8.42	
292.58	C-F	2.35	

To summarise, the chemical shifts observed in the XPS can be used to investigate what type of chemical bonds are being formed, the strength and covalency and if it is a single or double bond, as well as the quantification of the components of a specific peak. It is also possible to obtain the oxidation state of an element due to a change in  $E_B$  (with the additional help of the doublet separation due to the spin-orbit splitting). These tools are the main reason why XPS is a powerful technique in order to understand the

## Chapter 2. Experimental Methods

electrochemical behaviour of lithium intercalation compounds.

### 2.3.1.6. Cleaning the surface of a sample

It is common to find some contaminants in the surface of a sample, maybe formed during the synthesis or during the handling of the sample in atmospheric air. In this last case, we are talking about physical adsorption.

The most common of the physical adsorbed species is adventitious carbon, which is a thin layer of carbonaceous material usually found on the surface of most air exposed samples.<sup>36, 37</sup> Even small exposures to atmosphere can produce these films, and the detection of some adventitious carbon is a product of nearly every XPS analysis. Usually the strongest peak of the C 1s spectrum corresponds to the carbon species from  $sp^3$  hybridisation, usually hydrocarbons species (C-C and C-H bonds, respectively), and small amounts of both singly and doubly bound oxygen functionality (-C-O and -C=O, respectively) as it is shown in **Figure 2.9a**.

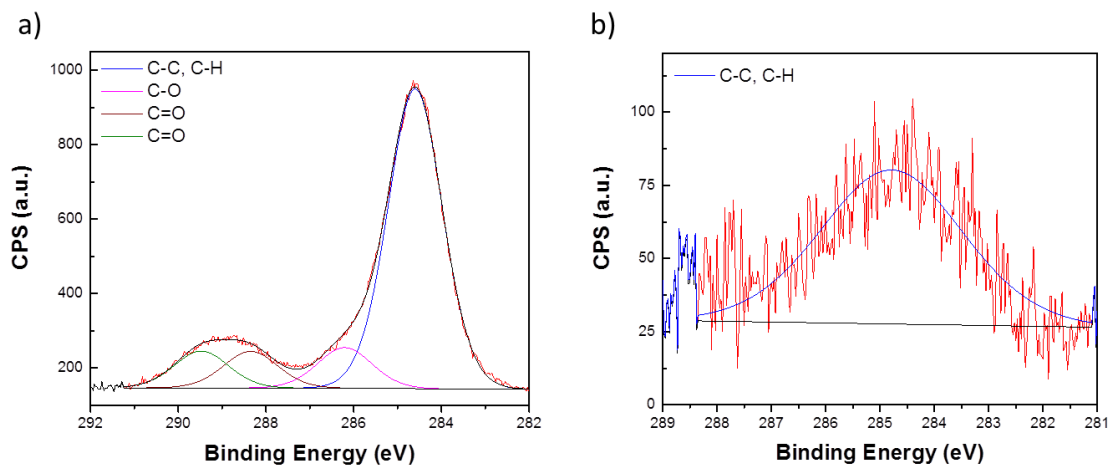


**Figure 2.9.** (a) XPS spectra of C 1s with the observation of adventitious carbon in the surface of pure Li foil after being exposure on air for a short period of time (~5 min). (b) XPS spectra of C 1s after sputtering of the surface of Li foil, where only remain some residual carbon after 4 flashes with  $Ar^+$  gas.

Adventitious carbon and other adsorbed species (for example, water from the atmosphere) do not affect the chemical properties of the measured material. However, if the layer that covers the material is too thick, it can hide weak core-level peaks that could be important to measure. In that case, it is very important to eliminate that layer.

There are two main methods used in order to clean the surface of a sample: a) The first method is to do sputtering, where a jet of  $\text{Ar}^+$  gas collides with the sample, removing all the adsorbed species on the surface as it is shown in **Figure 2.9b**. The problem with this method is the possibility to be applied only in few materials (as pure metals, for example), because it can modify the oxidation state of the elements of the sample. b) Other option is to do an annealing, consisting in heating the sample inside the XPS chamber using a hot filament in order to evaporate the carbonaceous and/or the water particles adsorbed in the surface, ionising the gas molecules. In this case, the problem lies in the plate used to hold the samples, which contains carbon tape; the annealing melts the carbon tape and the sample falls off the plate. It is possible to use tantalum wires to secure the sample, but it is not working when the measured sample is a powder. This method is not available either for samples that have a relatively low melting point.

### 2.3.1.7. Charge correction

During the photoemission, an ejected photoelectron leaves a hole in a measured sample. In order to fill this core hole, the XPS spectrometer is connected to an earth wire that provides electrodes to the material. For conductive materials (such as the sample electrodes measured in this thesis), these core holes left for the photoelectrons can be filled easily but for insulating surfaces the fill of these core holes become more complicated due to the difficulty of the electrons to move through the sample, and the

## ***Chapter 2. Experimental Methods***

---

surface acquires positive potential, meaning in a shift to higher binding energies when the sample is measured in the spectrometer.

This charge effect has to be corrected and this charge correction can be provided with certain elements that can be used as charge references. The most widely used is the adventitious carbon by setting the main line of the C 1s spectrum normally to 284.6 eV (although values ranging from 285.0 eV to 284.5 eV, depending of the researcher criteria) but there is the possibility to use other elements as well. In the present experiments, due to the presence of other carbon species that are not adventitious in the C 1s peak, the charge correction was mainly done using O 1s due to a well-known position for the studied oxygen species.

### *2.3.1.8. Transport of electrodes to XPS*

Measured electrodes at cycled to varying states of charge or discharge were transported to XPS machine for their measurement *ex situ*. The surface species formed by the electrochemical treatment are sensitive to oxygen and humidity (a small contact with air can modify the oxidation state of the elements present in the studied material). Therefore, in order to avoid any possible contact with air, a special transfer chamber was designed and constructed, as it is shown in **Figure 2.10**.

The transfer chamber has the possibility to be totally sealed in the glovebox with the samples in its inside, and then it is possible to transport it to the XPS chamber. Once the transfer chamber is connected to the XPS machine, ultra-high vacuum is created and that allows the measurement of electrochemically cycled electrodes without any air or moisture exposure.



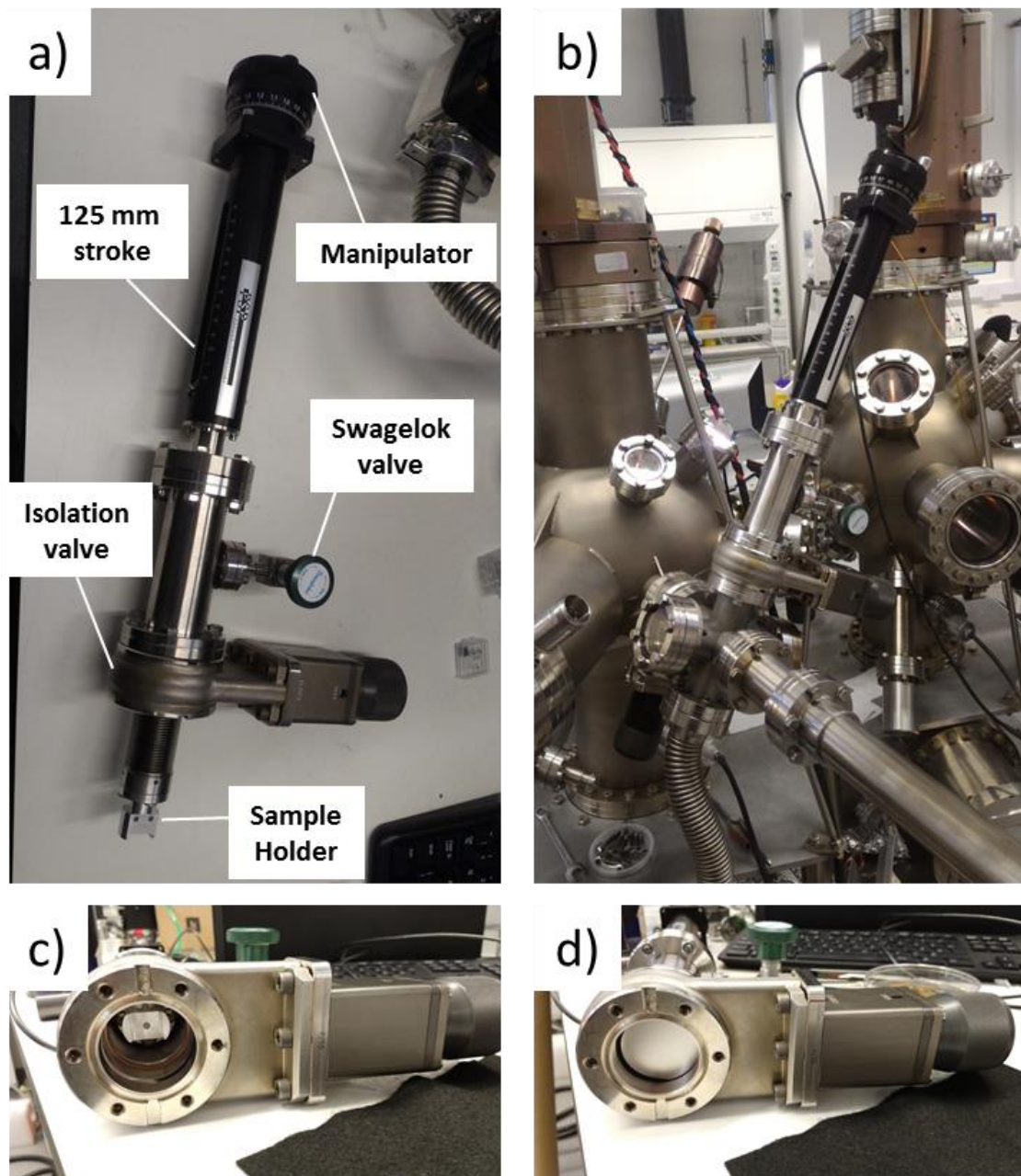


**Figure 2.10.** (a) Transfer chamber with its different components and (b) once it is connected to XPS. (c) Isolation valve when is open and (d) closed.

### 2.3.1.9. Experimental specifications

The XPS experiments presented in this thesis were performed in a standard ultrahigh vacuum surface science chamber consisting of a PSP Vacuum Technology electron

## Chapter 2. Experimental Methods

---

energy analyser (angle integrating  $\pm 10^\circ$ ) and a dual anode X-ray source. The base pressure of the system was  $2 \times 10^{-10}$  mbar, with hydrogen as the main residual gas in the chamber. The spectrometer was calibrated using Au 4f<sub>7/2</sub> at 83.9 eV. XPS spectra were fitted using Voigt functions after Shirley background removal and the overall resolution is 0.2 eV.

### 2.3.2. Hard X-Ray Photoelectron Spectroscopy

The photoemission process has a limiting factor after photon absorption known as inelastic mean free path of the electrons (IMFP<sub>e</sub>)<sup>38-40</sup> which is energy dependant and generally also dependant on a given material.

Tanuma *et. al*<sup>41</sup> could define a formula, known as TPP-2M model, which they could predict the depth of a given element, giving rise to an universal curve<sup>40, 42</sup> that shows that over the electron kinetic energy range 10 – 2000 eV (most of the XPS electron energies fall in this range), the IMFP<sub>e</sub> reaches a depth of few nanometres for a measured element, as can be observed in **Figure 2.11**, meaning that the majority of electrons contributing to the XPS signal are coming from the top few atomic layers of a sample.

Although X-rays penetrate at least several hundred of nm on the irradiated sample, only photoelectrons escaping from the surface are detected. Hence, information obtained by XPS is limited to around the outermost 10 nm, since photoelectrons ejected from deeper regions are stopped by inelastic scattering processes within the material, and this is why XPS is considered a surface sensitive technique. With higher photon energies, the kinetic energy of the photoelectrons can be increased, thus, increasing their mean free path and the penetration depth of the technique.

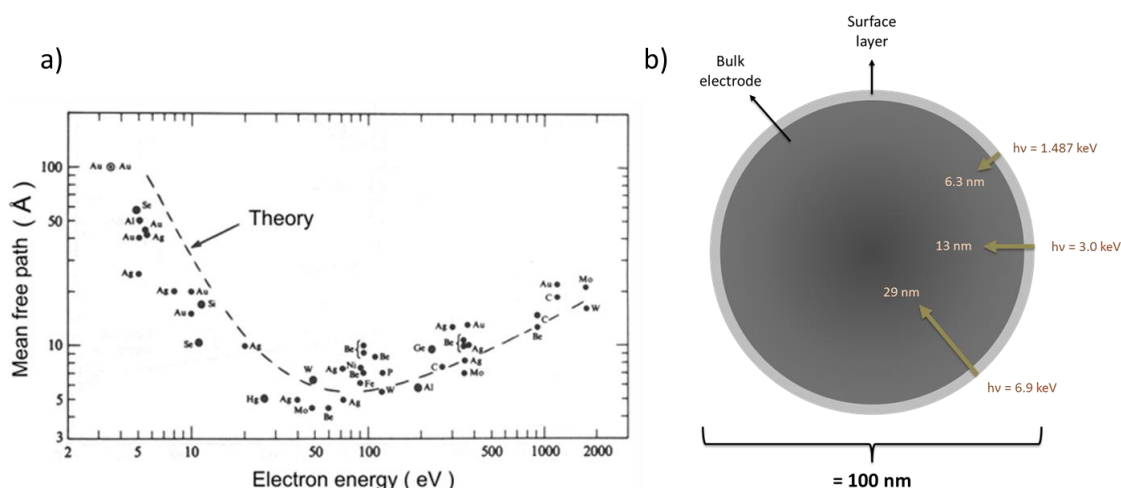


**Figure 2.11.** (a) Calculated inelastic mean free path of electrons in solids as a function of their energy: a compilation of a variety of experimental data given by the dots, and an interpolation formula given by a dash line.<sup>39, 43-45</sup> (b) Schematic view of XPS probe depths estimated for the O 1s core peak at increasing photon energies. Higher energy photons allow for probing much beyond the surface layer to provide bulk information from the ~100 nm-sized primary particles. The probe depths are defined as three times the  $\text{IMFP}_e$  (according to the TPP-2M model).<sup>46</sup>

In recent years there is an increasing number of new studies using an XPS-derived technique based on a synchrotron beamline, where it is possible to produce an excitation source with hard X-rays providing a kinetic energy beyond 2000 eV, which has a macroscopic penetration depth in the materials.<sup>47</sup>

Consequently, hard X-ray photoelectron spectroscopy (HAXPES) allows the study of bulk and buried interfaces up to several tens of nanometres depth based on kinetic energies up to 15 keV; an example of a HAXPES spectra is shown in **Figure 2.12**. Other advantage of this technique is the use of tuneable X-ray radiation provided by the synchrotron, meaning that the information depth can be changed and consequently electronic and compositional depth profiles can be obtained. HAXPES is a powerful

## Chapter 2. Experimental Methods

---

emerging technique for the determination of both the surface and bulk compositional, chemical and electronic properties.

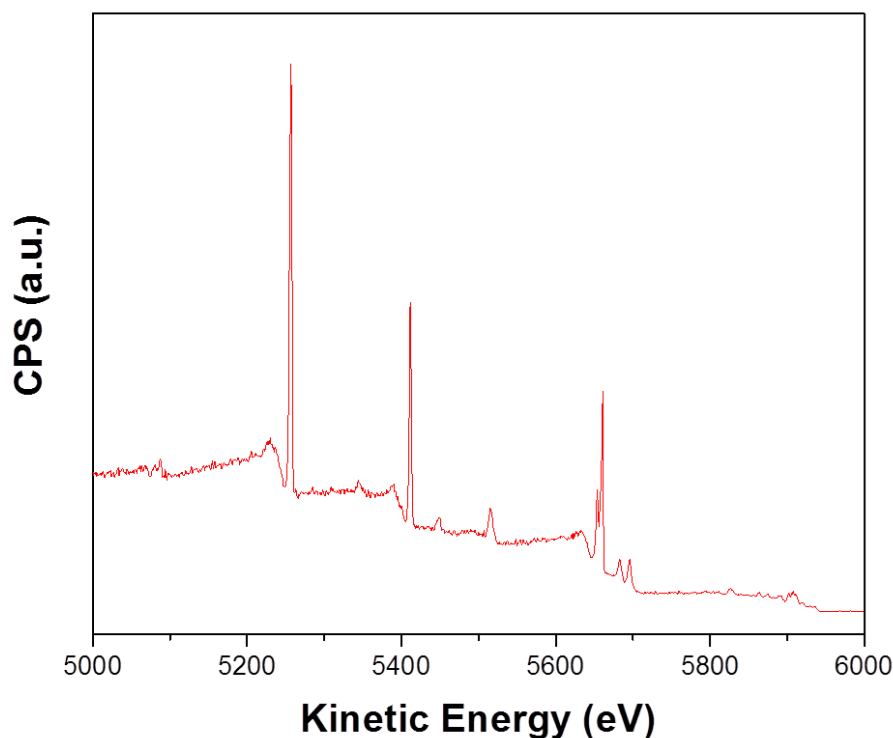


**Figure 2.12.** Example of measured HAXPES spectra for a studied material ( $\text{Li}_{4.15}\text{Ni}_{0.85}\text{WO}_6$ ) with a kinetic energy up to 6 keV. The binding energy of the main core electron peaks of every element in HAXPES appears at the same binding energy than in soft XPS according to equation (2.4).

HAXPES was measured at the I09 beamline at Diamond Light Source (Oxfordshire, UK). A double-crystal Si (111) monochromator was used to select photons with an energy of 2.1 and 6.45 keV. The resulting total experimental resolution was evaluated at each energy by measuring the Fermi edge of a polycrystalline gold reference sample and fitting the data to a Gaussian-broadened Fermi-Dirac distribution. The HAXPES end-station is equipped with a VG Scienta EW4000 electron analyser with a  $\pm 30^\circ$  angular acceptance.

Additional HAXPES measurements were carried out at beamline P09 of PETRAIII (Hamburg, Germany). The photon energy was set to 5947.9 eV using a Si(111) high heat load double-crystal primary monochromator and the (333) reflection of a Si double channel-cut post monochromator. The HAXPES end-station is equipped with a SPECS Phoibos 225 HV hemispherical analyser with a combined delayline and four channel micro-Mott spin detector. The resolution of the monochromator is better than 0.1 eV and the total resolution was set to 0.25 eV.

### 2.3.3. Raman microscopy

Raman microscopy is a vibrational technique and is used for obtaining chemical structural information down to the molecular level for a range of organic and inorganic compounds having Raman-active vibrational modes.

The Raman effect is an inelastic scattering of a light photon from analysed molecules due to changes in polarisability of molecule.<sup>48, 49</sup> This effect results in changes in the scattered photon wavelength. The Raman spectrum is a plot of intensity vs. the difference in Raman frequency from an incident photon, known as a Raman shift. Therefore, the Raman shift is independent of the incident photon frequency. An example of a Raman spectrum is represented in **Figure 2.13**.

The major requirement of Raman microscopy is to use a monochromatic light source, such as a laser in the visible, near IR or near ultraviolet ranges. Most of the wavelengths used for Raman analysis lie in the visible light range (400 – 700 nm), which has a good excitation efficiency.

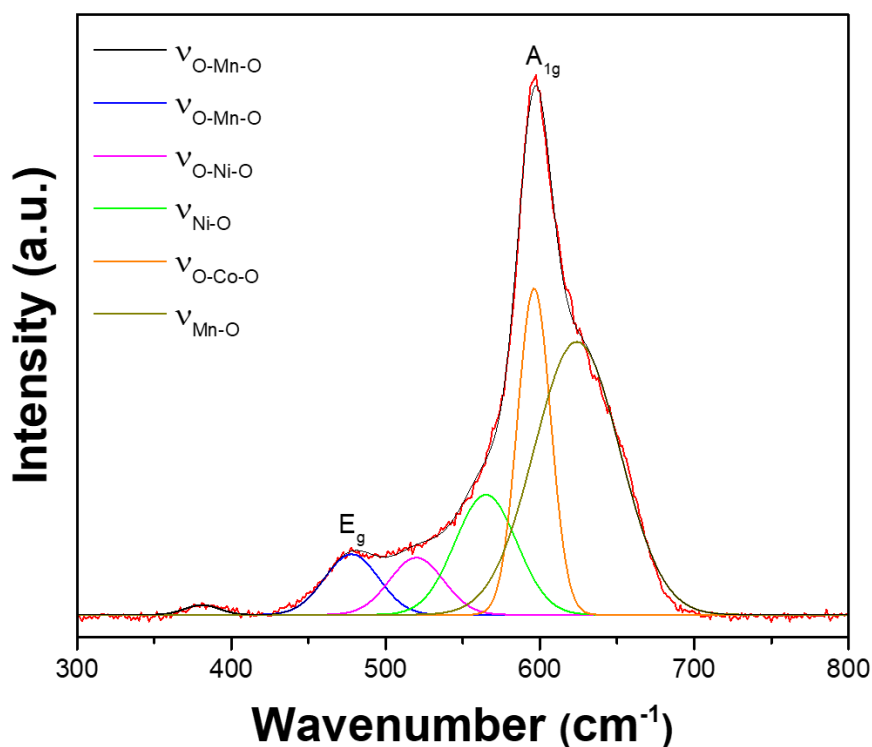


**Figure 2.13.** Example of Raman spectrum of  $\text{LiCo}_{1/3}\text{Ni}_{1/3}\text{Mn}_{1/3}\text{O}_2$  with the characteristic vibration bonds:  $\nu_{\text{Mn-O}}$  ( $381 \text{ cm}^{-1}$ ),  $\nu_{\text{O-Mn-O}}$  ( $478 \text{ cm}^{-1}$ ),  $\nu_{\text{O-Ni-O}}$  ( $520 \text{ cm}^{-1}$ ),  $\nu_{\text{Ni-O}}$  ( $565 \text{ cm}^{-1}$ ),  $\nu_{\text{Co-O}}$  ( $597 \text{ cm}^{-1}$ ) and  $\nu_{\text{Mn-O}}$  ( $624 \text{ cm}^{-1}$ ), as well as the  $E_g$  ( $480 \text{ cm}^{-1}$ ) and  $A_{1g}$  bands ( $600 \text{ cm}^{-1}$ ).<sup>50-52</sup>

Raman spectra were collected with a 633 nm wavelength laser using a Raman system (Renishaw inVia Reflex) with a microscope focused through a 50x objective lens (Leica). The estimated power on the sample was 0.43 mW with 200 s exposure time and two accumulations. For *ex situ* Raman measurements, performed at different stages of galvanostatic cycling, and to avoid oxygen and moisture contamination, an air-tight Raman cell (ECC-Opto-STD, El-Cell, GmbH) was assembled inside an Ar-filled glovebox.

### 2.3.4. X-ray diffraction

X-ray diffraction (XRD) is a well-established analytical and non-destructive technique that can determine the structure of crystalline solids, via the diffraction of incident X-rays by the electron cloud around atoms in the crystal structure and can provide information on unit cell dimensions, being capable of collecting both quantitative and qualitative phase analysis data applying Bragg's Law<sup>53</sup>:

$$n\lambda = 2 d_{hkl} \sin\theta \quad (2.5)$$

where  $n$  is an integer,  $\lambda$  is the wavelength of the radiation,  $d_{hkl}$  is the distance between lattice planes and  $\theta$  is the angle of incidence. (h,k,l) values represent the Miller indices used to define planes of atoms, whereby (h,k,l) are the reciprocal of the plane's intercepts on the x-, y-, and z-axes in terms of lattice constants a, b, and c.

Powder X-ray diffraction patterns were collected on a Rigaku SmartLab® diffractometer operating in transmission mode with Cu K $\alpha_1$  radiation.

### 2.3.5. X-ray absorption spectroscopy

X-ray absorption spectroscopy (XAS) is a powerful technique to measure the atomic structure of electrode materials because it provides information about the local environment of an element, while XRD provides information on the overall structure of a material. This analytical tool measures the energy dependence of the X-ray absorption coefficient at and above the absorption edge of the desired element in electrode materials.<sup>54</sup> XAS is a beneficial tool for the analytical characterisation of materials because it is element specific and sensitive to minimal concentrations. Data acquisition is quite fast due to the application of high-energy synchrotron radiation, which also facilitates the *in situ* testing because the probing and signalling source are high-intensity

## Chapter 2. Experimental Methods

---

X-rays.<sup>55, 56</sup> XAS can be implemented in gases, liquids and solids (both amorphous and crystalline).

Depending on the analytical application, this technique is divided into two parts:

1) X-ray absorption near-edge structure (XANES): the most widely used, provides quantitative and qualitative information about the electronic transition, sites symmetries, and change in the oxidation state of the probed element.<sup>57</sup> An example of this spectroscopy is exposed in **Figure 2.14**.

2) Extended X-ray absorption fine structure (EXAFS): provides information about the local environment of an element regarding its coordination numbers, bond length and the chemical identity of the nearest atom.<sup>56, 58</sup>

The X-ray absorption spectra showed in this thesis were measured at the B18 beamline at Diamond Light Source (Oxfordshire, UK).

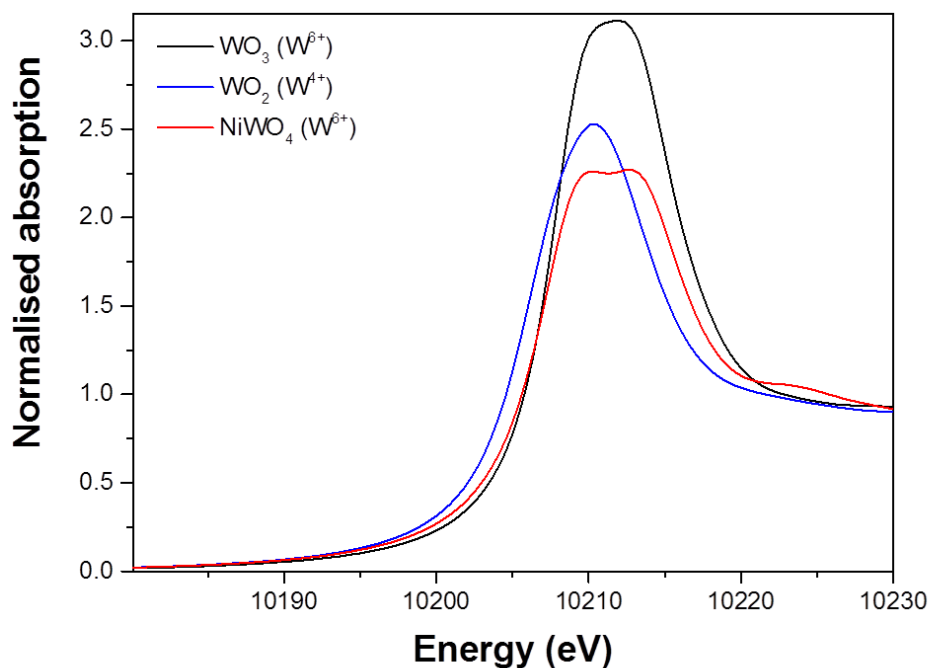


**Figure 2.14.** Example of X-ray absorption near-edge structure of different W-based compounds.



### **2.3.6. Scanning electron microscopy**

Scanning electron microscopy (SEM) is a technique used in the investigation of the size, morphology, texture and topography of samples on the micro and nanometre scale, producing detailed two-dimensional images.<sup>59</sup>

SEM produces images by scanning the sample with a high-energy beam of electrons. As the electrons interact with the sample, they produce secondary electrons, backscattered electrons, and characteristic X-rays. These signals are collected by one or more detectors to form images, which are then displayed on the computer screen. When the electron beam hits the surface of the sample, it penetrates the sample to a depth of a few microns, depending on the accelerating voltage and the density of the sample. Many signals, like secondary electrons and X-rays, are produced as a result of this interaction inside the sample.

The characteristic emitted electromagnetic radiation generated in SEM may be analysed to provide information regarding the elemental composition of the sample. This technique is known as Energy Dispersive X-ray spectroscopy (EDX).<sup>60</sup>

SEM images reported in this thesis were recorded with a JEOL JSM-7001F field emission electron microscope.

### **2.3.7. Inductively couple plasma optical emission spectroscopy**

Inductively couple plasma optical emission spectroscopy (ICP-OES) is an analytical technique that can provide quantitative bulk elemental composition and elemental concentrations of a wide variety of sample types, including powders, solids, liquids and suspensions.

Usually, solid samples are dissolved using a combination of acids or aqueous

## ***Chapter 2. Experimental Methods***

---

solutions (commonly known as ‘digestion’), with a final concentration between 10 and 100 ppm. The resulting sample solution is then nebulised into the core of an inductively couple argon plasma with temperatures up to 9000 K.

At high temperatures, the nebulised solution is vaporised and the species of interest are atomised, ionised and thermally excited. The element can be detected and quantitated with optical emission spectrometer (OES), which measures the intensity of radiation emitted by the specific element at the corresponding wavelength from the thermally excited atoms or ions. Elemental concentrations can be determined by comparing the intensity measured with those for calibration standards (i.e. calculating the stoichiometry using the atomic weight of each element).

This type of elemental analysis is very useful for heavy elements such as transition metals. However, it is not possible to use this technique to measure accurately the following elements: carbon, nitrogen, hydrogen, oxygen and halogens.

ICP-OES analyses were carried out in Agilent 5110 ICP-OES spectrometer.

### **2.3.8. Nitrogen adsorption/desorption isotherms**

Gas adsorption analysis is commonly used for surface area and porosity measurements. This involves exposing solid materials to gases under a variety of conditions and evaluating the weight of the sample volume. Brunauer-Emmett-Teller (BET) analysis is the most common method used for determining the surface area of either powders or porous materials.<sup>61</sup> The theory can be applied to systems with multilayer adsorption and adsorption/desorption isotherms are usually carried out with non-reactive gases, most commonly nitrogen at liquid condition at 77 K. The concept of the BET analysis is based on the following assumptions: 1) gas molecules physically

adsorb on a solid in layers up to infinite dimensions, 2) there is no interaction between the adsorbed layers and 3) the Langmuir theory (generally applied to monolayer adsorption) applies to each individual layer.<sup>62-64</sup>

One of the advantages of this technique is that can be used for the calculation of the surface area of solids by physical adsorption of gas molecules. The total surface area ( $S_{total}$ ) can be calculated using the following equation:

$$S_{total} = \frac{v_m N s}{V} \quad (2.6)$$

where  $v_m$  is the monolayer volume of the adsorbate gas (in units of the molar volume),  $N$  is Avogadro's number,  $s$  is adsorption cross section of the adsorbing species and  $V$  is molar volume of adsorbate gas.

And the specific surface area ( $S_{BET}$ ) can be obtained easily according to:

$$S_{BET} = \frac{S_{total}}{a} \quad (2.7)$$

where  $a$  is the mass of adsorbent (in grams).

BET analysis reported in this thesis were measured in Micromeritics 3Flex gas sorption analyser.

### 2.4. Preparation of the samples

Different synthetic methods were used throughout this thesis to prepare the different studied samples.

In *Chapter 3*, four  $\text{LiNi}_{1/3}\text{Co}_{1/3}\text{Mn}_{1/3}\text{O}_2$  samples were synthesised via two different techniques: hydroxide co-precipitation and resorcinol-formaldehyde sol-gel polymerisation.

## ***Chapter 2. Experimental Methods***

---

Hydroxide co-precipitation method consisted of mixing a stoichiometric ratio of manganese, nickel and cobalt nitrates and adding dropwise in a stoichiometric amount of lithium hydroxide monohydrate solution with a constant stirring rate. Another sample was prepared with a previous treatment via addition of a small pipette at the bottom of the burette in order to have approximately half a size of a normal droplet. The final products were filtrated and washed with water until the pH reached 7, and were left in an oven at 70 °C to evaporate away the remaining water. The filtrate was ground using an agate mortar and a pestle with a stoichiometric amount of lithium hydroxide monohydrate powder (i.e. a ratio of 1:1.05 with the starting composition) and then pressed into a 10 mm diameter pellet by applying uniaxial pressure of 1-2 tons. The pellet was then heated in a furnace at 450 °C for 4 hours with a heating rate of 130 °C h<sup>-1</sup>. After leaving to cool down to room temperature, the pellet was re-ground in the mortar and pressed again into a pellet using the same conditions explained before, then re-heated to 950 °C for 12 hours in air with a heating rate of 130 °C h<sup>-1</sup> whereafter the pellet was ground in the mortar one more time to obtain finally a fine, black powder.

Resorcinol-formaldehyde sol-gel polymerisation method consisted of mixing resorcinol and formaldehyde in a molar ratio of 1:1.5 in distilled water and then added to a mixture of lithium, manganese, nickel and cobalt acetates (in a molar ratio of 3:1:1:1) in distilled water until the polymerisation between resorcinol and formaldehyde starts after heating the mixture at 60 °C. The polymer (often called as “RF gel”)<sup>65</sup> was then introduced in a furnace and heated to 200 °C until the calcination of all the contained carbon in the material takes place and then the resulting product was ground in the mortar. An additional calcination and re-ground were done for one of the two studied samples. After these steps, the powders were heated in a furnace to 950 °C for 14 hours in air with

a heating rate of  $180\text{ }^{\circ}\text{C h}^{-1}$ , and the final products were ground in the mortar as a final step.

In *Chapter 4*,  $\text{Li}_{1.2}\text{Ni}_{0.13}\text{Mn}_{0.54}\text{Co}_{0.13}\text{O}_2$  and  $\text{Li}_{1.2}\text{Ni}_{0.32}\text{Mn}_{0.4}\text{Co}_{0.08}\text{O}_2$  samples were prepared using resorcinol-formaldehyde sol-gel polymerisation in the same way that was described previously, with the appropriate ratio of the metal acetates, and an additional calcination at  $200\text{ }^{\circ}\text{C}$  and re-ground. The main difference consisted in the final step, where the powders were heated in the furnace to  $480\text{ }^{\circ}\text{C}$  for 3 hours and then to  $800\text{ }^{\circ}\text{C}$  for 6 hours with a heating rate of  $130\text{ }^{\circ}\text{C h}^{-1}$  in both cases. The final products were then ground in the mortar, obtaining a black powder for  $\text{Li}_{1.2}\text{Ni}_{0.32}\text{Mn}_{0.4}\text{Co}_{0.08}\text{O}_2$  and dark brown powder for  $\text{Li}_{1.2}\text{Ni}_{0.13}\text{Mn}_{0.54}\text{Co}_{0.13}\text{O}_2$  due to its high content in Mn.

In *Chapter 5*, the non-stoichiometric  $\text{Li}_{4.15}\text{Ni}_{0.85}\text{WO}_6$  was provided by Matthew Rosseinsky's group, in the Department of Chemistry at University of Liverpool. They synthesised the sample using  $\text{Li}_2\text{CO}_3$ , NiO and  $\text{WO}_3$  as precursors.

The synthesis was carried out by a classical solid-state method where these starting materials were mixed with a 10% molar excess of  $\text{Li}_2\text{CO}_3$  (ratio of 4.56:0.85:1) to compensate for  $\text{Li}_2\text{O}$  volatility during high-temperature synthesis. The mix was done using a planetary mill (350 rpm, using 10 mm diameter zirconia balls) in propanol for 2 hours. The milled samples were then dried using a crystallising dish on a stirrer hotplate and the resulting powder was ground in a pestle and mortar. A 10 or 13 mm diameter pellet of the mixed reactants was pressed by applying uniaxial pressure of 1-2 tons to produce  $\sim 1$  g of material, and then loaded into an alumina crucible. Part of the remaining precursor mixture surrounding the pellet in the alumina crucible was used as a sacrificial powder, in order to minimise the effects of  $\text{Li}_2\text{O}$  volatilisation. The final synthetic conditions used for these materials was two firings in air using a box furnace at  $1000\text{ }^{\circ}\text{C}$

## ***Chapter 2. Experimental Methods***

---

for 24 h (48 h in total) at a heating and cooling rate of  $300\text{ }^{\circ}\text{C h}^{-1}$ . The pellet was ground and re-pressed and the sacrificial powder was ground separately between firings. The final product is a brown-black powder.

Additional processing was necessary in order to successfully cast this cathode material onto the aluminium current collector to produce coin cells for testing. The particle size was reduced further by milling in the planetary mill using isopropanol and 5 mm diameter zirconia balls at 350 rpm, obtaining a final particle size of 0.5-3  $\mu\text{m}$  (while the initial particle size was 5-20  $\mu\text{m}$ ) and a brown-coloured powder. This ball-milling also helps to achieve better electrochemical performance.

## 2.5. References

1. V. Srinivasan and C. Wang, *J. Electrochem. Soc.*, 2003, **150**, A98-A106.
2. J. Gnanaraj, Y. S. Cohen, M. Levi and D. Aurbach, *J. Electroanal. Chem.*, 2001, **516**, 89-102.
3. J. Shim and K. A. Striebel, *J. Power Sources*, 2003, **119**, 934-937.
4. P. Verma, P. Maire and P. Novák, *Electrochim. Acta*, 2010, **55**, 6332-6341.
5. E. Peled, *J. Electrochem. Soc.*, 1979, **126**, 2047-2051.
6. A. Andersson, D. Abraham, R. Haasch, S. MacLaren, J. Liu and K. Amine, *J. Electrochem. Soc.*, 2002, **149**, A1358-A1369.
7. D. Aurbach, I. Weissman, A. Schechter and H. Cohen, *Langmuir*, 1996, **12**, 3991-4007.
8. V. A. Agubra and J. W. Fergus, *J. Power Sources*, 2014, **268**, 153-162.
9. D. Aurbach, M. D. Levi, E. Levi, H. Teller, B. Markovsky, G. Salitra, U. Heider and L. Heider, *J. Electrochem. Soc.*, 1998, **145**, 3024-3034.
10. D. Aurbach, *J. Power Sources*, 2000, **89**, 206-218.
11. O. Haik, N. Leifer, Z. Samuk-Fromovich, E. Zinigrad, B. Markovsky, L. Larush, Y. Goffer, G. Goobes and D. Aurbach, *J. Electrochem. Soc.*, 2010, **157**, A1099-A1107.
12. K. Edström, T. Gustafsson and J. O. Thomas, *Electrochim. Acta*, 2004, **50**, 397-403.
13. P. Biensan, B. Simon, J. Peres, A. De Guibert, M. Broussely, J. Bodet and F. Perton, *J. Power Sources*, 1999, **81**, 906-912.
14. J. Drogenik, M. Gaberscek, R. Dominko, F. W. Poulsen, M. Mogensen, S. Pejovnik and J. Jamnik, *Electrochim. Acta*, 2003, **48**, 883-889.

## Chapter 2. Experimental Methods

---

15. J.-H. Lee, U. Paik, V. A. Hackley and Y.-M. Choi, *J. Electrochem. Soc.*, 2005, **152**, A1763-A1769.
16. H. Buqa, M. Holzapfel, F. Krumeich, C. Veit and P. Novák, *J. Power Sources*, 2006, **161**, 617-622.
17. B. Lestriez, S. Bahri, I. Sandu, L. Roué and D. Guyomard, *Electrochem. Commun.*, 2007, **9**, 2801-2806.
18. J. Li, R. Lewis and J. Dahn, *Electrochem. Solid-State Lett.*, 2007, **10**, A17-A20.
19. L. El Ouatani, R. Dedryvère, J.B. Ledeuil, C. Siret, P. Biensan, J. Desbrières and D. Gonbeau, *J. Power Sources*, 2009, **189**, 72-80.
20. S. Lux, F. Schappacher, A. Balducci, S. Passerini and M. Winter, *J. Electrochem. Soc.*, 2010, **157**, A320-A325.
21. J. F. Watts, *Surface science techniques*, 1994, 5-23.
22. D. Briggs and J. T. Grant, *Surface analysis by Auger and X-ray photoelectron spectroscopy*, IM publications, 2003.
23. J. C. Dupin, D. Gonbeau, H. Benqlilou-Moudden, P. Vinatier and A. Levasseur, *Thin Solid Films*, 2001, **384**, 23-32.
24. A. Einstein, *Am. J. Phys*, 1965, **33**, 367.
25. Y.-W. Chung, *Practical guide to surface science and spectroscopy*, Academic Press, 2001.
26. P. Citrin, P. Eisenberger, W. Marra, T. Åberg, J. Utriainen and E. Källne, *Phys. Rev. B*, 1974, **10**, 1762.
27. D. A. Shirley, *Phys. Rev. B*, 1972, **5**, 4709.
28. L. Ley, S. Kowalczyk, R. Pollak and D. Shirley, *Phys. Rev. Lett.*, 1972, **29**, 1088.



29. S. Hofmann, *Auger-and X-ray photoelectron spectroscopy in materials science: a user-oriented guide*, Springer Science & Business Media, 2012.
30. J. Chastain, R. C. King and J. Moulder, *Handbook of X-ray photoelectron spectroscopy*, Physical Electronics Division, 1992.
31. R. Winkler, *Advances in Solid State Physics*, Springer Science & Business Media, 2003, 211-223.
32. B. V. Crist, *Handbook of Monochromatic XPS Spectra, The Elements of Native Oxides*, Wiley-VCH, 2000.
33. J. Rumble Jr, D. Bickham and C. Powell, *Surf. Interface Anal.*, 1992, **19**, 241-246.
34. J. Végh, *J. Electron. Spectrosc. Relat. Phenom.*, 2006, **151**, 159-164.
35. C. D. Wagner, *The NIST X-ray photoelectron spectroscopy (XPS) database*, 1991.
36. C. D. Wagner, *J. Electron. Spectrosc. Relat. Phenom.*, 1980, **18**, 345-349.
37. T. L. Barr and S. Seal, *J. Vac. Sci. Technol. A*, 1995, **13**, 1239-1246.
38. D. P. Woodruff, *Modern techniques of surface science*, Cambridge university press, 2016.
39. S. Tanuma, C. J. Powell and D. R. Penn, *Surf. Interface Anal.*, 1997, **25**, 25-35.
40. M. P. Seah and W. Dench, *Surf. Interface Anal.*, 1979, **1**, 2-11.
41. S. Tanuma, C. J. Powell and D. R. Penn, *Surf. Interface Anal.*, 2003, **35**, 268-275.
42. H. Tokutaka, K. Nishimori and H. Hayashi, *Surf. Sci.*, 1985, **149**, 349-365.
43. S. Tanuma, C. J. Powell and D. R. Penn, *Surf. Interface Anal.*, 1988, **11**, 577-589.
44. S. Tanuma, C. J. Powell and D. R. Penn, *Surf. Interface Anal.*, 1994, **21**, 165-176.
45. S. Tanuma, *Surf. Interface Anal.*, 2011, **43**, 689.
46. S. Tanuma, C. J. Powell and D. R. Penn, *Surf. Sci.*, 1987, **192**, L849-L857.
47. J. Rubio-Zuazo and G. Castro, *Surf. Interface Anal.*, 2008, **40**, 1438-1443.

## Chapter 2. Experimental Methods

---

48. C. V. Raman and K. S. Krishnan, *Nature*, 1928, **121**, 501.
49. C. V. Raman and K. S. Krishnan, *Nature*, 1928, **121**, 711.
50. K. Ben-Kamel, N. Amdouni, A. Mauger and C. M. Julien, *J. Alloys Compd.*, 2012, **528**, 91-98.
51. C. M. Julien and M. Massot, *Mater. Sci. Eng. B*, 2003, **100**, 69-78.
52. X. Zhang, A. Mauger, Q. Lu, H. Groult, L. Perrigaud, F. Gendron and C. M. Julien, *Electrochim. Acta*, 2010, **55**, 6440-6449.
53. W. L. Bragg, *Scientia*, 1929, **23** (45), 153.
54. P. Shearing, Y. Wu, S. J. Harris and N. Brandon, *Electrochem. Soc. Interface*, 2011, **20**, 43-47.
55. S. Khalid, W. Caliebe, P. Siddons, I. So, B. Clay, T. Lenhard, J. Hanson, Q. Wang, A. Frenkel and N. Marinkovic, *Rev. Sci. Instrum.*, 2010, **81**, 015105.
56. J. Stötzel, D. Lützenkirchen-Hecht, E. Fonda, N. De Oliveira, V. Briois and R. Frahm, *Rev. Sci. Instrum.*, 2008, **79**, 083107.
57. C. Bressler and M. Chergui, *Chem. Rev.*, 2004, **104**, 1781-1812.
58. A. Mignani, B. Ballarin, M. Giorgetti, E. Scavetta, D. Tonelli, E. Boanini, V. Prevot, C. Mousty, and A. Iadecola, *J. Phys. Chem. C*, 2013, **117** (31), 16221-16230.
59. R. E. Lee, *Scanning electron microscopy and X-ray microanalysis*, PTR Prentice Hall, 1993.
60. D. Shindo and T. Oikawa, *Analytical electron microscopy for materials science*, Springer, 2002, 81-102.
61. K. K. Aligizaki, *Pore structure of cement-based materials*, CRC Press, 2014.
62. K. Sing, *Colloids Surf. A*, 2001, **187**, 3-9.

## *Chapter 2. Experimental Methods*

---

63. Y. Xi, Z. P. Bažant and H. M. Jennings, *Adv. Cem. Based Mater.*, 1994, **1**, 248-257.
64. K. S. Sing, *Adv. Colloid Interface Sci.*, 1998, **76**, 3-11.
65. J. P. Lewicki, C. A. Fox and M. A. Worsley, *Polymer*, 2015, **69**, 45-51.

# Chapter 3.

## **Effect of the synthetic routes on the surface properties and electrochemical performance of $\text{LiNi}_{1-x-y}\text{Co}_x\text{Mn}_y\text{O}_2$**

*"Life finds a way."*

Ian Malcolm

*Jurassic Park*

### **3.1. Overview of the chapter**

Mixed metal layered transition metal oxides ( $\text{LiNi}_{1-x-y}\text{Co}_x\text{Mn}_y\text{O}_2$ ) are particularly promising positive electrode materials, due to their higher capacity, lower cost and safety over  $\text{LiCoO}_2$ .<sup>1-3</sup>

The electrochemical properties of a chosen material can be influenced by the synthetic routes used for obtaining the final product.<sup>4-6</sup> Although the crystal structure can remain unchanged, the electrochemical properties can vary between one sample and another depending of the chosen synthetic method, and this is linked directly with the surface of a studied material.

Understanding the surface chemistry is critical in developing synthetic methods that allow greater stability within these classes of materials to permit their future commercialisation into applications where long lifetimes are required.<sup>7-10</sup>

### ***Chapter 3. Effect of the synthetic routes on the surface properties and electrochemical performance of $\text{LiNi}_{1-x-y}\text{Co}_x\text{Mn}_y\text{O}_2$***

---

In this chapter,  $\text{LiNi}_{1-x-y}\text{Co}_x\text{Mn}_y\text{O}_2$  is synthesised via different routes that led to different surface properties. These materials are characterised for their structural, electrochemical and surface properties using XPS. Commonalities and trends in surface properties and electrochemical performance in particular are discussed and rationalised.

#### **3.2. Introduction**

Layered lithium metal oxides are widely used as positive electrodes in rechargeable batteries due to their ability to reversibly deintercalate / intercalate  $\text{Li}^+$  ions.<sup>11</sup> There is one promising material in the  $\text{LiNi}_{1-x-y}\text{Co}_x\text{Mn}_y\text{O}_2$  series:  $\text{LiCo}_{1/3}\text{Ni}_{1/3}\text{Mn}_{1/3}\text{O}_2$ , which has been widely studied in the last years.<sup>3, 12, 13</sup> This material is highly dependent of the used synthetic route, meaning in a big change on the electrochemical properties according to the type of used synthesis.

The most common synthetic method used in academia and in commercial products is solid-state synthesis,<sup>14, 15</sup> but this type of synthesis has several issues like the production of impure products with poor electrochemical properties.<sup>16-18</sup> Additionally, the precursors are highly sensitive to reaction conditions, meaning that the reproducibility becomes very difficult. This is also problematic with the co-precipitation methods, which is dependant of the precursors that are used, and the results can vary each other if the precursors are for example metal hydroxides, metal carbonates or metal nitrates.<sup>4, 19-21</sup>

On the other hand, the use of resorcinol-formaldehyde sol-gel polymerisation synthesis results in a simple but good technique, which can be reproduced easily and the stoichiometry of the final product is accurate.<sup>22</sup> Furthermore, materials synthesised via sol-gel have superior electrochemical results such as improved capacity retention at high charge / discharge rates, and an increase in capacity overpassing  $200 \text{ mAh g}^{-1}$ , while

### ***Chapter 3. Effect of the synthetic routes on the surface properties and electrochemical performance of $\text{LiNi}_{1-x-y}\text{Co}_x\text{Mn}_y\text{O}_2$***

---

materials synthesised via more traditional methods usually do not obtain capacities higher than  $180 \text{ mAh g}^{-1}$ . This is due to the homogeneity promoted by the starting reactants solution and a better control in the particle size due to the introduction of a carbon source.<sup>23-26</sup>

In this chapter, the electrochemical performance and surface characterisation of four  $\text{LiNi}_{1/3}\text{Co}_{1/3}\text{Mn}_{1/3}\text{O}_2$  samples synthesised by two different methods are presented, according to the synthesis conditions described in **Chapter 2**: hydroxide co-precipitation synthesis with the addition of bigger (CP1) and smaller drops (CP2) from the metal nitrates to the LiOH solution, and resorcinol-formaldehyde sol-gel polymerisation synthesis with only one (SG1) and two calcinations (SG2) at  $200^\circ\text{C}$ . The obtained results are compared with a commercial sample (COM) synthesised via a solid-state route.

## **3.3. Results**

### **3.3.1. Crystal structure and morphology**

Elemental analysis in ICP-OES shows that all the synthesised samples have a stoichiometry similar to the  $\text{LiNi}_{1/3}\text{Mn}_{1/3}\text{Co}_{1/3}\text{O}_2$  standard, with some deviations such as higher amount of Li in the case of the co-precipitation samples (1.105 and 1.051 for CP1 and CP2, respectively) and a lower amount of Li for the sol-gel polymerisation samples (0.951 and 0.994 for SG1 and SG2, respectively) as shown in **Table 3.1**.

In the case of Ni, Mn and Co, lower values than the  $\text{LiNi}_{1/3}\text{Mn}_{1/3}\text{Co}_{1/3}\text{O}_2$  standard are observed for both CP1 and CP2 while the sol-gel samples are more precise, although both Co and Mn are slightly higher for both SG1 and SG2. For the commercial sample, the obtained values are closer to the standard values, with slight variations in the case of both Co and Mn.

***Chapter 3. Effect of the synthetic routes on the surface properties and electrochemical performance of  $\text{LiNi}_{1-x-y}\text{Co}_x\text{Mn}_y\text{O}_2$***

**Table 3.1.** Elemental analysis of the different samples using ICP-OES, with an error of  $\pm 0.004$ .

Oxygen is assumed to be 2 due to the impossibility to be measured using this technique.

Sample	Li	Ni	Co	Mn
Standard	1	0.333	0.333	0.333
CP1	1.10(5)	0.29(2)	0.29(2)	0.31(2)
CP2	1.05(1)	0.31(1)	0.31(3)	0.32(5)
SG1	0.95(1)	0.33(6)	0.35(9)	0.35(4)
SG2	0.99(4)	0.32(8)	0.34(8)	0.33(0)
COM	0.99(9)	0.33(1)	0.32(5)	0.34(7)

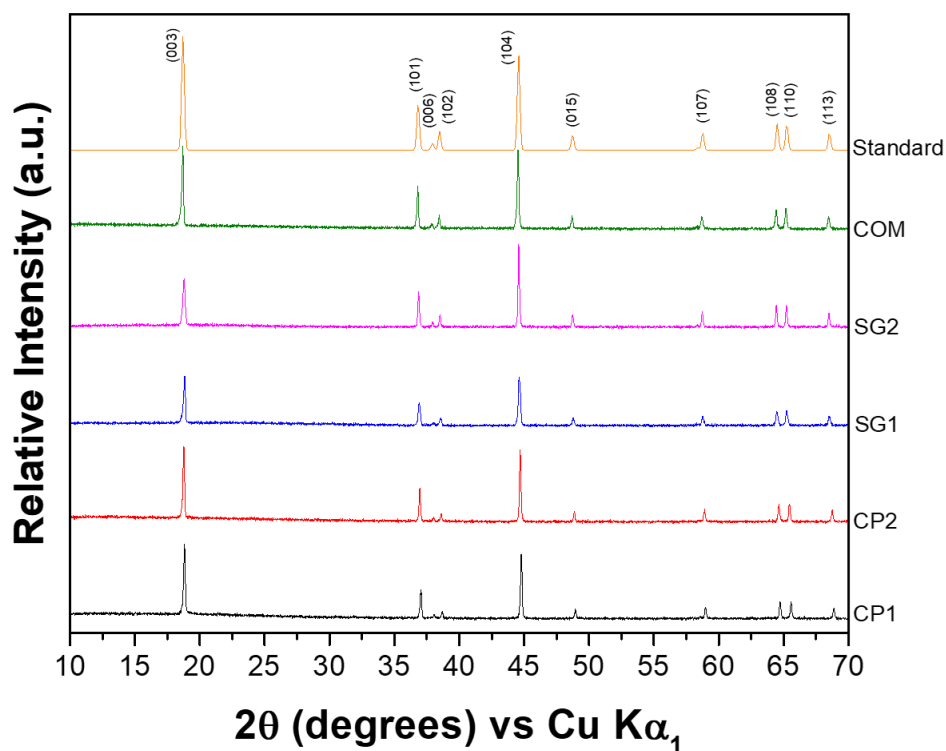


**Figure 3.1.** PXRD patterns of the different samples and their comparison with the literature standard (Code 171750 in ICSD database).<sup>27</sup>

### ***Chapter 3. Effect of the synthetic routes on the surface properties and electrochemical performance of $\text{LiNi}_{1-x-y}\text{Co}_x\text{Mn}_y\text{O}_2$***

---

**Figure 3.1.** shows PXRD (powder x-ray diffraction) patterns of the samples. These are in agreement with the literature standard<sup>27</sup> (Code 171750 in ICSD database), which confirms that: 1) There is no carbon in the structure. 2) All the peaks are sharp and well-defined, suggesting that the prepared compounds are well-crystallised. 3) It confirms that all the samples follow the layered structure, which is a hexagonal  $\alpha\text{-NaFeO}_2$  crystal structure type with space group  $R\bar{3}m$ , with alternating layer of edge-sharing  $\text{LiO}_6$ - and  $\text{MO}_6$ -octahedra, respectively.<sup>24, 28-30</sup> 4) There is a highly ordered hexagonal lattice with  $\text{Li}^+$  ions at the 3a site, transition metal ions at the 3b site and oxygen ions at the 6c site.<sup>28</sup> All the samples prepared, are single-phase materials.<sup>31</sup>

In **Table 3.2.** the cell parameters are presented. The calculated lattice constants using Rietveld refinement are in good agreement with the literature standard values.<sup>24, 27-30</sup> All samples have a  $c/a$  ratio very similar to the value obtained from the literature standard (4.975), which suggests a well-ordered layered structure with little variations due to the difference in preparation conditions.<sup>32</sup>

**Table 3.2.** Cell parameters of the different studied samples. The lattice constants were calculated using Rietveld refinement in FullProf Suite, with an error of  $\pm 0.003$  Å.

<b>Sample</b>	<b>a (Å)</b>	<b>c (Å)</b>	<b>c/a</b>
Standard	2.860	14.227	4.975
CP1	2.84(8)	14.19(6)	4.98(4)
CP2	2.85(1)	14.20(5)	4.98(2)
SG1	2.86(4)	14.25(5)	4.97(8)
SG2	2.86(4)	14.25(5)	4.97(8)
COM	2.86(0)	14.23(1)	4.97(7)



### ***Chapter 3. Effect of the synthetic routes on the surface properties and electrochemical performance of $\text{LiNi}_{1-x-y}\text{Co}_x\text{Mn}_y\text{O}_2$***

A comparison of the morphology of the studied samples via scanning electron microscopy is shown in **Figure 3.2.** with low and high magnification (1  $\mu\text{m}$  and 100 nm scale, respectively).

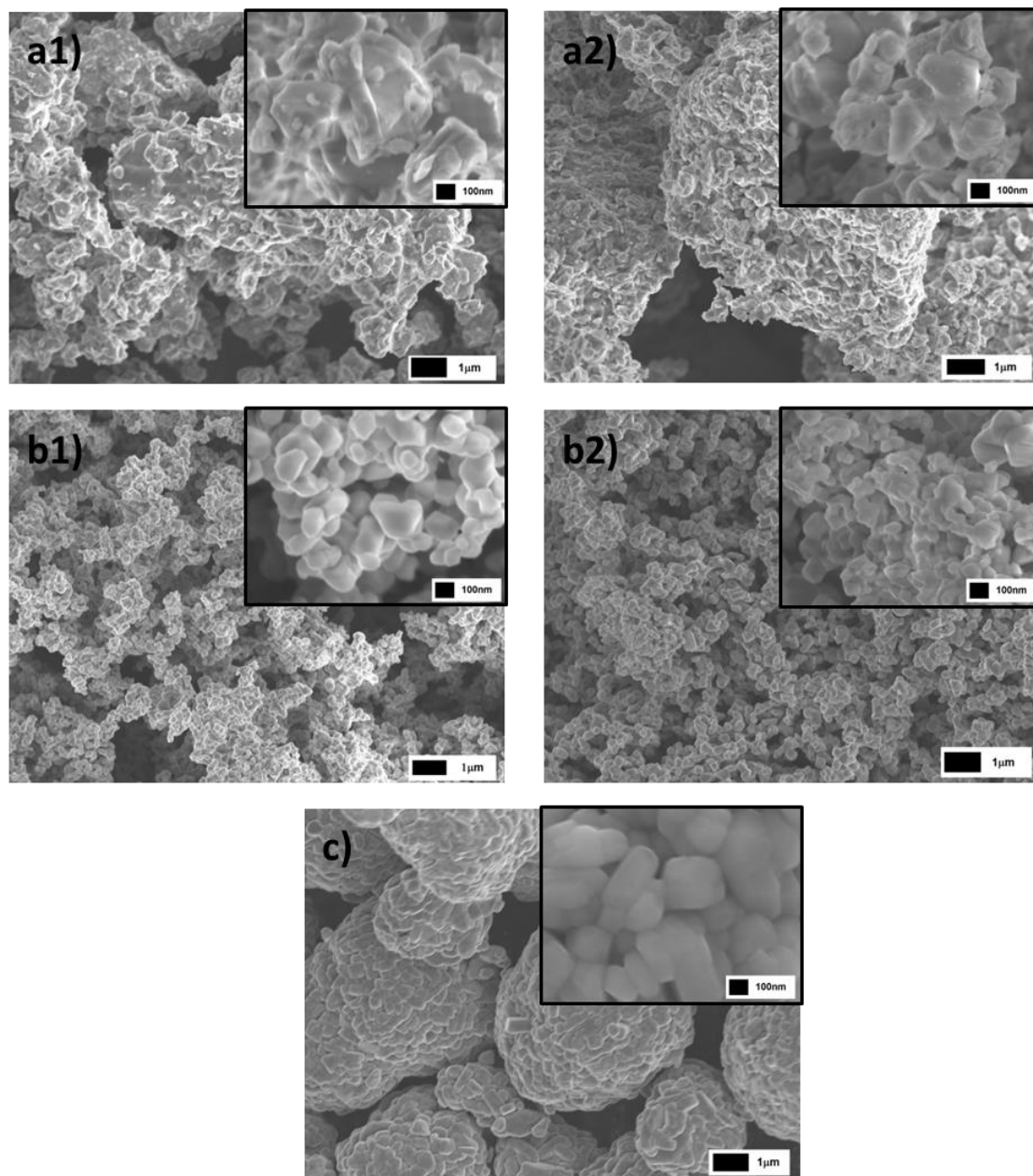


**Figure 3.2.** SEM images of the particles prepared by the different synthetic routes: a) hydroxide co-precipitation, b) sol-gel polymerisation and c) solid-state synthesis. The 1  $\mu\text{m}$  scale shows the conglomerates of the different samples and the 100 nm scale shows the individual particles.

### ***Chapter 3. Effect of the synthetic routes on the surface properties and electrochemical performance of $\text{LiNi}_{1-x-y}\text{Co}_x\text{Mn}_y\text{O}_2$***

---

According to the images, all the synthesised materials consist of individual particles, with an important difference in the size of the particles according to the followed synthetic route. The higher particle size is for the hydroxide co-precipitation synthesis, with a diameter of ~900 nm and ~560 nm for CP1 and CP2, respectively. This difference in diameter demonstrates that the control of the drop size has an important influence in the size of the particles. The conglomerates are uniform, with a size between 3 and 5  $\mu\text{m}$ .

For the sol-gel polymerisation synthesis, the particles are small in both samples, with a narrow distribution in the range of 0.1 to 0.5  $\mu\text{m}$ , fused together to form disordered agglomerates. The difference in the particle size for both samples is not significant, with a diameter of ~280 nm for SG1 and ~220 nm for SG2. For the commercial sample, the conglomerates are very uniform, with a size of approximately 5  $\mu\text{m}$  and a particle size of ~800 nm. The calculation of the particle diameter was done using the scale and observing the particles, therefore the error can be considerable.

**Table 3.3.** A comparison between the surface area and porosity of the samples using BET measurements, as well as the approximate diameter of the particles measured in SEM.

<b>Sample</b>	<b>Surface area (<math>\text{m}^2 \text{g}^{-1}</math>)</b>	<b>Pore size (nm)</b>	<b>Diameter (nm)</b>
CP1	-	-	900
CP2	$1.2 \pm 0.1$	-	560
SG1	$6.3 \pm 0.1$	3.010(3)	280
SG2	$4.0 \pm 0.1$	2.414(0)	220
COM	$0.4 \pm 0.1$	2.719(2)	800

Additional BET measurements were done in order to determine the surface and the porosity of the materials (**Table 3.3.**). For the co-precipitation samples (CP1 and CP2),

### ***Chapter 3. Effect of the synthetic routes on the surface properties and electrochemical performance of $\text{LiNi}_{1-x-y}\text{Co}_x\text{Mn}_y\text{O}_2$***

---

the isotherms were difficult to measure, making impossible to obtain reliable results in the case of CP1, and the impossibility to measure the pore size in CP2, although several measurements were done. In any case, the obtained results in BET reveal a high surface area for the polymerisation samples ( $6.3 \text{ m}^2 \text{ g}^{-1}$  for SG1 and  $4.0 \text{ m}^2 \text{ g}^{-1}$  for SG2) while the commercial sample had a surface area of  $0.4 \text{ m}^2 \text{ g}^{-1}$ . These values can be related with the particle size and the agglomerates observed in SEM, showing that a bigger diameter and bigger agglomerates gave place to a lower surface area, and vice versa.

#### **3.3.2. Electrochemical Properties**

A symmetric cycling procedure was developed whereby an initial galvanostatic charge at  $100 \text{ mA g}^{-1}$  up to  $4.6 \text{ V vs. Li/Li}^+$ . On lithiation the cell was discharged down to  $2.5 \text{ V vs. Li/Li}^+$ . The electrochemical measurements of the  $\text{LiNi}_{1/3}\text{Co}_{1/3}\text{Mn}_{1/3}\text{O}_2$  samples are compared in **Figure 3.3**.

The galvanostatic measurement showed in **Figure 3.3a**, represents the first charge / discharge cycle. The curves are very similar but an unexpected shoulder during charge is observed for both co-precipitation samples at  $\sim 4.5 \text{ V}$  that cannot be explained using the literature values in order to compare the results. In the case of the discharge, there is a clear difference of capacity between the samples according to their synthetic routes, where co-precipitation samples have the lowest capacity (especially in the case of CP1 with a discharge capacity of  $138 \text{ mAh g}^{-1}$ , while CP2 has a discharge capacity of  $168 \text{ mAh g}^{-1}$ ). On the other hand, sol-gel polymerisation samples have the best capacity, with a discharge capacity of  $195 \text{ mAh g}^{-1}$  in the case of SG1 and  $198 \text{ mAh g}^{-1}$  for SG2. For the commercial sample, the discharge capacity is  $175 \text{ mAh g}^{-1}$ , which is between both synthetic methods.

**Chapter 3. Effect of the synthetic routes on the surface properties and electrochemical performance of  $\text{LiNi}_{1-x-y}\text{Co}_x\text{Mn}_y\text{O}_2$**

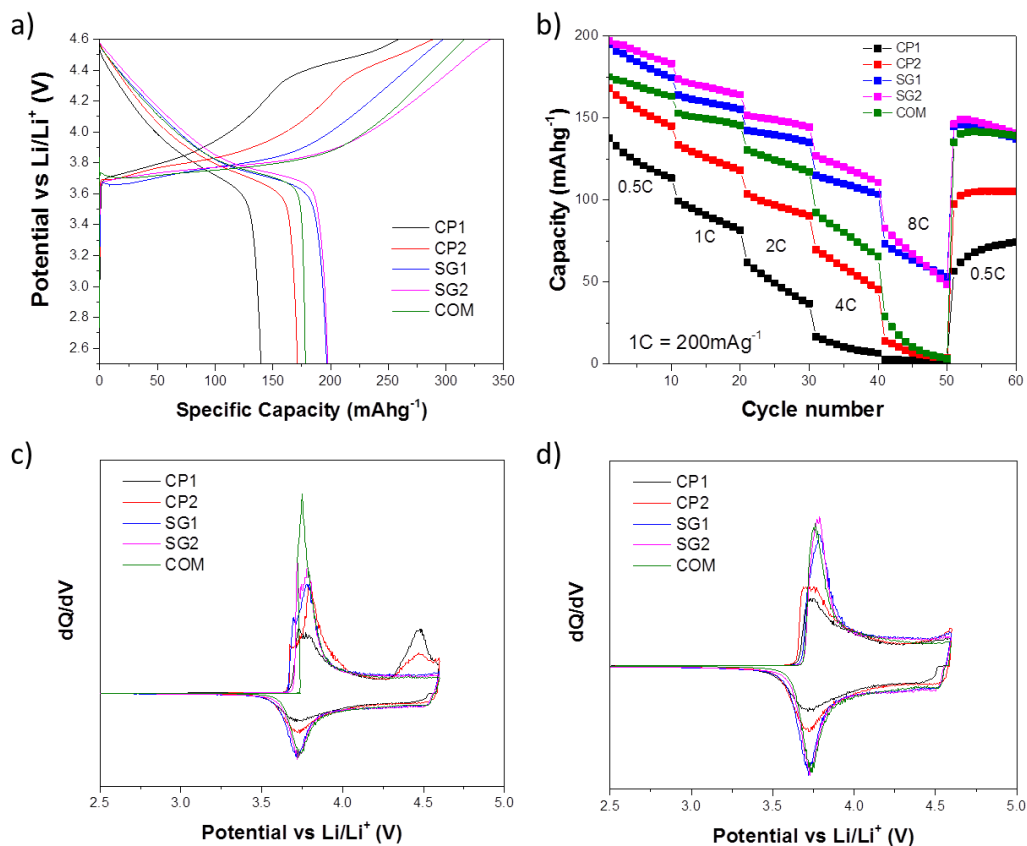


**Figure 3.3.** Comparison of the electrochemical performance of the studied materials. (a) Galvanostatic measurement during first cycle and (b) cyclability at different C-rates, as well as the differential capacity at first (c) and second cycle (d).

The extended cyclability measurements of the samples are shown in **Figure 3.3b.**, with a total measurement of 60 cycles and a variation of C-rate every 10 cycles (100, 200, 400, 800, 1600 and 100 mA g<sup>-1</sup>). Cyclability shows a decrease in the capacity with the increase of C-rate, with values approaching 0 mAh g<sup>-1</sup> for both co-precipitation and the commercial sample at 1600 mA g<sup>-1</sup>. For sol-gel samples, the capacity does not fall as dramatically as the other samples. SG1 has low capacity with the increase of C-rate compared with SG2 (around 10 mAh g<sup>-1</sup> below) but SG2 looks to be less stable when it

### ***Chapter 3. Effect of the synthetic routes on the surface properties and electrochemical performance of $\text{LiNi}_{1-x-y}\text{Co}_x\text{Mn}_y\text{O}_2$***

---

is cycled at high C-rate reaching values in the 50<sup>th</sup> cycle to 53 and 50 mAh g<sup>-1</sup>, respectively. After 60 cycles, both the sol-gel and the commercial samples have very similar capacities, with final values of around 140 mAh g<sup>-1</sup>. For the co-precipitation samples the final capacities are still poor, with 74 mAh g<sup>-1</sup> in the case of CP1 and 105 mAh g<sup>-1</sup> for CP2.

According to previous research, the expected oxidation states of nickel, cobalt and manganese in  $\text{LiNi}_{1/3}\text{Co}_{1/3}\text{Mn}_{1/3}\text{O}_2$  are +2, +3, and +4, respectively.<sup>14, 15, 28, 33, 34</sup> It is believed that the  $\text{Mn}^{4+}$  remains the same in this voltage range and it is not active (according to the XANES measurements of Mn K-edge, where the variation of XANES spectra is due to the change in environments around the Mn rather than a change in the oxidation state because the distance of Mn-O bond remains unchanged during cycling).<sup>35</sup>

The differential capacity for first and second cycle shows a strong peak at ~3.7 V corresponding to the redox transitions that are taking place, involving both  $\text{Co}^{3+/4+}$  and  $\text{Ni}^{2+/4+}$  – via the two-step process from  $\text{Ni}^{2+/3+}$  to  $\text{Ni}^{3+/4+}$  according to some theories.<sup>14, 24,</sup><sup>36</sup> **Figure 3.3c.** shows that CP1 has low intensity in the redox charge peak compared with the other samples, and the commercial sample has the strongest one; surprisingly, sol-gel samples have medium intensity in spite of their highest capacity, and CP2 has a similar intensity even though the capacity is lower. Additionally, in this first cycle it is observed that co-precipitation samples also have a secondary transition peak during charge at ~4.5 V. In **Figure 3.3d.**, there is a change in the observed redox behaviour, where now both the commercial and sol-gel samples have a very similar intensity while co-precipitation samples still have the lowest one; additionally, the observed secondary peak in the co-precipitation samples has disappeared.

At this point, it looks like there is no relationship between the obtained capacity and the intensity of the redox transitions, as well as those secondary peaks that appeared in some samples. To understand what is happening, it is necessary to study the morphology and surface behaviour of these materials.

### **3.3.3. Strength of M-O vibration bonds**

Raman measurements took place in a region between 100 and 3500  $\text{cm}^{-1}$ , showing only peaks in a region between 400 and 800  $\text{cm}^{-1}$  corresponding to the M-O vibration modes. The comparison of the different spectra appears in **Figure 3.4**.

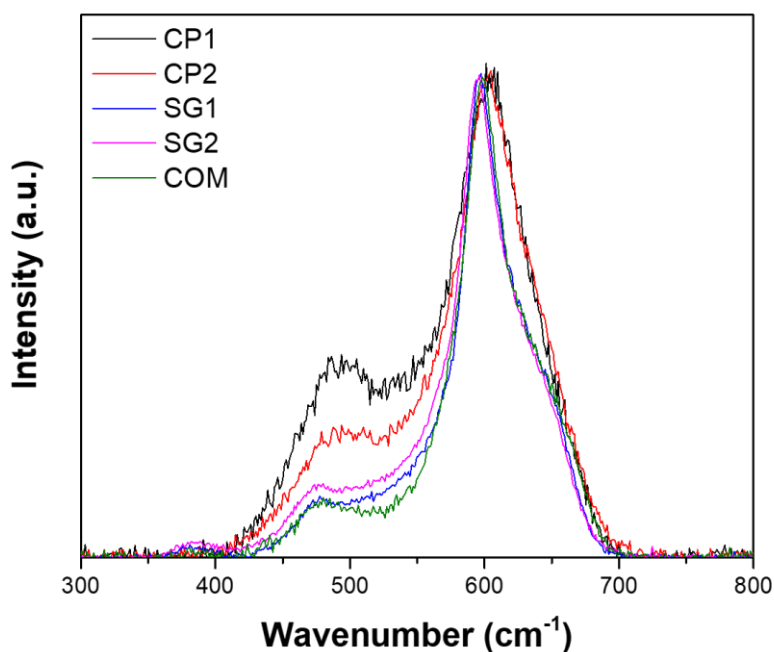


**Figure 3.4.** Raman spectra of the different measured samples where the vibration bonds are represented (spectra were normalised to the prominent band at  $\sim 597 \text{ cm}^{-1}$ ). The difference in shape is directly related with M-O vibration modes for each studied material.

### ***Chapter 3. Effect of the synthetic routes on the surface properties and electrochemical performance of $\text{LiNi}_{1-x-y}\text{Co}_x\text{Mn}_y\text{O}_2$***

---

No peaks were detected in the region between 3000 and 3500  $\text{cm}^{-1}$ , discarding any possible formation of metal hydroxides. No prominent carbonate or carboxyl-like bands were detected. The deconvolution of the bands shows the characteristic vibration bonds for this material:  $\nu_{\text{Mn-O}}$  ( $\sim 381 \text{ cm}^{-1}$ ),  $\nu_{\text{O-Mn-O}}$  ( $\sim 478 \text{ cm}^{-1}$ ),  $\nu_{\text{O-Ni-O}}$  ( $\sim 520 \text{ cm}^{-1}$ ),  $\nu_{\text{Ni-O}}$  ( $\sim 565 \text{ cm}^{-1}$ ),  $\nu_{\text{Co-O}}$  ( $\sim 597 \text{ cm}^{-1}$ ) and  $\nu_{\text{Mn-O}}$  ( $\sim 624 \text{ cm}^{-1}$ ), and two bands assigned to  $E_g$  and  $A_{1g}$  which appear at  $\sim 500 \text{ cm}^{-1}$  and  $\sim 600 \text{ cm}^{-1}$ , respectively, according to what was already described in **Figure 2.13.** from *Chapter 2* and the bibliography.<sup>37-39</sup> The measured positions of these bands are in good agreement with the expected values for species related to  $\text{Ni}^{2+}$ ,  $\text{Mn}^{4+}$  and  $\text{Co}^{3+}$ .<sup>40, 41</sup>

The normalisation of each spectrum allows observing a variation of the  $\nu_{\text{O-Mn-O}}$  and  $\nu_{\text{O-Ni-O}}$  vibration modes and their intensities are not related with the stoichiometry of each sample as observed in ICP-OES measurements in **Table 3.1.** A clear example is the  $\nu_{\text{O-Mn-O}}$  vibration bond, where CP1 has the strongest signal while SG1 has the smallest. In the case of  $\nu_{\text{Mn-O}}$  vibration bond at  $\sim 624 \text{ cm}^{-1}$ , the  $\nu_{\text{Co-O}}$  and  $\nu_{\text{Mn-O}}$  vibration bonds for the co-precipitation samples overlapped each other, giving place to a broad peak. Both sol-gel and the commercial sample show a clearer difference in shape for both vibration bonds, showing a sharp peak from  $\nu_{\text{Co-O}}$  bond and a shoulder at  $\sim 640 \text{ cm}^{-1}$  from  $\nu_{\text{Mn-O}}$  bond.

#### **3.3.4. Surface behaviour and its relationship with the synthetic method**

Surface behaviour of the different samples was analysed using X-ray photoelectron spectroscopy. In **Figure 3.5.**, a comparison between the survey scans of the different pristine powders were studied using Mg  $K\alpha$  as X-ray source. In all of them, it is possible to observe the core electrons from Ni  $2p_{3/2}$  ( $854.7 \pm 0.5 \text{ eV}$ ), Co  $2p_{3/2}$  ( $780.0 \pm 0.2 \text{ eV}$ ),

### ***Chapter 3. Effect of the synthetic routes on the surface properties and electrochemical performance of $\text{LiNi}_{1-x-y}\text{Co}_x\text{Mn}_y\text{O}_2$***

Mn  $2p_{3/2}$  ( $642.0 \pm 0.5$  eV), O 1s ( $529.9 \pm 0.7$  eV) and Li 1s ( $54.9 \pm 0.5$  eV), according to their comparison with the NIST X-ray Photoelectron Spectroscopy Database.<sup>42</sup> There is also an additional C 1s peak due to the adventitious carbon<sup>43, 44</sup> and the characteristic Auger peaks for each element.<sup>45</sup>

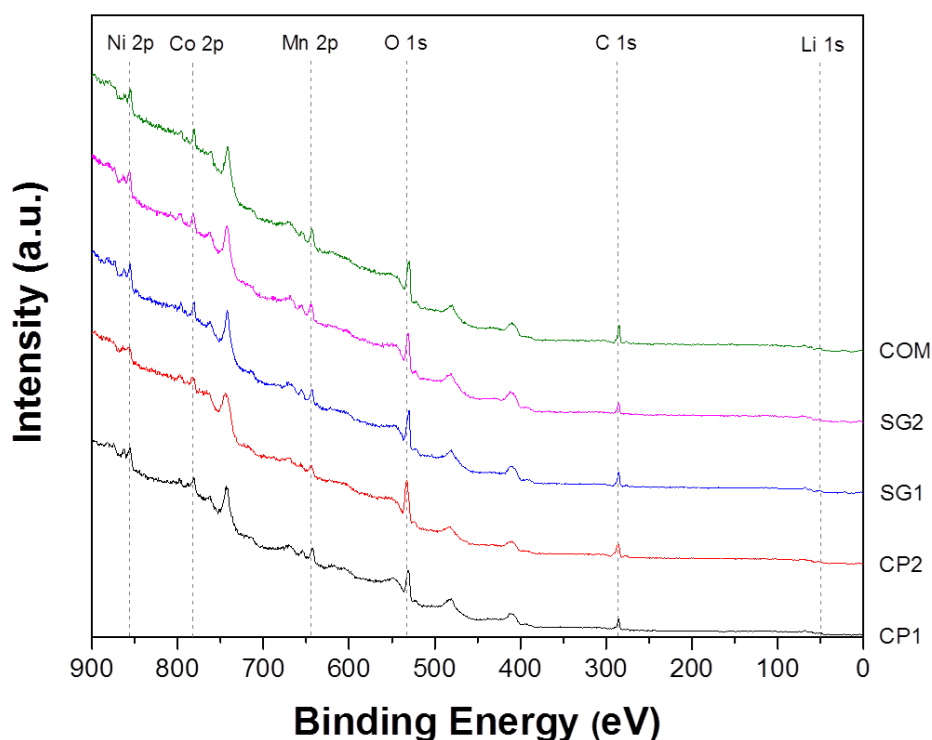


**Figure 3.5.** Survey scan of the different samples in XPS. The profile for all of them was the same, which means that the expected core-level peaks are observed, as well as their respective Auger peaks.

A deep analysis of the different regions shows that Li 1s is overlapped with Mn 3p. A more detailed study of the core-level peaks of interest is represented in **Figure 3.6**. Charge correction was done using O 1s, implementing the strongest component after deconvolution at 529.5 eV, which is where the expected ( $\text{Mn}^{4+}$ )-O bond appears.



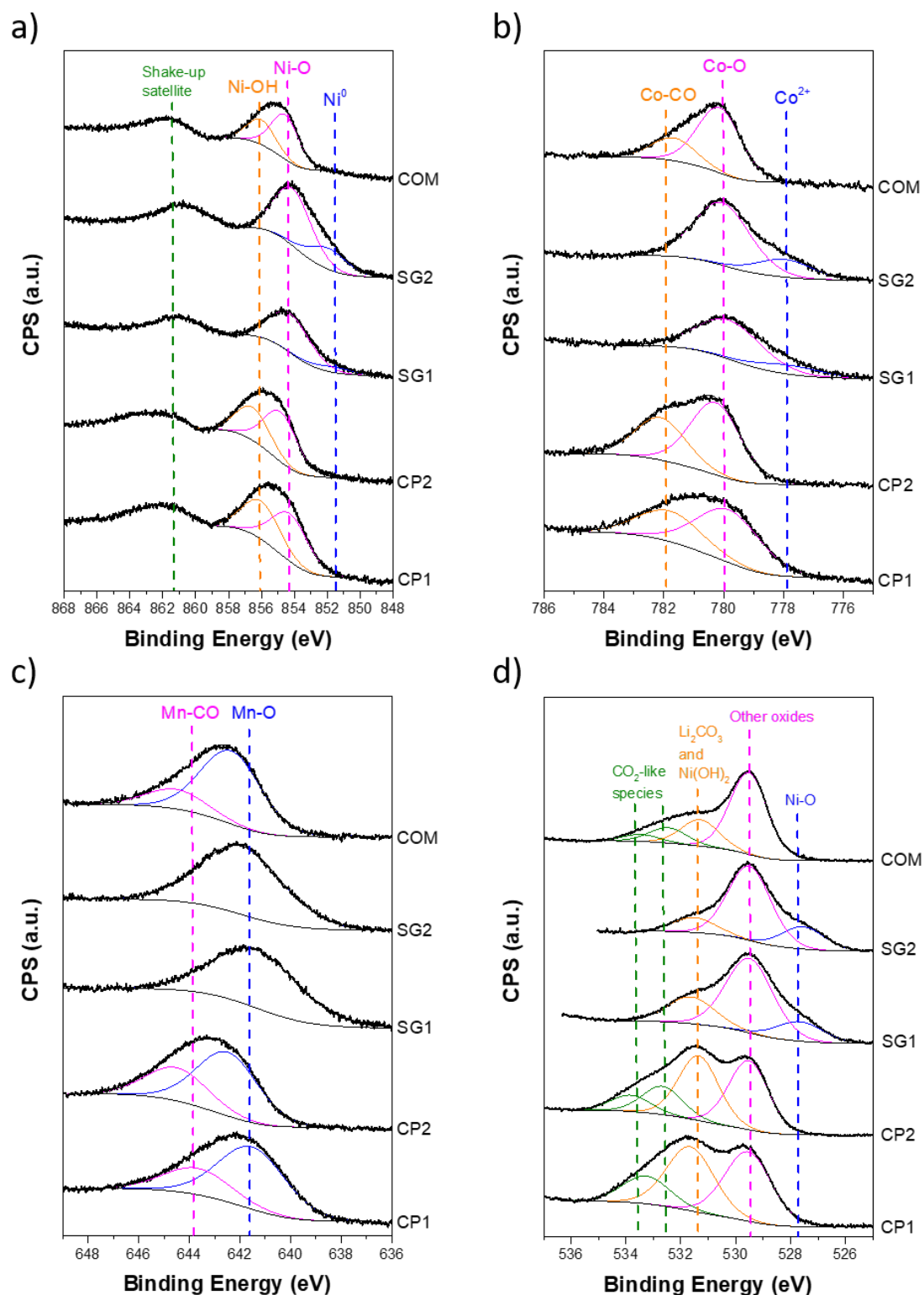


**Figure 3.6.** Comparison of XPS spectrum from the different samples where their core-level peaks are shown: a) Ni 2p<sub>3/2</sub>, b) Co 2p<sub>3/2</sub>, c) Mn 2p<sub>3/2</sub> and d) O 1s.

***Chapter 3. Effect of the synthetic routes on the surface properties and electrochemical performance of  $\text{LiNi}_{1-x-y}\text{Co}_x\text{Mn}_y\text{O}_2$***

According to the data plotted, it is observed a different result for Ni 2p, Co 2p, Mn 2p and O 1s in each sample. The deconvolution shows different contributions related with different oxidation states and different oxo-species in the transition metals. The percentage of these contributions is showed in **Table 3.4**.

**Table 3.4.** Percentage of contribution from the different species of Ni, Co and Mn observed in XPS for the different studied samples (standard deviation of  $\pm 0.5\%$ ).

Type	CP1	CP2	SG1	SG2	COM
Ni <sup>0</sup> -O	-	-	11.5%	26.9%	-
Ni <sup>2+</sup> -O	55.4%	60.1%	88.5%	73.1%	64.2%
Ni <sup>2+</sup> -OH	44.6%	39.9%	-	-	35.8%
Co <sup>2+</sup> -O	-	-	18.9%	22.1%	-
Co <sup>3+</sup> -O	63.2%	63%	81.1%	77.9%	74.1%
Co <sup>3+</sup> -CO	36.8%	37%	-	-	25.9%
Mn <sup>4+</sup> -O	70.1%	65.2%	100%	100%	78.7%
Mn <sup>4+</sup> -CO	29.9%	34.8%	-	-	21.3%

Focusing on Ni 2p<sub>3/2</sub>, it is surprising that in the sol-gel samples appears what was considered being a small contribution of metallic Ni at low  $E_B$ ; although in  $\text{LiNi}_{1/3}\text{Mn}_{1/3}\text{Co}_{1/3}\text{O}_2$  is expected to have only Ni<sup>2+</sup>. In the case of both the co-precipitation and commercial samples, a contribution appears at ~856 eV attributed to the formation of Ni(OH)<sub>2</sub> in the surface of the samples.

For Co 2p<sub>3/2</sub>, the sol-gel compounds have small contributions of Co<sup>2+</sup>, while in the other samples, there is a formation of what is considered to be Co<sub>2</sub>(CO<sub>3</sub>)<sub>3</sub> at ~782 eV. For Mn 2p<sub>3/2</sub>, sol-gel samples have pure Mn-O bonds, while the rest of the samples have an

### ***Chapter 3. Effect of the synthetic routes on the surface properties and electrochemical performance of $\text{LiNi}_{1-x-y}\text{Co}_x\text{Mn}_y\text{O}_2$***

---

important contribution at high  $E_B$  (~644 eV) assigned to be  $\text{Mn}(\text{CO}_3)_2$ . These contributions in the transition metals lead to a shift in peak position to higher  $E_B$  in the case of both the co-precipitation and commercial samples.

The oxidation state for each transition metal was calculated using the percentage of each contribution as shown in **Table 3.4.**, and was established that both sol-gel samples have an oxidation state for both Ni and Co of +1.8 and +2.8, respectively. In the rest of samples, the oxidation states are the expected  $\text{Ni}^{2+}$  and  $\text{Co}^{3+}$ . It was established that Mn was in the Mn(IV) oxidation state in all cases.

The O 1s peaks showed in **Figure 3.6d.** show that the overall peak shape varies accordingly to the synthetic method, with a clear difference between the co-precipitation, sol-gel and commercial samples. Sol-gel samples have a small shoulder at low  $E_B$  attributed to Ni-O bond (~527.6 eV), and another one at high  $E_B$  (~531.5 eV) that was mainly attributed to the formation of some  $\text{Li}_2\text{CO}_3$  in the surface of this material after reaction of  $\text{Li}^+$  ions with  $\text{CO}_2$ -like species from the atmosphere. For the rest of the samples, the shoulder at low  $E_B$  disappears and the contribution at ~531.5 eV is more important, which can be related with the formation of  $\text{Ni}(\text{OH})_2$  as observed in Ni 2p. Both  $\text{Ni}(\text{OH})_2$  and  $\text{Li}_2\text{CO}_3$  appears at same  $E_B$ , giving place to a strong peak which is the combination of both components. It also appears to be an adsorption onto the surface of other carbon-based species at high  $E_B$  (that can be attributed to the formation of both cobalt and manganese carbonates) and such adsorbed species does not appear in the analysis of the sol-gel samples.

In order to understand what is the observed redox peak at ~4.5 V during first charge in the co-precipitation samples (**Figure 3.3c.**), some electrodes for the co-precipitation and the sol-gel samples were measured in XPS and oxidation states for the pristine

### ***Chapter 3. Effect of the synthetic routes on the surface properties and electrochemical performance of $\text{LiNi}_{1-x-y}\text{Co}_x\text{Mn}_y\text{O}_2$***

electrode (uncharged) and electrodes charged at 4.35 V and 4.6 V (first charge) were obtained. The data is compared within **Table 3.5**. The initial  $E_B$  for the pristine electrodes are ~854.6 eV for Ni 2p<sub>3/2</sub>, ~780.1 eV for Co 2p<sub>3/2</sub> and ~642.4 eV for Mn 2p<sub>3/2</sub>. After charging at 4.35 V, a shift at high  $E_B$  for Ni (~855.6 eV) is observed, while both Co and Mn positions remain unchanged. Finally, in the electrode charged at 4.6 V the shift at high  $E_B$  is coming from Co (~780.6 eV), while Ni has a final  $E_B$  of ~855.6 eV and Mn still remains at ~642.4 eV.

**Table 3.5.** Comparison of the pristine electrode and electrodes charged at 4.35 V and 4.6 V for the co-precipitation and sol-gel polymerisation samples. Oxidation states were measured using shift in the  $E_B$  of the core-level peak (error of  $\pm 0.3$  eV).

Sample	Pristine	4.35 V	4.6 V
CP	Ni <sup>2+</sup> , Co <sup>3+</sup> , Mn <sup>4+</sup>	Ni <sup>3+</sup> , Co <sup>3+</sup> , Mn <sup>4+</sup>	Ni <sup>3+</sup> , Co <sup>3.7+</sup> , Mn <sup>4+</sup>
SG	Ni <sup>2+</sup> , Co <sup>2.9+</sup> , Mn <sup>4+</sup>	Ni <sup>3+</sup> , Co <sup>3+</sup> , Mn <sup>4+</sup>	Ni <sup>3.2+</sup> , Co <sup>3.6+</sup> , Mn <sup>4+</sup>

These results confirm that the redox transitions are according to the expected, although the redox peak at ~3.75 V attributed is Ni<sup>2+/3+</sup> and does not reach the Ni(IV) oxidation state as was expected according to previous measurements.<sup>14, 24</sup> The peak at ~4.5 V shows the expected Co<sup>3+/4+</sup> redox transition according to some theories.<sup>46</sup>

### **3.4. Discussion**

Elemental analysis using ICP-OES shows a stoichiometry for each sample similar to the theoretical one. PXRD measurements show a very well-defined crystal layered structure, with space group  $R\bar{3}m$  for all the studied compounds.

### ***Chapter 3. Effect of the synthetic routes on the surface properties and electrochemical performance of $\text{LiNi}_{1-x-y}\text{Co}_x\text{Mn}_y\text{O}_2$***

---

The study of the morphology using SEM shows important differences depending of the used synthetic method. Focussing only on the co-precipitation samples, there is a clear difference in the particle size between CP1 and CP2 as it is shown in **Figure 3.2**. This is clear evidence of the importance of drop size with the addition of a small pipette at the bottom of the burette in the case of CP2: small drops give place to small particles (~560 nm compared with the ~900 nm obtained for CP1). These results demonstrate a clear relationship between drop size and particle size, as well as an important relationship with the surface area (**Table 3.2.**). For the sol-gel samples, there is no clear difference between SG1 and SG2, showing nanoparticles of 200-300 nm, meaning that a second calcination has no influence in the control of the particle size; in both cases, the agglomerates have a narrow distribution – strongly influenced for the formed gel during polymerisation process. Finally, the commercial sample has similar diameter than CP1, but the agglomerates are slightly different with more spherical results.

The surface behaviour observed in XPS can help to understand the capacities obtained and the profile of differential capacity plots. Mn is redox inactive for  $\text{LiNi}_{1/3}\text{Co}_{1/3}\text{Mn}_{1/3}\text{O}_2$  compounds, but it has been shown to increase the stability of the metal oxide lattice,<sup>28, 35</sup> which means that the higher the oxidation state of Mn, the greater the stability of the metal oxide lattice during deintercalation / reintercalation process, and therefore the greater the capacity.<sup>47</sup> In all the samples, the oxidation state observed for Mn is +4, and for Ni and Co the oxidation states are established as +2 and +3, respectively. In **Figure 3.3c.**, the differential capacity shows a redox peak at ~3.75 V, which can be attributed to  $\text{Ni}^{2+/4+}$  according to previous results<sup>14, 24</sup>. However, measurements of the electrodes at different stages of charge (**Table 3.5.**) show that only  $\text{Ni}^{2+/3+}$  transition is taking place even for the sol-gel samples. One reason could be that the measurements are

### ***Chapter 3. Effect of the synthetic routes on the surface properties and electrochemical performance of $\text{LiNi}_{1-x-y}\text{Co}_x\text{Mn}_y\text{O}_2$***

---

done in XPS, which is a surface sensitive technique, therefore future measurements have to be undergone in the bulk of the materials to confirm that Ni behaves in a same way.

$\text{Co}^{3+/4+}$  redox transition is taking place at  $\sim 4.5$  V,<sup>46</sup> showing a strong peak for the co-precipitation samples and it is not appreciated for the rest of the samples. The reason why this peak appears is not clear and has to be further investigated in future measurements.

**Figure 3.6.** shows that both the co-precipitation and the commercial samples turned out to be sensitive to the atmosphere leading to the formation of surface compounds with adsorbed species. Li, Co and Mn reacted to form carbonates, whereas Ni formed hydroxides with the moisture. In the Ni 2p spectra, the small contribution at low  $E_B$  in the sol-gel samples was considered metallic Ni due to the low stability of  $\text{Ni}^+$  but this explanation has to be confirmed with other methods such as XANES, that is also very useful in order to measure the oxidation state of the elements in a studied sample. The formation of a carbonate and hydroxide layers on the surface of these samples led to lower capacity and lower rate capability due to the increase in impedance from the presence of these layers. Less cyclable  $\text{Li}^+$  was available during deintercalation / reintercalation process, and Ni and Co are less redox active due to the passivation layer that is being formed (additionally,  $\text{Li}_2\text{CO}_3$  can facilitate the formation of a thicker CEI with the electrolyte).<sup>8, 48, 49</sup>

Raman measurements in **Figure 3.4.** shows after normalisation that the formed M-O vibration bonds have important variations in intensity between each sample. An additional weak band at  $\sim 1080$   $\text{cm}^{-1}$  for the co-precipitation samples attributed to  $\text{Li}_2\text{CO}_3$  was present in the Raman spectrum;<sup>50</sup> these measurements were undergone several months after the initial synthesis, which can suggests that the formation of  $\text{Li}_2\text{CO}_3$  in the co-precipitation samples can affect not also the surface but also the bulk after a time.

### ***Chapter 3. Effect of the synthetic routes on the surface properties and electrochemical performance of $\text{LiNi}_{1-x-y}\text{Co}_x\text{Mn}_y\text{O}_2$***

---

The fact that carbonates or hydroxides do not appear in the measured XPS spectra for the sol-gel samples indicate a higher surface stability in the use of this synthetic method (it is possible to discard any Ni-OH species according to the shoulder observed at ~527.6 eV which correspond at Ni-O species). This is maybe due to the narrow distribution of the agglomerates and the bigger surface area for these samples (**Table 3.3.**), producing particles that are more difficult to passivate and therefore  $\text{Li}^+$  ions can move easily – as reported previously using electrochemical impedance spectroscopy (EIS)<sup>51</sup> for the study of charge transfer resistance in  $\text{LiNi}_{1/3}\text{Co}_{1/3}\text{Mn}_{1/3}\text{O}_2$  samples.<sup>52-54</sup>

### **3.5. Conclusions**

Four samples prepared via two different synthetic routes were investigated and compared with a commercial sample. X-ray diffraction shows layer-structured materials with good hexagonal ordering, and Raman spectroscopy shows the vibration bonds between oxygen and the metals from the bulk of the different samples, confirming with these techniques that the crystal structure and the bonds formed are according to the expected results.

The SEM images show that there is an important difference in the particle size depending on which synthetic method is studied, and the importance of the modification in the synthesis conditions to obtain different sizes (as observed in the drop size for CP1 and CP2). The particle size is directly related with the electrochemical measurements for each sample. In the comparison between the two samples synthesised via hydroxide co-precipitation method, the sample with small nanoparticles (CP2) has a better capacity than the samples with big nanoparticles (CP1), giving place to a first discharge capacity of 138 mAh  $\text{g}^{-1}$  for CP1 while CP2 has a discharge capacity of 168 mAh  $\text{g}^{-1}$  as observed in

### ***Chapter 3. Effect of the synthetic routes on the surface properties and electrochemical performance of $\text{LiNi}_{1-x-y}\text{Co}_x\text{Mn}_y\text{O}_2$***

---

**Figure 3.3.** The fact that CP2 has a better surface area than CP1 (**Table 3.3.**) leads to a better accessibility of the deintercalation / reintercalation process for  $\text{Li}^+$  ions, further supporting the already well-established fact of the direct relationship between the particle size and the electrochemical performance. The small particle size and narrow distribution for sol-gel polymerisation samples give place to the best electrochemical performance of all samples, with capacities reaching  $200 \text{ mAh g}^{-1}$  in the first discharge, and good cyclability and stability at high C-rates.

Surface studies with XPS were important in order to link the electrochemical behaviour of these samples with the surface reactivity with the adsorbed species from air, like moisture and carbon-based compounds. This surface reactivity is very important in the co-precipitation and the commercial samples, forming metal carbonates and hydroxides as observed in **Figure 3.6.** The formation of a passivation layer is therefore possible and further studies using electrochemical impedance spectroscopy should be done in order to observe this layer in each sample. The additional study of electrodes at different charge states using *ex situ* XPS helps to better understand the link between the redox transitions observed in the differential capacity plots and the surface reactivity and final oxidation states for each sample.



***Chapter 3. Effect of the synthetic routes on the surface properties and electrochemical performance of  $\text{LiNi}_{1-x-y}\text{Co}_x\text{Mn}_y\text{O}_2$***

---

### **3.6. References**

1. E. Rossen, C. Jones and J. Dahn, *Solid State Ionics*, 1992, **57**, 311-318.
2. M. S. Islam, R. A. Davies and J. D. Gale, *Chem. Mater.*, 2003, **15**, 4280-4286.
3. T. Ohzuku and Y. Makimura, *Chem. Lett.*, 2001, 642-643.
4. T. Cho, S. Park, M. Yoshio, T. Hirai and Y. Hideshima, *J. Power Sources*, 2005, **142**, 306-312.
5. D.-C. Li, T. Muta, L.-Q. Zhang, M. Yoshio and H. Noguchi, *J. Power Sources*, 2004, **132**, 150-155.
6. C. Deng, L. Liu, W. Zhou, K. Sun and D. Sun, *Electrochim. Acta*, 2008, **53**, 2441-2447.
7. O. Haik, N. Leifer, Z. Samuk-Fromovich, E. Zinigrad, B. Markovsky, L. Larush, Y. Goffer, G. Goobes and D. Aurbach, *J. Electrochem. Soc.*, 2010, **157**, A1099-A1107.
8. K. Edström, T. Gustafsson and J. O. Thomas, *Electrochim. Acta*, 2004, **50**, 397-403.
9. G. Cherkashinin, K. Nikolowski, H. Ehrenberg, S. Jacke, L. Dimesso and W. Jaegermann, *Phys. Chem. Chem. Phys.*, 2012, **14**, 12321-12331.
10. L. Dahéron, H. Martinez, R. Dedryvère, I. Baraille, M. Ménétrier, C. Denage, C. Delmas and D. Gonbeau, *J. Phys. Chem. C*, 2009, **113**, 5843-5852.
11. F. Gamble, J. Osiecki, M. Cais, R. Pisharody, F. DiSalvo and T. Geballe, *Science*, 1971, **174**, 493-497.
12. Z. Lu, D. MacNeil and J. Dahn, *Electrochem. Solid-State Lett.*, 2001, **4**, A191-A194.

***Chapter 3. Effect of the synthetic routes on the surface properties and electrochemical performance of  $\text{LiNi}_{1-x-y}\text{Co}_x\text{Mn}_y\text{O}_2$***

---

13. S.-W. Lee, D.-H. Jang, J.-B. Yoon, Y.-H. Cho, Y.-S. Lee, D.-H. Kim, W.-S. Kim and W.-S. Yoon, *J. Electrochem. Sci. Technol.*, 2012, **3**, 29-34.
14. Y. Koyama, N. Yabuuchi, I. Tanaka, H. Adachi and T. Ohzuku, *J. Electrochem. Soc.*, 2004, **151**, A1545-A1551.
15. N. Yabuuchi, Y. Koyama, N. Nakayama and T. Ohzuku, *J. Electrochem. Soc.*, 2005, **152**, A1434-A1440.
16. J. Choi and A. Manthiram, *Electrochem. Solid-State Lett.*, 2004, **7**, A365-A368.
17. S. Patoux and M. M. Doeff, *Electrochem. Commun.*, 2004, **6**, 767-772.
18. Z. Wang, Y. Sun, L. Chen and X. Huang, *J. Electrochem. Soc.*, 2004, **151**, A914-A921.
19. Z. Lu, D. MacNeil and J. Dahn, *Electrochem. Solid-State Lett.*, 2001, **4**, A200-A203.
20. D. MacNeil, Z. Lu and J. R. Dahn, *J. Electrochem. Soc.*, 2002, **149**, A1332-A1336.
21. N. Yabuuchi and T. Ohzuku, *J. Power Sources*, 2003, **119**, 171-174.
22. S. A. Al-Muhtaseb and J. A. Ritter, *Adv. Mater.*, 2003, **15**, 101-114.
23. K. M. Shaju and P. G. Bruce, *Adv. Mater.*, 2006, **18**, 2330-2334.
24. K. Shaju, G. S. Rao and B. Chowdari, *Electrochim. Acta*, 2002, **48**, 145-151.
25. K. Shaju, G. S. Rao and B. Chowdari, *J. Electrochem. Soc.*, 2004, **151**, A1324-A1332.
26. A. M. Hashem, A. E. Abdel-Ghany, H. M. Abuzeid, H. Ehrenberg, A. Mauger, H. Groult and C. M. Julien, *ECS Trans.*, 2013, **50**, 91-96.
27. S. C. Yin, Y. H. Rho, I. Swainson and L. F. Nazar, *Chem. Mater.*, 2006, **18**, 1901-1910.

***Chapter 3. Effect of the synthetic routes on the surface properties and electrochemical performance of  $\text{LiNi}_{1-x-y}\text{Co}_x\text{Mn}_y\text{O}_2$***

---

28. B. Hwang, Y. Tsai, D. Carlier and G. Ceder, *Chem. Mater.*, 2003, **15**, 3676-3682.
29. N. N. Sinha and N. Munichandraiah, *ACS Appl. Mater. Interfaces*, 2009, **1**, 1241-1249.
30. S.-C. Yin, Y.-H. Rho, I. Swainson and L. Nazar, *Chem. Mater.*, 2006, **18**, 1901-1910.
31. M. Inaba, Y. Iriyama, Z. Ogumi, Y. Todzuka and A. Tasaka, *J. Raman Spectrosc.*, 1997, **28**, 613-617.
32. S. K. Martha, H. Sclar, Z. S. Framowitz, D. Kovacheva, N. Saliyski, Y. Gofer, P. Sharon, E. Golik, B. Markovsky and D. Aurbach, *J. Power Sources*, 2009, **189**, 248-255.
33. Y. Koyama, I. Tanaka, H. Adachi, Y. Makimura and T. Ohzuku, *J. Power Sources*, 2003, **119**, 644-648.
34. Y. Tsai, B. Hwang, G. Ceder, H. Sheu, D. Liu and J. Lee, *Chem. Mater.*, 2005, **17**, 3191-3199.
35. J.-M. Kim and H.-T. Chung, *Electrochim. Acta*, 2004, **49**, 3573-3580.
36. Y.-J. Shin, W.-J. Choi, Y.-S. Hong, S. Yoon, K. S. Ryu and S. H. Chang, *Solid State Ionics*, 2006, **177**, 515-521.
37. X. Zhang, A. Mauger, Q. Lu, H. Groult, L. Perrigaud, F. Gendron and C. M. Julien, *Electrochim. Acta*, 2010, **55**, 6440-6449.
38. C. Julien and M. Massot, *Mater. Sci. Eng. B*, 2003, **97**, 217-230.
39. K. Ben-Kamel, N. Amdouni, A. Mauger and C. Julien, *J. Alloys Compd.*, 2012, **528**, 91-98.
40. D. A. Long, *J. Raman Spectrosc.*, 2004, **35**, 905-905.

***Chapter 3. Effect of the synthetic routes on the surface properties and electrochemical performance of  $\text{LiNi}_{1-x-y}\text{Co}_x\text{Mn}_y\text{O}_2$***

---

41. H. Koga, L. Croguennec, P. Mannesiez, M. Ménétrier, F. Weill, L. Bourgeois, M. Duttine, E. Suard and C. Delmas, *J. Phys. Chem. C*, 2012, **116**, 13497-13506.
42. C. D. Wagner, *The NIST X-ray photoelectron spectroscopy (XPS) database*, 1991.
43. C. D. Wagner, *J. Electron. Spectrosc. Relat. Phenom.*, 1980, **18**, 345-349.
44. T. L. Barr and S. Seal, *J. Vac. Sci. Technol. A*, 1995, **13**, 1239-1246.
45. J. F. Watts, *Surface science techniques*, 1994, 5-23.
46. A. M. Hashem, R. S. El-Tawil, M. Abutabl and A. E. Eid, *Res. Eng. Struct. Mat.*, 2015, **1**, 81-97.
47. Y. Wang, J. Roller and R. Maric, *ACS Omega*, 2018, **3**, 3966-3973.
48. P. Verma, P. Maire and P. Novák, *Electrochim. Acta*, 2010, **55**, 6332-6341.
49. V. A. Agubra and J. W. Fergus, *J. Power Sources*, 2014, **268**, 153-162.
50. M. H. Brooker and J. B. Bates, *J. Chem. Phys.*, 1971, **54**, 4788-4796.
51. C. Chen, J. Liu and K. Amine, *J. Power Sources*, 2001, **96**, 321-328.
52. Y. Wang, H. Zhang, W. Chen, Z. Ma and Z. Li, *RSC Adv.*, 2014, **4**, 37148.
53. X. Li, Y. J. Wei, H. Ehrenberg, F. Du, C. Z. Wang and G. Chen, *Solid State Ionics*, 2008, **178**, 1969-1974.
54. D. Aurbach, M. D. Levi, E. Levi, H. Teller, B. Markovsky, G. Salitra, U. Heider and L. Heider, *J. Electrochem. Soc.*, 1998, **145**, 3024-3034.

# Chapter 4.

## Electrochemical and surface behaviour for Li-rich row 1 transition metal oxides

*"What we do in life echoes in eternity."*

Maximus Decimus Meridius

*Gladiator*

### 4.1. Overview of the chapter

Lithium manganese rich mixed metal oxides have been well studied during the last decade. They have a good capacity (exceeding capacities to  $200 \text{ mAh g}^{-1}$ )<sup>1</sup> and rate capability, which means that they are good candidates as cathodic materials in the next generation of Li-ion batteries. Among them,  $\text{Li}_{1.2}\text{Ni}_{0.13}\text{Mn}_{0.54}\text{Co}_{0.13}\text{O}_2$  (also known as  $0.5\text{Li}_2\text{MnO}_3\text{-}0.5\text{LiNi}_{1/3}\text{Mn}_{1/3}\text{Co}_{1/3}\text{O}_2$ ) is widely studied because it has an excellent capacity<sup>2, 3</sup> due to anionic redox activity, giving place to the formation of peroxo-like species to charge compensate the removal of  $\text{Li}^+$  ions during the charge / discharge process.<sup>4</sup>

In this chapter, an electrochemical and surface study for  $\text{Li}_{1.2}\text{Ni}_{0.13}\text{Mn}_{0.54}\text{Co}_{0.13}\text{O}_2$  was investigated, and the results are compared with another Li-rich intercalation material:  $\text{Li}_{1.2}\text{Ni}_{0.32}\text{Mn}_{0.4}\text{Co}_{0.08}\text{O}_2$ . The anionic redox activity and the formation of  $\text{O}^{\cdot-}$  species was investigated using XPS and Raman microscopy.

## **4.2. Introduction**

Layered Li-rich mixed metal oxides derive from  $\text{Li}_2\text{MnO}_3$  and can form a combination with layered structures giving place to compounds with the general formula of  $x\text{Li}_2\text{MnO}_3-(1-x)\text{LiMO}_2$  ( $M = \text{Mn, Ni, Co, Cr, Fe}$ ) which give place to the combination of two different crystallographic space group symmetries: the  $C2/m$  space group from  $\text{Li}_2\text{MnO}_3$  and the  $R\bar{3}m$  group from layered  $\text{LiMO}_2$ .

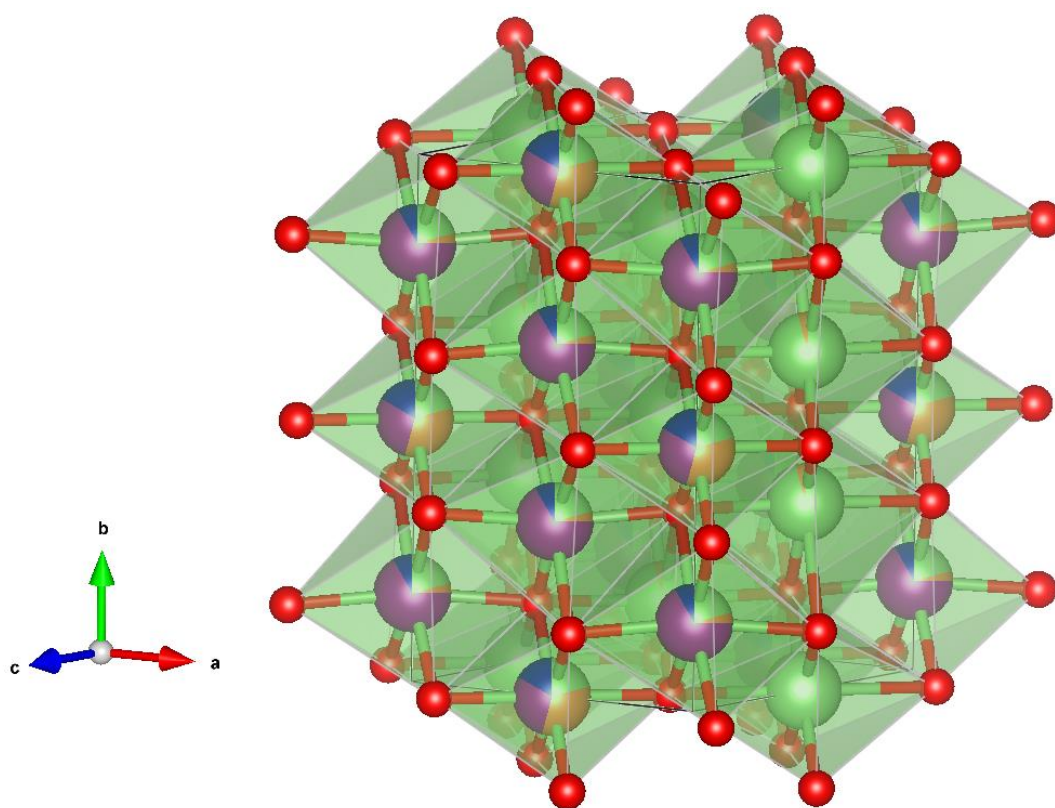


**Figure 4.1.** Schematic representation of  $\text{Li}_{1.2}\text{Ni}_{0.13}\text{Mn}_{0.54}\text{Co}_{0.13}\text{O}_2$  with  $\text{Li}_2\text{MnO}_3$  crystal structure type with space group  $C2/m$  of a basal plane layer showing the honeycomb of edge-sharing  $\text{MO}_6$  octahedra. The combination of transition metals are represented in blue, magenta and orange, Li atoms are represented in green and O atoms are represented in red. Figure drawn using VESTA software based on a CIF file obtained from ICSD database (Code 252816) and the bibliography.<sup>5</sup>

## ***Chapter 4. Electrochemical and surface behaviour for Li-rich row 1 transition metal oxides***

---

In spite of that, it is common to observe only the  $C2/m$  space group, giving place to rock-salt structures in which all the octahedral sites of the cubic close-packed oxygen array are occupied; these close-packed layers are highly compatible and allow the integration between the two components on an atomic level;<sup>6,7</sup> one example of this crystal structure is observed in  $\text{Li}_{1.2}\text{Ni}_{0.13}\text{Mn}_{0.54}\text{Co}_{0.13}\text{O}_2$  according to **Figure 4.1**.

The investigation of novel Li-rich mixed metal oxide materials has led to the synthesis of compounds with high electrochemical performance: improved cycling stabilities, higher rate capabilities than  $\text{LiNi}_{1/3}\text{Mn}_{1/3}\text{Co}_{1/3}\text{O}_2$ <sup>8-11</sup> and capacities exceeding  $200 \text{ mAh g}^{-1}$  due to the reversible redox of  $\text{O}^{2-}$  anions.<sup>1-3</sup> Therefore, these materials are very useful to understand the evolution of anionic redox and, regarding practical energy density and cost,<sup>12, 13</sup> the possibility to design new high-energy cathodes for Li-ion batteries.

The electrochemical performance and surface behaviour of  $\text{Li}_{1.2}\text{Ni}_{0.13}\text{Mn}_{0.54}\text{Co}_{0.13}\text{O}_2$  (abbreviated now on as LRNMC151) was studied along this chapter, and the results were compared with another Li-rich intercalation compound: this is  $\text{Li}_{1.2}\text{Ni}_{0.32}\text{Mn}_{0.4}\text{Co}_{0.08}\text{O}_2$  (named as LRNMC451), which is expected to have a comparable capacity and similar crystal structure.

### **4.3. Results**

#### **4.3.1. Crystal structure and morphology**

Elemental analysis in ICP-OES shows that both samples have the expected stoichiometry according to **Table 4.1**. A comparison of the morphology of the studied samples via scanning electron microscopy is shown in **Figure 4.2**. with low and high magnification ( $1 \mu\text{m}$  and  $100 \text{ nm}$  scale, respectively).

## ***Chapter 4. Electrochemical and surface behaviour for Li-rich row 1 transition metal oxides***

**Table 4.1.** Elemental analysis of the different samples using ICP-OES, with an error of  $\pm 0.001$ .

Sample	Li	Ni	Co	Mn
LRNMC151	1.19(0)	0.13(1)	0.13(8)	0.54(1)
LRNMC451	1.19(3)	0.32(1)	0.08(5)	0.40(2)

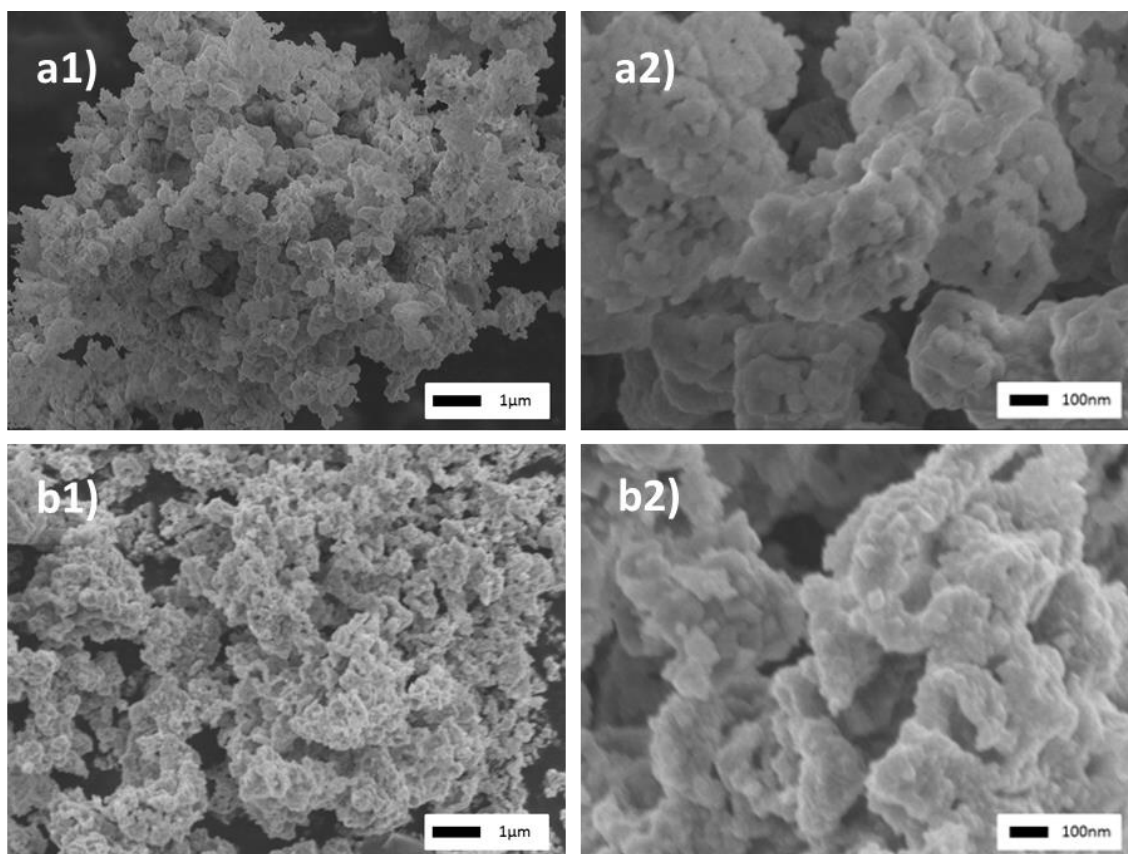


**Figure 4.2.** SEM images of the samples prepared via sol-gel synthetic route: a)  $\text{Li}_{1.2}\text{Ni}_{0.13}\text{Mn}_{0.54}\text{Co}_{0.13}\text{O}_2$  and b)  $\text{Li}_{1.2}\text{Ni}_{0.32}\text{Mn}_{0.4}\text{Co}_{0.08}\text{O}_2$ .

The observed diameter for  $\text{Li}_{1.2}\text{Ni}_{0.13}\text{Mn}_{0.54}\text{Co}_{0.13}\text{O}_2$  is  $\sim 200$  nm while in the case of  $\text{Li}_{1.2}\text{Ni}_{0.32}\text{Mn}_{0.4}\text{Co}_{0.08}\text{O}_2$  is  $\sim 140$  nm. BET measurements were used to calculate the surface area and the pore size of the samples (**Table 4.2.**) and shows a bigger surface area for  $\text{Li}_{1.2}\text{Ni}_{0.13}\text{Mn}_{0.54}\text{Co}_{0.13}\text{O}_2$ .



***Chapter 4. Electrochemical and surface behaviour for Li-rich row 1 transition metal oxides***

**Table 4.2.** A comparison between the surface area and porosity of the samples using BET measurements, as well as the approximate diameter of the particles measured in SEM.

Sample	Surface area (m <sup>2</sup> g <sup>-1</sup> )	Pore size (nm)	Diameter (nm)
LRNMC151	9.08 ± 0.10	6.59(4)	200
LRNMC451	7.11 ± 0.04	8.20(8)	140

Analysis of the crystal structure using powder X-ray diffraction shows different patterns for both samples according to their comparison using  $C2/m$  and  $R\bar{3}m$  group standards for  $\text{Li}_{1.2}\text{Ni}_{0.13}\text{Mn}_{0.54}\text{Co}_{0.13}\text{O}_2$ <sup>5</sup> (Code 252816 in ICSD database) and  $\text{LiNi}_{1/3}\text{Mn}_{1/3}\text{Co}_{1/3}\text{O}_2$ <sup>14</sup> (Code 171750) respectively as shown in **Figure 4.3**. It is observed that  $\text{Li}_{1.2}\text{Ni}_{0.13}\text{Mn}_{0.54}\text{Co}_{0.13}\text{O}_2$  is in good agreement with the theory and has the characteristic peaks from the  $C2/m$  space group. For  $\text{Li}_{1.2}\text{Ni}_{0.32}\text{Mn}_{0.4}\text{Co}_{0.08}\text{O}_2$ , the spectrum shows broad peaks, giving an unclear appreciation of which kind of space groups are formed.

Rietveld refinement analysis using FullProf Suite software demonstrates that both  $\text{Li}_{1.2}\text{Ni}_{0.13}\text{Mn}_{0.54}\text{Co}_{0.13}\text{O}_2$  and  $\text{Li}_{1.2}\text{Ni}_{0.32}\text{Mn}_{0.4}\text{Co}_{0.08}\text{O}_2$  have  $C2/m$  space group and therefore they have a  $\text{Li}_2\text{MnO}_3$ -like structure. The lattice parameters are represented in **Table 4.3.**, as well as the cell volumes.

**Table 4.3.** Cell parameters of  $\text{Li}_{1.2}\text{Ni}_{0.13}\text{Mn}_{0.54}\text{Co}_{0.13}\text{O}_2$  and  $\text{Li}_{1.2}\text{Ni}_{0.32}\text{Mn}_{0.4}\text{Co}_{0.08}\text{O}_2$ . The lattice constants were calculated using Rietveld refinement in FullProf Suite (error of ±0.003 Å).

Sample	a (Å)	b (Å)	c (Å)	β (degrees)	Cell volume (Å <sup>3</sup> )
LRNMC151	4.93(4)	8.54(9)	5.02(0)	109.14(4)	200.06(7)
LRNMC451	4.91(9)	8.65(4)	5.08(0)	109.60(5)	203.45(8)

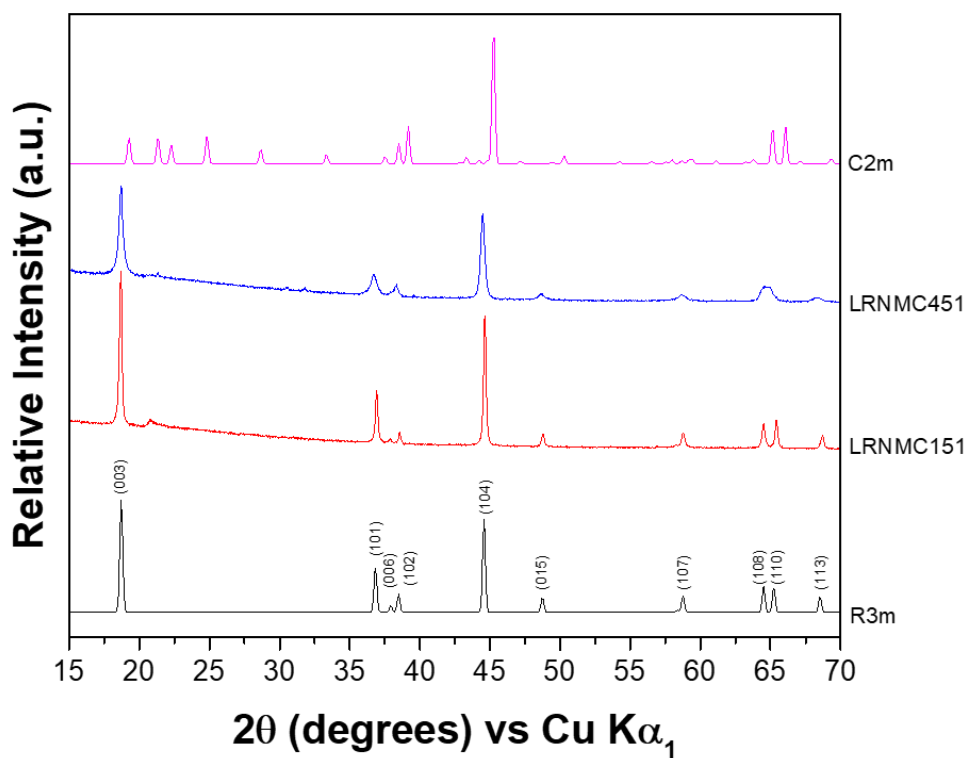


**Figure 4.3.** A comparison of X-ray diffraction spectrum between the studied samples; their patterns are compared with the standard space groups of  $C2/m$  and  $R\bar{3}m$  (Code 252816 and 171750 in ICSD database, respectively).<sup>5, 14</sup>

### 4.3.2. Electrochemical Properties

The electrochemical measurements of the different samples (cyclability and the differential capacity) are compared in **Figure 4.4.**;  $\text{Li}_{1.2}\text{Ni}_{0.13}\text{Mn}_{0.54}\text{Co}_{0.13}\text{O}_2$  and  $\text{Li}_{1.2}\text{Ni}_{0.32}\text{Mn}_{0.4}\text{Co}_{0.08}\text{O}_2$  were measured between 2 and 4.8 V vs.  $\text{Li}/\text{Li}^+$ .

The capacities measured shows different values depending of which sample is studied: for the cyclability at constant C-rate of  $100 \text{ mA g}^{-1}$ , the first cycle for  $\text{Li}_{1.2}\text{Ni}_{0.13}\text{Mn}_{0.54}\text{Co}_{0.13}\text{O}_2$  shows a discharge capacity of  $255 \text{ mAh g}^{-1}$  and in the case of  $\text{Li}_{1.2}\text{Ni}_{0.32}\text{Mn}_{0.4}\text{Co}_{0.08}\text{O}_2$  the discharge capacity is  $167 \text{ mAh g}^{-1}$ .  $\text{Li}_{1.2}\text{Ni}_{0.13}\text{Mn}_{0.54}\text{Co}_{0.13}\text{O}_2$

## Chapter 4. Electrochemical and surface behaviour for Li-rich row 1 transition metal oxides

shows a discharge capacity of 195 mAh g<sup>-1</sup> after 80 cycles, which means that there is a fade of 23.5%. For Li<sub>1.2</sub>Ni<sub>0.32</sub>Mn<sub>0.4</sub>Co<sub>0.08</sub>O<sub>2</sub> is obtained a discharge capacity of 126 mAh g<sup>-1</sup> after 80 cycles (capacity fade of 24.5%).

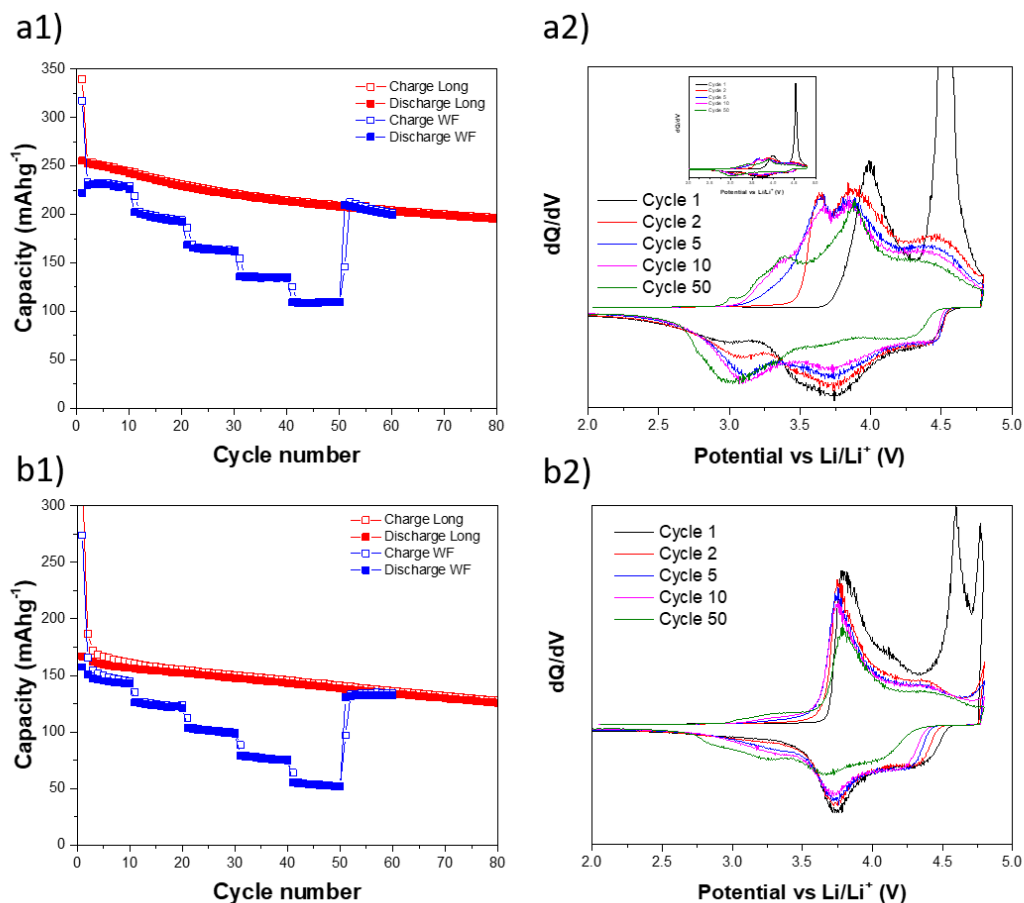


**Figure 4.4.** Comparison of the cyclability at a constant C-rate of 100 mA g<sup>-1</sup> and a variation of C-rate every 10 cycles (100, 200, 400, 800, 1600 and 100 mA g<sup>-1</sup>) and the differential capacity for (a) Li<sub>1.2</sub>Ni<sub>0.13</sub>Mn<sub>0.54</sub>Co<sub>0.13</sub>O<sub>2</sub> and (b) Li<sub>1.2</sub>Ni<sub>0.32</sub>Mn<sub>0.4</sub>Co<sub>0.08</sub>O<sub>2</sub>.

The differential capacity plots (measured at a constant C-rate of 100 mA g<sup>-1</sup>) show very different profiles for each sample. For Li<sub>1.2</sub>Ni<sub>0.13</sub>Mn<sub>0.54</sub>Co<sub>0.13</sub>O<sub>2</sub> the first charge shows two different peaks, one at ~3.9 V and an intense peak at ~4.5 V which corresponds to a potential plateau already reported in the literature and explained as the

## ***Chapter 4. Electrochemical and surface behaviour for Li-rich row 1 transition metal oxides***

---

simultaneous extraction of lithium and oxygen.<sup>15-18</sup> The first discharge shows a shoulder at ~4.5 V and a peak at ~3.75 V, and a small peak at ~3 V can also be appreciated. For the second and the following cycles, the charge peaks appear at ~3.75 V and ~4.5 V (which is now very small compared with the first cycle) and discharge peaks at ~4.5 V and ~3.75 V similar to the first discharge but now appears a peak at ~3.1 V that increase with the increasing number of cycles.

For  $\text{Li}_{1.2}\text{Ni}_{0.32}\text{Mn}_{0.4}\text{Co}_{0.08}\text{O}_2$  in the first charge peaks appear at ~3.75 V, ~4.1 V, ~4.5 V and ~4.75 V, in the discharge the peaks appear at ~4.5 V and ~3.75 V; for the following cycles, the plots show a strong peak at ~3.75 V and a shoulder at ~4.4 V during charge, while discharge is similar to first cycle.

For these two samples, the redox peaks that appear at ~3.75 V can be attributed to the electrochemical redox reactions that involve  $\text{Ni}^{2+/4+}$  (via the two-step process from  $\text{Ni}^{2+/3+}$  to  $\text{Ni}^{3+/4+}$ )<sup>19-21</sup> as it was established in **Chapter 3**. In the case of the redox peak that appears at ~4.5 V during charge, it can be assigned to anion redox, forming some oxidised  $\text{O}^{n-}$  species, and also to  $\text{Co}^{3+/4+}$ . It is interesting that the differential capacity plot for  $\text{Li}_{1.2}\text{Ni}_{0.32}\text{Mn}_{0.4}\text{Co}_{0.08}\text{O}_2$  shows more peaks during first charge, leaving this as an unsolved question at this point.

The galvanostatic cycles display a plateau at ~4.5 V for  $\text{Li}_{1.2}\text{Ni}_{0.13}\text{Mn}_{0.54}\text{Co}_{0.13}\text{O}_2$ , and it is also quite interesting what is the expected movement of  $\text{Li}^+$  ions during charge and discharge as it is shown in **Figure 4.5**.

The observed galvanostatic profiles vary considerable between first and second cycle in both materials, which is directly related with what was observed in the differential capacity plots; in that way, the observed plateau at ~4.5 V in the first charge is bigger for  $\text{Li}_{1.2}\text{Ni}_{0.13}\text{Mn}_{0.54}\text{Co}_{0.13}\text{O}_2$  than for  $\text{Li}_{1.2}\text{Ni}_{0.32}\text{Mn}_{0.4}\text{Co}_{0.08}\text{O}_2$  and this is directly related with

***Chapter 4. Electrochemical and surface behaviour for Li-rich row 1 transition metal oxides***

the redox charge peak. It is also noteworthy that, according to the calculations, the Li loss in the case of  $\text{Li}_{1.2}\text{Ni}_{0.32}\text{Mn}_{0.4}\text{Co}_{0.08}\text{O}_2$  is more important than in  $\text{Li}_{1.2}\text{Ni}_{0.13}\text{Mn}_{0.54}\text{Co}_{0.13}\text{O}_2$  and this is directly related with the charge capacity of both materials, although this difference in capacity between charge and discharge is not too important for the second cycle of each sample.

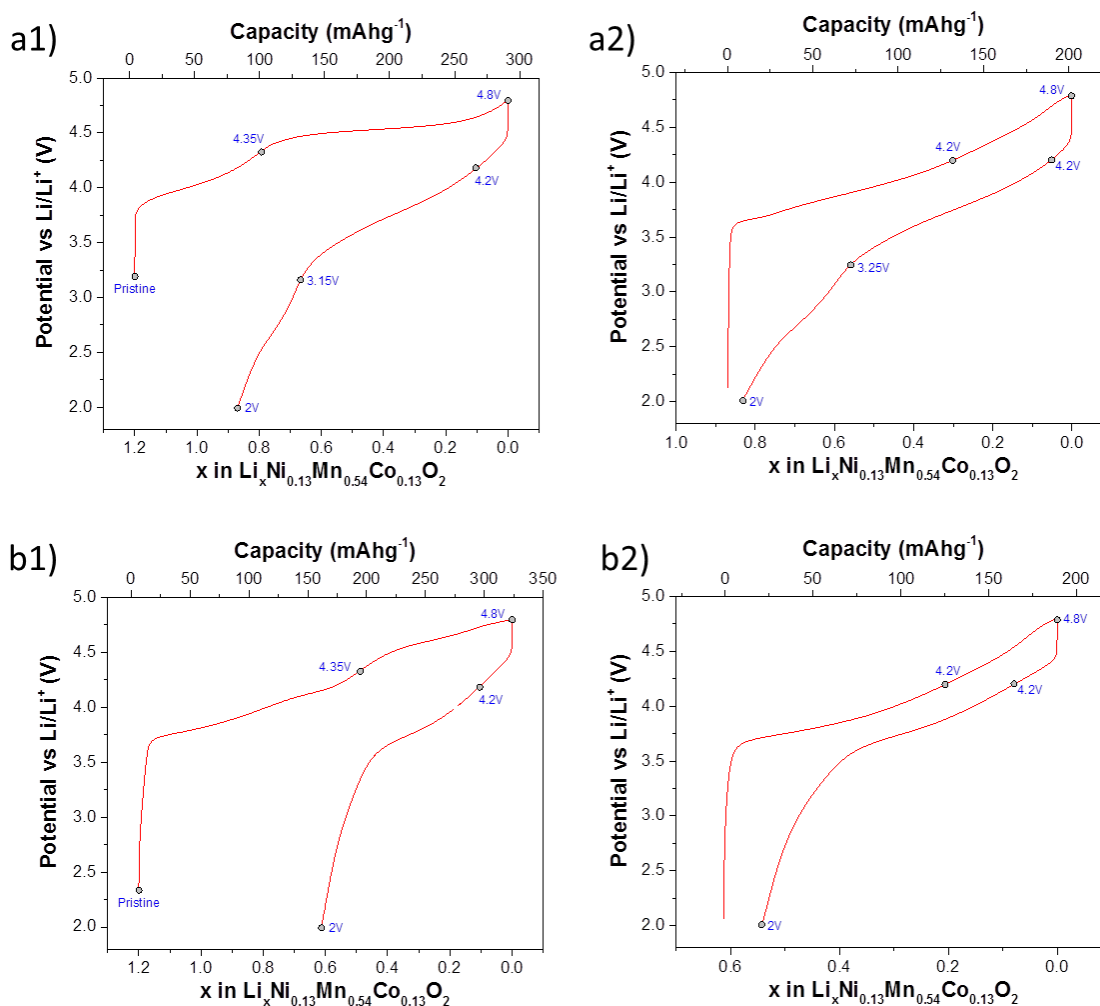


**Figure 4.5.** Comparison between first and second charge / discharge process and the expected loss of Li atoms in the stoichiometry of the material after the first two cycles for (a)  $\text{Li}_{1.2}\text{Ni}_{0.13}\text{Mn}_{0.54}\text{Co}_{0.13}\text{O}_2$  and (b)  $\text{Li}_{1.2}\text{Ni}_{0.32}\text{Mn}_{0.4}\text{Co}_{0.08}\text{O}_2$ .

### 4.3.3. Surface behaviour and anion redox reactions

In order to understand the electrochemical behaviour and investigate the participation of anionic redox as an important reason of the good capacities obtained for such materials, a detailed surface study via X-ray photoelectron spectroscopy is done and several electrodes were measure at different states of charge and discharge (as represented in **Figure 4.5.**). The obtained results for O 1s at different voltages during the first two cycles for both materials are shown in **Figure 4.6.**

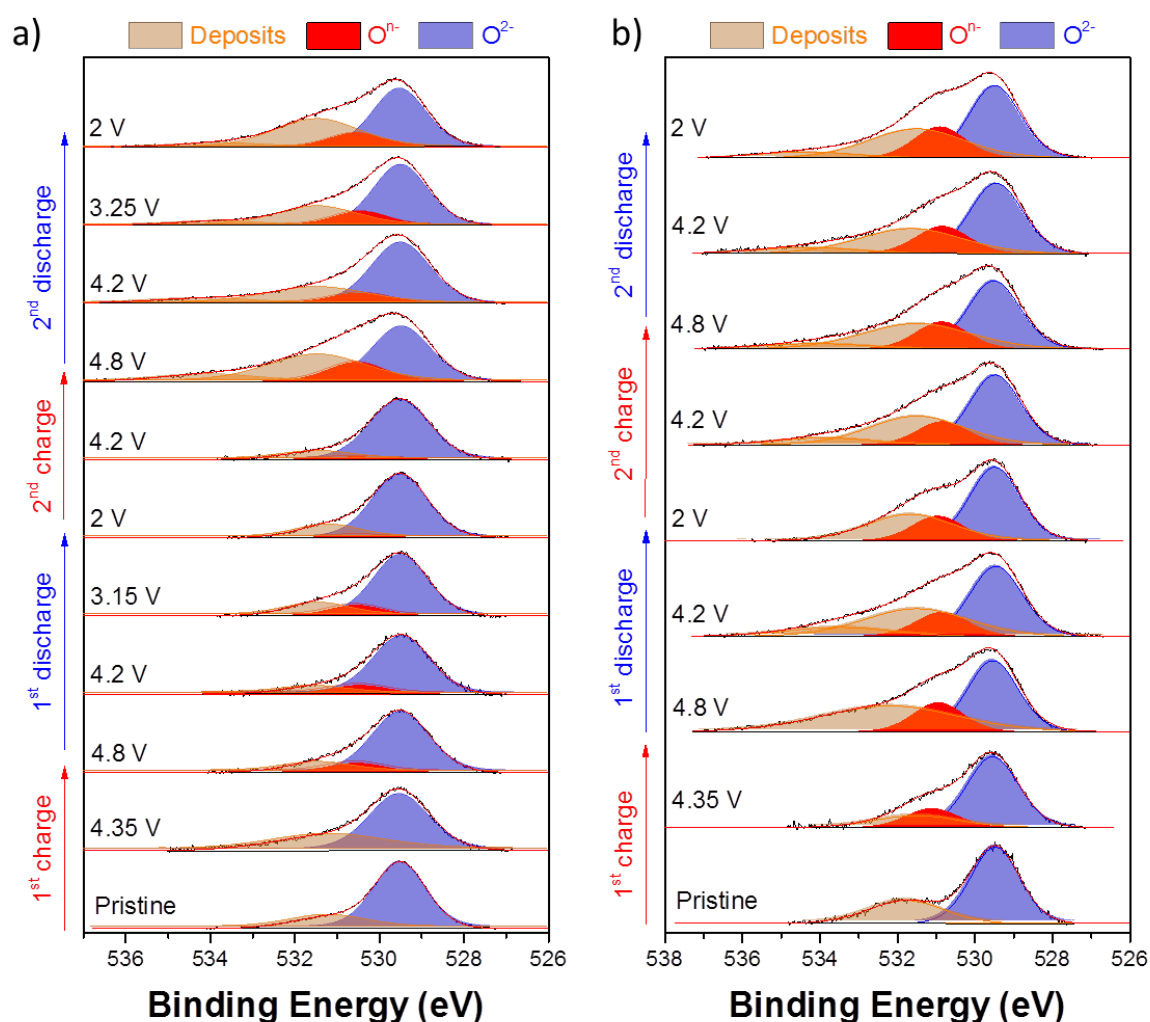


**Figure 4.6.** X-ray photoelectron spectroscopy data collected at O 1s energies in the first two charge / discharge cycles of (a)  $Li_{1.2}Ni_{0.13}Mn_{0.54}Co_{0.13}O_2$  and (b)  $Li_{1.2}Ni_{0.32}Mn_{0.4}Co_{0.08}O_2$ .

## ***Chapter 4. Electrochemical and surface behaviour for Li-rich row 1 transition metal oxides***

---

Charge correction was done using O 1s, implementing the strongest component after deconvolution at 529.5 eV, which corresponds to the non-oxidised O<sup>2-</sup> at 529.5 eV (blue colour); the oxidised O<sup>n-</sup> ( $0 \leq n < 2$ ) was observed at 530.5 eV (red colour). Other contributions for these peaks are the surface deposits from decomposition products of the carbonate-based electrolyte forming the CEI layer and/or possible contamination with dimethyl carbonate at ~532 eV (orange colour).

The comparison between both materials shows important differences of the evolution of oxygen. For one part, in the case of Li<sub>1.2</sub>Ni<sub>0.13</sub>Mn<sub>0.54</sub>Co<sub>0.13</sub>O<sub>2</sub> the formation of oxidised O<sup>n-</sup> species takes place beyond ~4.35 V and therefore can be associated to the redox peak at ~4.5 V (as formation of peroxo-like species can be observed in the sample charged at ~4.8 V). However, Li<sub>1.2</sub>Ni<sub>0.32</sub>Mn<sub>0.4</sub>Co<sub>0.08</sub>O<sub>2</sub> already shows formation of O<sup>n-</sup> species in the electrode charged at ~4.35 V, which means that the shoulder observed at ~4.1 V can be attributed to anionic oxidation, although this contribution is small. For both samples, oxidised O<sup>n-</sup> species are observed when electrodes are fully charged at 4.8 V.

Upon discharge, the relative contribution of the oxidised O<sup>n-</sup> peak decreases compared to that of the non-oxidised O<sup>2-</sup> feature, but does not fully disappear for Li<sub>1.2</sub>Ni<sub>0.13</sub>Mn<sub>0.54</sub>Co<sub>0.13</sub>O<sub>2</sub>, suggesting that some of the oxidised O<sup>n-</sup> species formed are not reduced back to oxide. In the second cycle, the contribution of the O<sup>n-</sup> peak at full charge is bigger compared with the first cycle, as well as the electrode fully discharged, suggesting the accumulation of oxidised O<sup>n-</sup> with the increase number of cycles. In the case of Li<sub>1.2</sub>Ni<sub>0.32</sub>Mn<sub>0.4</sub>Co<sub>0.08</sub>O<sub>2</sub>, once the O<sup>n-</sup> species are formed during first charge, their contribution remain unchanged even at full discharge, and does not change in the second cycle either.

## Chapter 4. Electrochemical and surface behaviour for Li-rich row 1 transition metal oxides

A better appreciation of the variation of the  $O^{n-}$  species and the average oxidation state for oxygen is shown in **Figure 4.7**, and it is also compared with the oxidation state of Mn, Co and Ni. The calculation of the oxidation state for both Mn, Ni and Co were made with the doublet separation and the shift in the position of Mn 2p, Co 2p and Ni 2p, while the calculation for the oxidation state for O was done by comparison of the percentages of contributions between the non-oxidised  $O^{2-}$  and the oxidised  $O^{n-}$  components. This was also confirmed using an alternative method consisting in measuring the expected oxidation state for oxygen in order to charge compensate the Li loss and the oxidised Mn, Co and Ni.

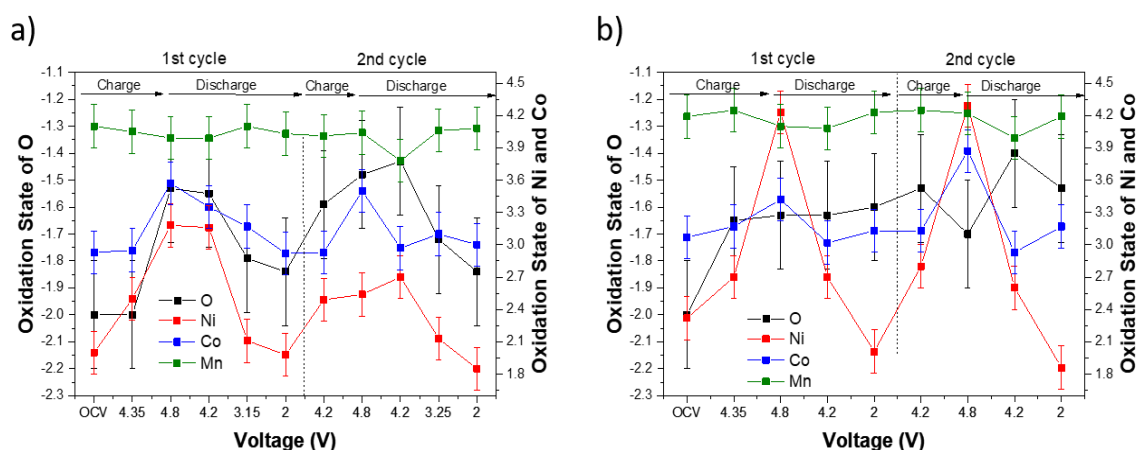


**Figure 4.7.** Variation of the oxidation state for O, Ni, Co and Mn for (a)  $Li_{1.2}Ni_{0.13}Mn_{0.54}Co_{0.13}O_2$  and (b)  $Li_{1.2}Ni_{0.32}Mn_{0.4}Co_{0.08}O_2$  on the first two charge / discharge cycles according to their measurements using XPS, with an error of  $\pm 0.2$ .

Focusing on  $Li_{1.2}Ni_{0.13}Mn_{0.54}Co_{0.13}O_2$ , the evolution of oxidised  $O^{n-}$  can be well established where the oxidation state of oxygen is -2 in the pristine electrode, increasing until -1.5 upon full charge and decreasing to -1.8 on full discharge. The same behaviour was observed in the second cycle (-1.5 at full charge and -1.8 at full discharge). In the



case of the oxidation state of the transition metals, the maximum oxidation state for Ni was measured as +3.2 at full charge in the first cycle and +2.5 in the second cycle, while the oxidation state for the full discharge samples is +2. For Co, the variation of oxidation states is +3 for the pristine electrode, +3.5 at full charge in both first and second cycle and +3 at full discharge. Mn remains around +4 with little variations in all cases.

In the case of  $\text{Li}_{1.2}\text{Ni}_{0.32}\text{Mn}_{0.4}\text{Co}_{0.08}\text{O}_2$  electrodes, oxygen rises from -2 in the pristine sample until -1.6 at full charge, remaining unchanged (with slight variations) since then. For this material, the most important variations are taking place at Ni, with a variation from +2 in the pristine electrode to +4 at full charge at 4.8 V, reducing back to +2 during full discharge, and this process is repeated in the second cycle. Co has more importance in the second cycle: in the first cycle is oxidised from +3 (pristine electrode) to +3.5 (fully charged) but in the second cycle is oxidised from +3 (fully discharged after the first cycle) to +4 (fully charged) to come back to +3 at full discharge at 2 V. As for  $\text{Li}_{1.2}\text{Ni}_{0.13}\text{Mn}_{0.54}\text{Co}_{0.13}\text{O}_2$ , Mn remains around +4 with little variations in all cases.

#### **4.3.4. Raman measurements and formation of $\text{O}^{\text{n-}}$ in the bulk**

The anion redox process is observed in the surface of the samples and can explain the higher capacity for  $\text{Li}_{1.2}\text{Ni}_{0.13}\text{Mn}_{0.54}\text{Co}_{0.13}\text{O}_2$  with a clear evolution of oxygen during charge and discharge, while in  $\text{Li}_{1.2}\text{Ni}_{0.32}\text{Mn}_{0.4}\text{Co}_{0.08}\text{O}_2$  is the cationic redox from the transition metals that has more importance.

To check the formation of oxidised  $\text{O}^{\text{n-}}$  species in the bulk structure for both compounds, *ex situ* Raman spectra of the samples at different states of charge and discharge was measured (according to the different states assigned in **Figure 4.5.**) and the results are shown in **Figure 4.8.**

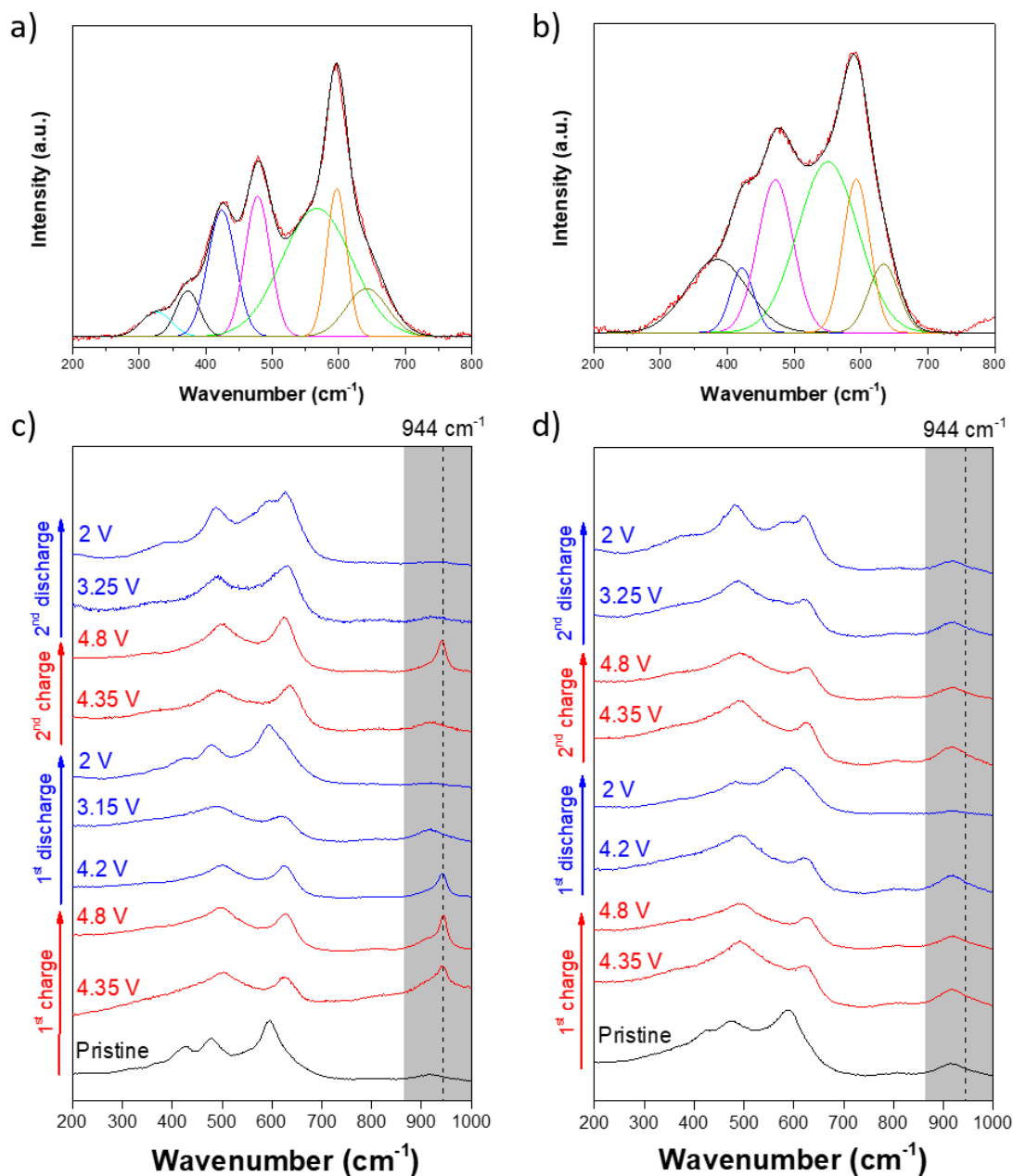


**Figure 4.8.** *Ex situ* Raman spectra for the pristine electrodes of (a)  $\text{Li}_{1.2}\text{Ni}_{0.13}\text{Mn}_{0.54}\text{Co}_{0.13}\text{O}_2$  and (b)  $\text{Li}_{1.2}\text{Ni}_{0.32}\text{Mn}_{0.4}\text{Co}_{0.08}\text{O}_2$  and at different states of charge / discharge in the first two cycles for (c)  $\text{Li}_{1.2}\text{Ni}_{0.13}\text{Mn}_{0.54}\text{Co}_{0.13}\text{O}_2$  and (d)  $\text{Li}_{1.2}\text{Ni}_{0.32}\text{Mn}_{0.4}\text{Co}_{0.08}\text{O}_2$ . The area where is expected to have  $\text{M-O}^n$  species (between 860 and 1000  $\text{cm}^{-1}$ ) is highlighted. Raman measurements were carried out by Dr Filipe Braga and analysed by myself.

***Chapter 4. Electrochemical and surface behaviour for Li-rich row 1 transition metal oxides***

In **Figure 4.8a.** and **Figure 4.8b.**, the region between 300 and 800  $\text{cm}^{-1}$  corresponding to the pristine electrodes for both samples is shown and has some differences compared with the  $\text{LiNi}_{1/3}\text{Mn}_{1/3}\text{Co}_{1/3}\text{O}_2$  spectra observed in **Chapter 3**. According to Nanda *et. al.*,<sup>22</sup> the bonds measured at  $\sim 480$  and  $\sim 600$   $\text{cm}^{-1}$  correspond to the  $E_g$  and  $A_{1g}$  modes for the  $R\bar{3}m$  space group,<sup>10, 23</sup> respectively, and the bonds at  $\sim 420$  and  $\sim 560$   $\text{cm}^{-1}$  are the  $B_g$  and  $A_g$  modes for the  $C2/m$  space group,<sup>24, 25</sup> respectively. The shoulder at  $\sim 640$   $\text{cm}^{-1}$  correspond to the  $\nu_{\text{Mn-O}}$  bond from the lithium manganese rich material, as reported previously.<sup>10, 26-28</sup> These results are shown in detail in **Table 4.4**.

The intensity of the different modes is different for each compound, one of the possible reasons could be attributed to the contribution of each space group in the crystal structure. The bands observed between 300 and 400  $\text{cm}^{-1}$  are poorly resolved and can be related with the  $\nu_{\text{Mn-O}}$  bond for the  $R\bar{3}m$  space group.<sup>24</sup>

**Table 4.4.** A comparison of the Raman shifts and percentage of area for the different measured bands in  $\text{Li}_{1.2}\text{Ni}_{0.13}\text{Mn}_{0.54}\text{Co}_{0.13}\text{O}_2$  and  $\text{Li}_{1.2}\text{Ni}_{0.32}\text{Mn}_{0.4}\text{Co}_{0.08}\text{O}_2$ .

Band	LRNMC151		LRNMC451	
	Position ( $\text{cm}^{-1}$ )	Area (%)	Position ( $\text{cm}^{-1}$ )	Area (%)
$\nu_{\text{Mn-O}}$	326	3.23	-	-
$\nu_{\text{Mn-O}}$	373	4.69	385	15.87
$B_g$	424	15.53	422	5.46
$E_g$	478	15.56	472	19.50
$A_g$	567	39.32	550	37.04
$A_{1g}$	597	12.95	593	14.80
$\nu_{\text{Mn-O}}$	642	8.71	634	7.34

## ***Chapter 4. Electrochemical and surface behaviour for Li-rich row 1 transition metal oxides***

---

Concentrating on  $\text{Li}_{1.2}\text{Ni}_{0.13}\text{Mn}_{0.54}\text{Co}_{0.13}\text{O}_2$  in **Figure 4.8c.**, a formation of a new peak at  $\sim 940\text{ cm}^{-1}$  and a shoulder at  $\sim 920\text{ cm}^{-1}$  is observed in the electrode charged at 4.35 V (first cycle), the first one can be attributed to the formation of O-O stretching bond in the  $\text{M-O}^n$  species according to the “Infrared and Raman Characteristic Group Frequencies” database.<sup>2, 29</sup> The shoulder at  $\sim 920\text{ cm}^{-1}$  is related with the C-C stretching mode due to the presence of the conductive additive in the measured electrode.<sup>29</sup> The disappearance of the  $\nu_{\text{Co-O}}$  bond ( $\sim 597\text{ cm}^{-1}$ ) could correspond to the oxidation of  $\text{Co}^{3+}$  to  $\text{Co}^{4+}$ ; the  $\nu_{\text{Li-O}}$  bond ( $\sim 487\text{ cm}^{-1}$ ) also disappears, related with the deintercalation of  $\text{Li}^+$  ions.

The spectrum remains unchanged until discharge at 3.15 V (first cycle), where the peak observed at  $\sim 940\text{ cm}^{-1}$  disappears and now only the shoulder at  $\sim 920\text{ cm}^{-1}$  is observed; the electrode fully discharged at 2 V has a very similar spectrum than the pristine one. Similar behaviour is observed in the second cycle, but now the electrode charged at 4.35 V does not have the peak at  $\sim 940\text{ cm}^{-1}$ , which is now only observed on fully charge at 4.8 V; now, at fully discharge, the intensity of some bonds has changed compared with the pristine electrode.

The evolution of the Raman spectra for  $\text{Li}_{1.2}\text{Ni}_{0.32}\text{Mn}_{0.4}\text{Co}_{0.08}\text{O}_2$  in the first two cycles is observed in **Figure 4.8d.** and can be compared to the results for  $\text{Li}_{1.2}\text{Ni}_{0.13}\text{Mn}_{0.54}\text{Co}_{0.13}\text{O}_2$  and the most important change is the disappearance of the sharp peak at  $\sim 940\text{ cm}^{-1}$  and only observing the broad band at  $\sim 920\text{ cm}^{-1}$ , which means that the formation of peroxy-like species for this compound is not observed in the bulk.

### **4.4. Discussion**

The SEM images in **Figure 4.2.** shows the expected particle size and agglomeration according to the resorcinol-formaldehyde sol-gel polymerisation synthesis as explained

## ***Chapter 4. Electrochemical and surface behaviour for Li-rich row 1 transition metal oxides***

---

in **Chapter 3**. Crystal structure analysed via PXRD (**Figure 4.3.**) shows very different spectra between both samples: while  $\text{Li}_{1.2}\text{Ni}_{0.13}\text{Mn}_{0.54}\text{Co}_{0.13}\text{O}_2$  has very sharp peaks associated with good crystal structure in a single layer,  $\text{Li}_{1.2}\text{Ni}_{0.32}\text{Mn}_{0.4}\text{Co}_{0.08}\text{O}_2$  has very broad peaks and it is very difficult to differentiate between each other (such as the broad peak at  $\sim 65^\circ$  that should correspond to two different peaks according to its comparison with  $\text{Li}_{1.2}\text{Ni}_{0.13}\text{Mn}_{0.54}\text{Co}_{0.13}\text{O}_2$  and the literature standards). This could be related with the formation of multiple single crystals that are randomly distributed giving place to a polycrystalline material.<sup>30, 31</sup> This could explain the differential capacity for  $\text{Li}_{1.2}\text{Ni}_{0.32}\text{Mn}_{0.4}\text{Co}_{0.08}\text{O}_2$  as observed in **Figure 4.4b.**, where the shoulder at  $\sim 4.1$  V and the peak at  $\sim 4.75$  V observed during first charge could be indeed additional peaks from  $\sim 3.75$  V and  $\sim 4.5$  V due to the different observed faces. This explanation has to be investigated further in future measurements.

The electrochemical measurements in **Figure 4.4.** show capacities in the first cycles up to  $255 \text{ mAh g}^{-1}$  for  $\text{Li}_{1.2}\text{Ni}_{0.13}\text{Mn}_{0.54}\text{Co}_{0.13}\text{O}_2$ , while  $\text{Li}_{1.2}\text{Ni}_{0.32}\text{Mn}_{0.4}\text{Co}_{0.08}\text{O}_2$  has lower capacities (up to  $167 \text{ mAh g}^{-1}$ ). This is associated with oxygen redox process, as can be appreciated with the intense peak observed at  $\sim 4.5$  V for  $\text{Li}_{1.2}\text{Ni}_{0.13}\text{Mn}_{0.54}\text{Co}_{0.13}\text{O}_2$ . In the case of  $\text{Li}_{1.2}\text{Ni}_{0.32}\text{Mn}_{0.4}\text{Co}_{0.08}\text{O}_2$ , this peak is not that strong which means that anion redox is almost inactive.

The possible loss of  $\text{Li}^+$  ions for  $\text{Li}_{1.2}\text{Ni}_{0.32}\text{Mn}_{0.4}\text{Co}_{0.08}\text{O}_2$  (more important than for  $\text{Li}_{1.2}\text{Ni}_{0.13}\text{Mn}_{0.54}\text{Co}_{0.13}\text{O}_2$ ) as observed in **Figure 4.5.** could be related with a change in the crystal phase<sup>32, 33</sup> and this also can explain why the evolution of oxygen for this compound does not change once the  $\text{O}^{\text{n-}}$  species are formed during first charge to charge compensate the loss of lithium ions, according to the XPS measurements showed in **Figure 4.6.**, and also the change in Raman profile in **Figure 4.8.**

## ***Chapter 4. Electrochemical and surface behaviour for Li-rich row 1 transition metal oxides***

---

$\text{Li}_{1.2}\text{Ni}_{0.13}\text{Mn}_{0.54}\text{Co}_{0.13}\text{O}_2$  has a clearer and efficient evolution of oxygen during the first two cycles (also confirmed with Raman measurements according to **Figure 4.8.**). This can also explain why the differential capacity plots between the first and second cycle are different in both materials, and why the anion redox activity is more important for  $\text{Li}_{1.2}\text{Ni}_{0.13}\text{Mn}_{0.54}\text{Co}_{0.13}\text{O}_2$  than for  $\text{Li}_{1.2}\text{Ni}_{0.32}\text{Mn}_{0.4}\text{Co}_{0.08}\text{O}_2$  (where the redox activity for the transition metals are more important on the other hand), directly related with the lower capacity for  $\text{Li}_{1.2}\text{Ni}_{0.32}\text{Mn}_{0.4}\text{Co}_{0.08}\text{O}_2$  compared to  $\text{Li}_{1.2}\text{Ni}_{0.13}\text{Mn}_{0.54}\text{Co}_{0.13}\text{O}_2$ , and confirming that anion redox activity is really important to obtain a higher capacity in this type of Li-rich compounds.

Raman measurements show in **Figure 4.8.** the vibration bonds between the transition metals and oxygen, and the evolution of peroxo-like bond in  $\text{Li}_{1.2}\text{Ni}_{0.13}\text{Mn}_{0.54}\text{Co}_{0.13}\text{O}_2$  is attributed to the peak at  $944\text{ cm}^{-1}$  although it was never reported before (even with detailed Raman studies done by Bruce *et al.*<sup>2</sup> and Nanda *et al.*<sup>22</sup> among others), which can mean that this could be the first time that the O-O stretching bonds can be observed in this compound, but this possibility has to be confirmed in future measurements. One of the possible reasons why this bond is observed could be attributed to resorcinol-formaldehyde sol-gel polymerisation synthesis and the synthesis conditions.

The Raman band at  $\sim 940\text{ cm}^{-1}$  is not observed in  $\text{Li}_{1.2}\text{Ni}_{0.32}\text{Mn}_{0.4}\text{Co}_{0.08}\text{O}_2$ , although XPS shows the oxidation of oxygen, which can suggest that  $\text{Li}_{1.2}\text{Ni}_{0.32}\text{Mn}_{0.4}\text{Co}_{0.08}\text{O}_2$  has only superficial anion redox while in the case of  $\text{Li}_{1.2}\text{Ni}_{0.13}\text{Mn}_{0.54}\text{Co}_{0.13}\text{O}_2$  also reaches the bulk. The reason behind this behaviour is not totally clear and has to be investigated in further studies.

## **4.5. Conclusions**

Two different Li-rich intercalation materials have been studied in this work, and the anion redox could be established with XPS measurements, which was essential in order to observe the evolution of oxygen for both compounds. Anion redox activity is more important for  $\text{Li}_{1.2}\text{Ni}_{0.13}\text{Mn}_{0.54}\text{Co}_{0.13}\text{O}_2$  than for  $\text{Li}_{1.2}\text{Ni}_{0.32}\text{Mn}_{0.4}\text{Co}_{0.08}\text{O}_2$ , as also suggest the differential capacity plots and the obtained capacity. The charge compensation mechanism due to anionic redox is easier for this compound, helping to obtain high capacities. This difference in the results could be related with the crystal structure for each compound, and further measurements have to be done.

The results for  $\text{Li}_{1.2}\text{Ni}_{0.32}\text{Mn}_{0.4}\text{Co}_{0.08}\text{O}_2$  are more complicated to establish because there were not previous studies for this compound, and future measurements have to be undergone to try to solve some questions related mainly with Raman measurements.

The conclusion for this work is that not all Li-rich compounds behave in the same way, where some of them have a more important cation redox contribution than anion redox. Involving the evolution of oxygen is related with a better electrochemical performance and higher capacities; this anion redox is key in the development of new cathodic materials for commercial purposes, and further studies need to be done in order to their future synthesis in a big scale.

## **4.6. References**

1. P. Rozier and J. M. Tarascon, *J. Electrochem. Soc.*, 2015, **162**, A2490-A2499.
2. K. Luo, M. R. Roberts, R. Hao, N. Guerrini, D. M. Pickup, Y.-S. Liu, K. Edström, J. Guo, A. V. Chadwick and L. C. Duda, *Nat. Chem.*, 2016, **8**, 684.
3. D.-H. Seo, J. Lee, A. Urban, R. Malik, S. Kang and G. Ceder, *Nat. Chem.*, 2016, **8**, 692.
4. G. Assat, D. Foix, C. Delacourt, A. Iadecola, R. Dedryvère and J.-M. Tarascon, *Nat. Commun.*, 2017, **8**, 2219.
5. N. Ishida, N. Tamura, N. Kitamura and Y. Idemoto, *J. Power Sources*, 2016, **319**, 255-261.
6. C. S. Johnson, N. Li, C. Lefief, J. T. Vaughey and M. M. Thackeray, *Chem. Mater.*, 2008, **20**, 6095-6106.
7. M. M. Thackeray, S.-H. Kang, C. S. Johnson, J. T. Vaughey, R. Benedek and S. Hackney, *J. Mater. Chem.*, 2007, **17**, 3112-3125.
8. J.-M. Kim, N. Kumagai and H.-T. Chung, *Electrochem. Solid-State Lett.*, 2006, **9**, A494-A498.
9. H. Yu, H. Kim, Y. Wang, P. He, D. Asakura, Y. Nakamura and H. Zhou, *Phys. Chem. Chem. Phys.*, 2012, **14**, 6584-6595.
10. P. Lanz, C. Villevieille and P. Novák, *Electrochim. Acta*, 2014, **130**, 206-212.
11. S.-H. Yu, T. Yoon, J. Mun, S. Park, Y.-S. Kang, J.-H. Park, S. M. Oh and Y.-E. Sung, *J. Mater. Chem. A*, 2013, **1**, 2833-2839.
12. E. J. Berg, C. Villevieille, D. Streich, S. Trabesinger and P. Novák, *J. Electrochem. Soc.*, 2015, **162**, A2468-A2475.



***Chapter 4. Electrochemical and surface behaviour for Li-rich row I transition metal oxides***

---

13. K. G. Gallagher, S. Goebel, T. Greszler, M. Mathias, W. Oelerich, D. Eroglu and V. Srinivasan, *Energy Environ. Sci.*, 2014, **7**, 1555-1563.
14. S. C. Yin, Y. H. Rho, I. Swainson and L. F. Nazar, *Chem. Mater.*, 2006, **18**, 1901-1910.
15. Z. Lu and J. R. Dahn, *J. Electrochem. Soc.*, 2002, **149**, A815-A822.
16. N. Tran, L. Croguennec, M. Ménétrier, F. Weill, P. Biensan, C. Jordy and C. Delmas, *Chem. Mater.*, 2008, **20**, 4815-4825.
17. C. Gan, H. Zhan, X. Hu and Y. Zhou, *Electrochem. Commun.*, 2005, **7**, 1318-1322.
18. N. Yabuuchi, K. Yoshii, S.-T. Myung, I. Nakai and S. Komaba, *J. Am. Chem. Soc.*, 2011, **133**, 4404-4419.
19. K. Shaju, G. S. Rao and B. Chowdari, *Electrochim. Acta*, 2002, **48**, 145-151.
20. Y. Koyama, N. Yabuuchi, I. Tanaka, H. Adachi and T. Ohzuku, *J. Electrochem. Soc.*, 2004, **151**, A1545-A1551.
21. Y.-J. Shin, W.-J. Choi, Y.-S. Hong, S. Yoon, K. S. Ryu and S. H. Chang, *Solid State Ionics*, 2006, **177**, 515-521.
22. R. E. Ruther, A. F. Callender, H. Zhou, S. K. Martha and J. Nanda, *J. Electrochem. Soc.*, 2015, **162**, A98-A102.
23. A. M. A. Hashem, A. E. Abdel-Ghany, A. E. Eid, J. Trottier, K. Zaghib, A. Mauger and C. M. Julien, *J. Power Sources*, 2011, **196**, 8632-8637.
24. C. M. Julien and M. Massot, *Mater. Sci. Eng. B*, 2003, **100**, 69-78.
25. H.-S. Park, S.-J. Hwang and J.-H. Choy, *J. Phys. Chem. B*, 2001, **105**, 4860-4866.
26. H. Koga, L. Croguennec, M. Ménétrier, K. Dohhil, S. Belin, L. Bourgeois, E. Suard, F. Weill and C. Delmas, *J. Electrochem. Soc.*, 2013, **160**, A786-A792.

***Chapter 4. Electrochemical and surface behaviour for Li-rich row 1 transition metal oxides***

---

27. Z. Li, F. Du, X. Bie, D. Zhang, Y. Cai, X. Cui, C. Wang, G. Chen and Y. Wei, *J. Phys. Chem. C*, 2010, **114**, 22751-22757.
28. H. Koga, L. Croguennec, P. Manessiez, M. Ménétrier, F. Weill, L. Bourgeois, M. Duttine, E. Suard and C. Delmas, *J. Phys. Chem. C*, 2012, **116**, 13497-13506.
29. D. A. Long, *J. Raman Spectrosc.*, 2004, **35**, 905-905.
30. R. Weber, C. R. Fell, J. Dahn and S. Hy, *J. Electrochem. Soc.*, 2017, **164**, A2992-A2999.
31. J. Li, A. R. Cameron, H. Li, S. Glazier, D. Xiong, M. Chatzidakis, J. Allen, G. Botton and J. Dahn, *J. Electrochem. Soc.*, 2017, **164**, A1534-A1544.
32. P. Hou, G. Chu, J. Gao, Y. Zhang and L. Zhang, *Chin. Phys. B*, 2016, **25**, 016104.
33. H. Koga, L. Croguennec, M. Ménétrier, P. Manessiez, F. Weill and C. Delmas, *J. Power Sources*, 2013, **236**, 250-258.

# Chapter 5.

## Electrochemical and surface behaviour of Li-rich nickel tungsten oxides

*“I’m just a simple man trying to make my way in the universe.”*

Jango Fett

*Star Wars: Episode II - Attack of the Clones*

### 5.1. Overview of the chapter

In this chapter, a novel non-stoichiometric  $\text{Li}_2\text{MO}_3$ -type compound with a heavy metal ion is proposed:  $\text{Li}_{4+x}\text{Ni}_{1-x}\text{WO}_6$ , where an exhaustive study of  $\text{Li}_{4.15}\text{Ni}_{0.85}\text{WO}_6$  was undertaken. This material has unique electrochemical properties due to  $\text{W}^{6+}$  and the crystal structure, giving a differential capacity that differs from other studied materials. The anionic redox of  $\text{O}^{2-}$  plays a major role, where the majority of the capacity of the material is coming from the redox processes involving the anion.

Electrochemical and structural characterisation techniques were used, with a special focus on XPS, where different electrodes charged and discharged at different voltages were studied, and the role of Ni and O in the charge compensation during electrochemical delithiation was investigated; anionic redox is observed and established. Large discharge hysteresis below 2 V is also observed.

## **5.2. Introduction**

In this chapter, a novel non-stoichiometric family of Li-rich compounds following the formula of  $\text{Li}_4\text{MM}'\text{O}_6^{1-3}$  is established. The stoichiometry for these materials are  $\text{Li}_{4+x}\text{Ni}_{1-x}\text{WO}_6$  ( $0 \leq x \leq 0.25$ ), specially focused on one stoichiometry in particular:  $\text{Li}_{4.15}\text{Ni}_{0.85}\text{WO}_6$ , which consists in a Li-rich rocksalt oxide exhibiting partial cation ordering, without fully occupied lithium layers separated of  $[\text{MO}_6]^{n-}$  octahedra and forming the honeycomb array as shown in **Figure 5.1**. The space group is  $C2/m$ .

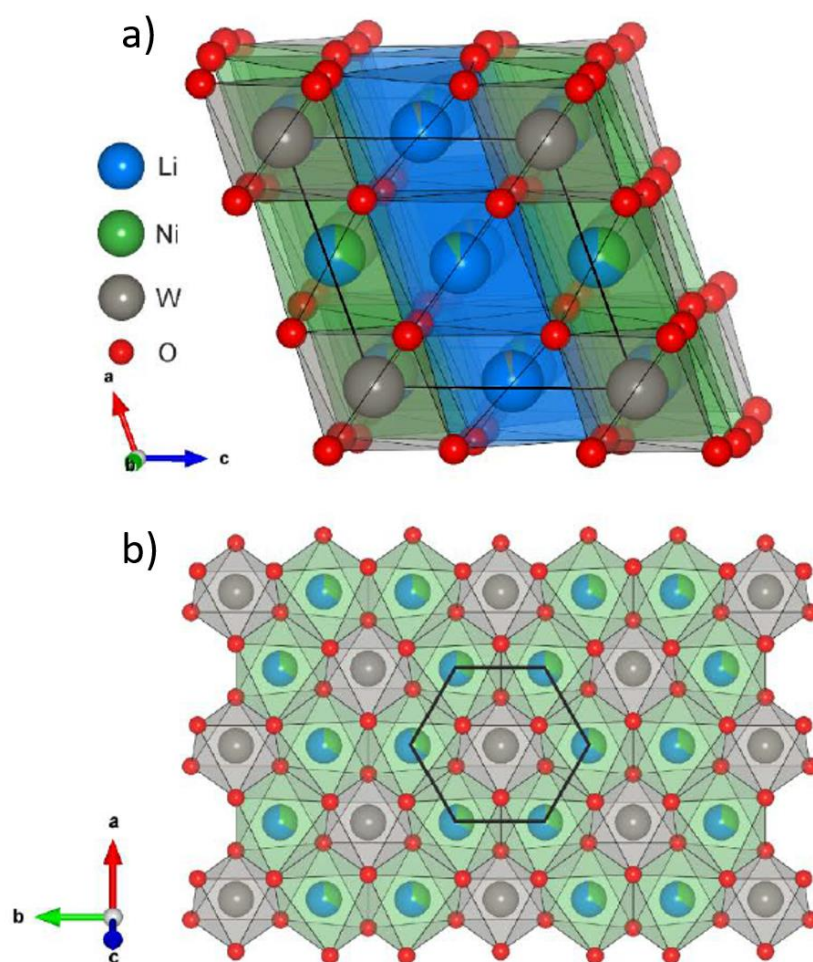


**Figure 5.1.** The rock-salt structure of  $\text{Li}_{4.15}\text{Ni}_{0.85}\text{WO}_6$  viewed along the  $[010]$  direction (a) and honeycomb-like ordering around W in the W/Ni-rich layer (b). Crystal structure simulation designed by Dr Zoe Taylor and Dr Michael Pitcher.

This novel family of Li-rich oxides derives from the  $\text{Li}_4\text{NiWO}_6$  phase reported by Mandal *et al.*<sup>4</sup> and follows early reports of a tungsten containing compound evaluated as a lithium intercalation material.  $\text{W}^{6+}$  provides electroneutrality and structural stability to the rock-salt based structure and allows the influence of a  $5d^0$  metal on the electrochemical properties according to the numerous reports of stable tungsten peroxo and superoxo species.<sup>5-8</sup> The theoretical capacity for  $\text{Li}_{4.15}\text{Ni}_{0.85}\text{WO}_6$  was calculated to be  $310 \text{ mAh g}^{-1}$  considering complete deintercalation.

### **5.3. Results**

#### **5.3.1. Electrochemical properties**

Electrochemical measurements at long cycling (C-rate of  $20 \text{ mA g}^{-1}$ ) are shown in **Figure 5.2**. The first charge / discharge cycle for this material shows a capacity of  $400 \text{ mAh g}^{-1}$  when is charged to  $5 \text{ V}$ , with some irreversible capacity on discharge to  $1 \text{ V}$  reaching up to  $200 \text{ mAh g}^{-1}$ , decreasing to  $175 \text{ mAh g}^{-1}$  after 20 cycles. Capacity fading can be observed after 25 cycles.

**Figure 5.2c.** shows the differential capacity curve at different cycles of  $\text{Li}_{4.15}\text{Ni}_{0.85}\text{WO}_6$ . The irreversible capacity on the first cycle, and subsequent modification of the capacity-voltage curve observed in **Figure 5.2d.**, indicates a change in the crystal structure upon initial charging, which could be related to a rearrangement of cations or oxygen release from the material.

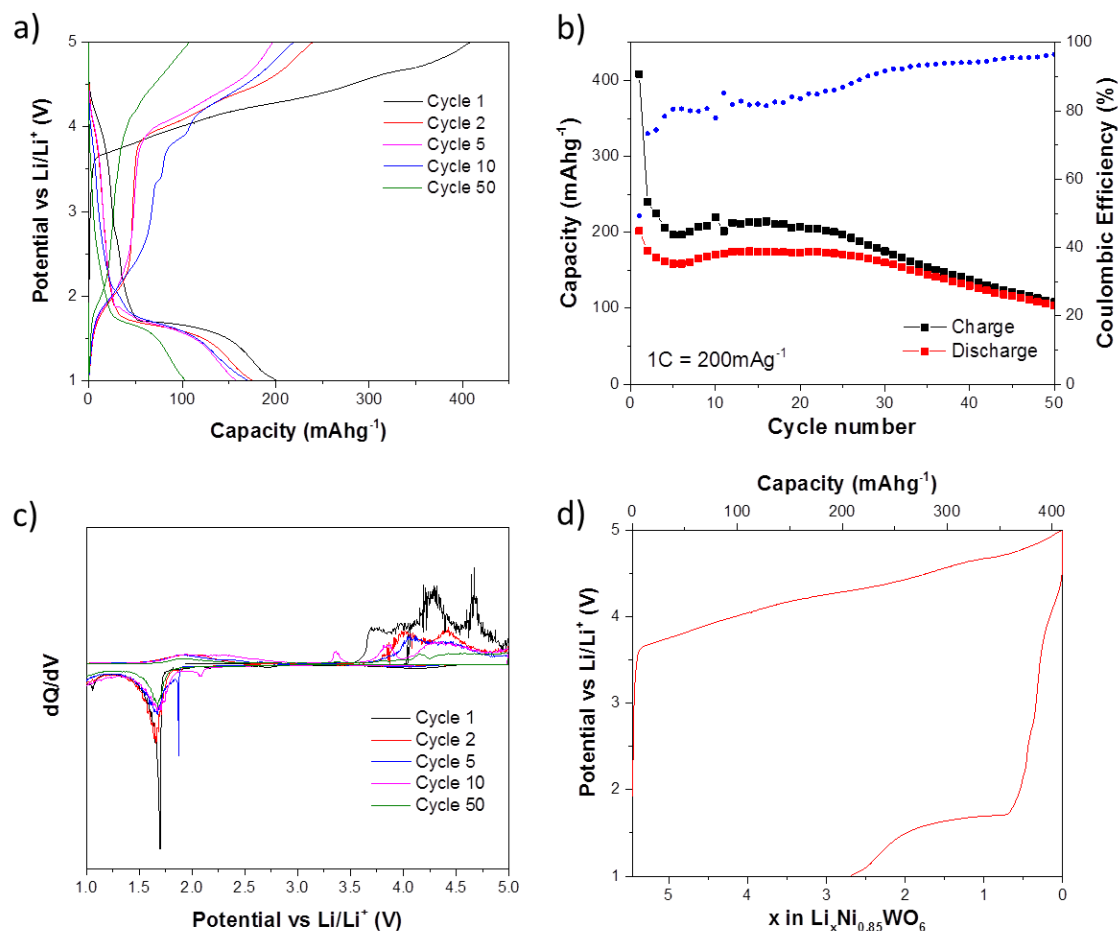


**Figure 5.2.** Electrochemical performance of  $\text{Li}_{4.15}\text{Ni}_{0.85}\text{WO}_6$  as cathode material. (a) Galvanostatic measurement at different cycles. (b) Cyclability and coulombic efficiency. (c) Differential capacity at different cycles. (d) Comparison between the first charge / discharge and the expected loss of Li atoms in the stoichiometry of the material after first discharge.

A more detailed differential capacity is shown in **Figure 5.3.**, with three redox processes occurring at 3.7, 4.2 and 4.7 V vs.  $\text{Li}/\text{Li}^+$  on the first charge, and most of the redox activity on discharge happening at 1.7 V, which is related with the plateau observed in **Figure 5.2a.** and **Figure 5.2d.** Such a large voltage hysteresis (2-3 V) is uncommon for rocksalt oxide cathode materials, and was therefore investigated further. On the

second cycle, different processes are observed, with  $\sim 0.35$   $\text{Li}^+$  deintercalated at 2 V and the remaining 2.25  $\text{Li}^+$  at 4 and 4.4 V. The strongest discharge redox peak still appears at 1.7 V.

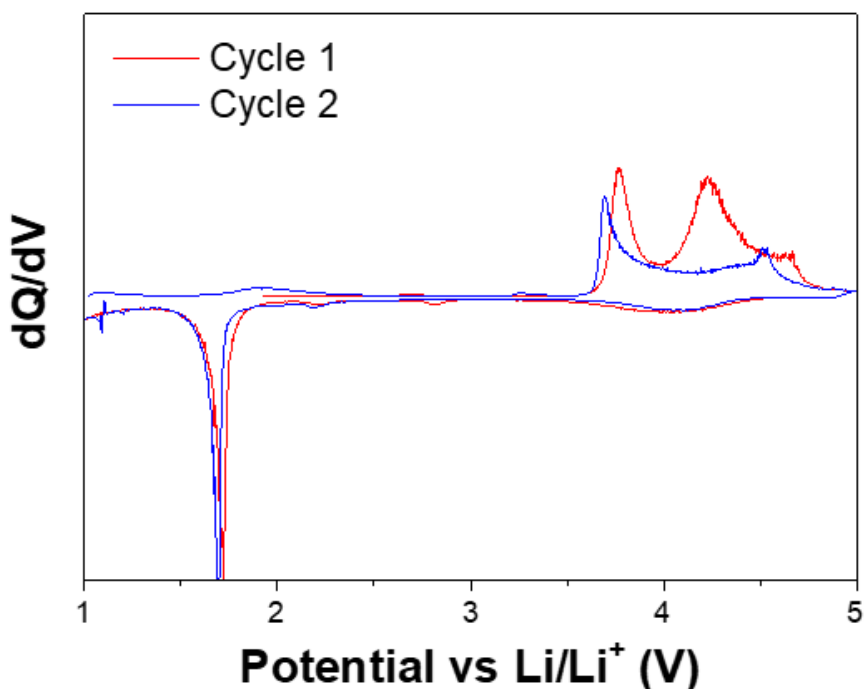


**Figure 5.3.** Differential capacity of the first two cycles and their difference in the redox processes. The difference in the redox peaks observed between both cycles is related with the change in the crystal structure that is taking place upon initial charging.

To understand the origin of the irreversibility observed in **Figure 5.2d.**, several cells were cycled with different maximum cut-off voltages, and the corresponding differential capacity curves are shown in **Figure 5.4.**

For a 4 V cut-off, less than 100 mV polarisation is observed between the oxidation and reduction processes and the capacity of  $85 \text{ mAh g}^{-1}$  is fully recovered. After charging at 4.5 V with a capacity of  $225 \text{ mAh g}^{-1}$ , several broad reduction peaks are spread between

3.4 and 4.4 V, and an intense peak appears at 1.7 V corresponding to the low voltage plateau described previously.

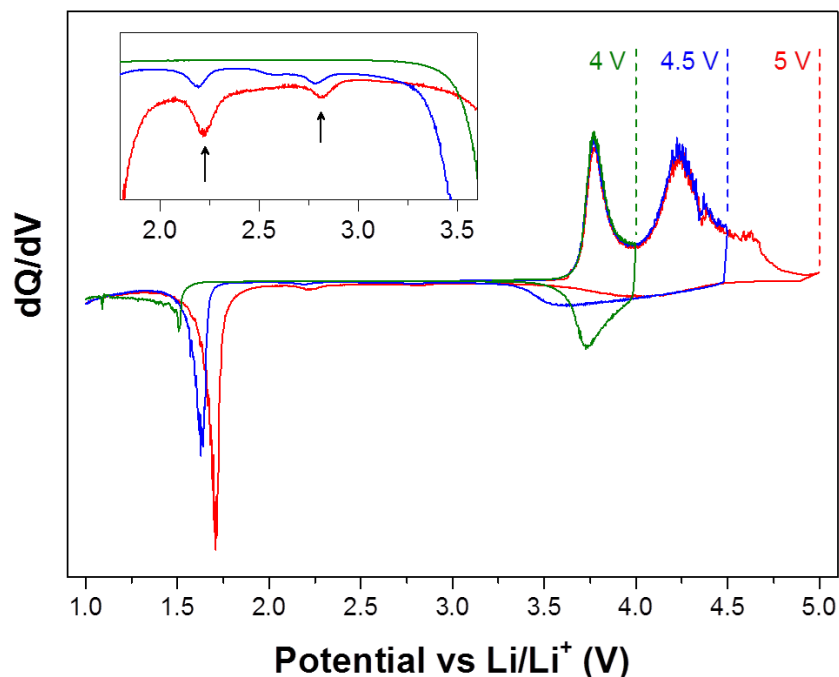


**Figure 5.4.** Differential capacity plots of the voltage window opening experiment performed on  $\text{Li}_{4.15}\text{Ni}_{0.85}\text{WO}_6$  with upper cut-off voltages of 4, 4.5 and 5 V. Two small features appearing on discharge after oxidation above 4.5 V are highlighted in the inset.

The modification is even more obvious when the material is fully charged to 5 V, with only a broad reduction feature left at 4 V and most of the capacity recovered on the 1.7 V plateau. The appearance of two small features during discharge at 2.2 and 2.8 V (see inset of **Figure 5.4.**) when the sample is charged at 4.5 V could indicate a small fraction of cations (Ni or W) in different coordination environments. Another remark is that the irreversible capacity on the first cycle is due to the redox process at 4.2 V.



### 5.3.2. Charge compensation mechanism

The oxidation states for the transition metals are calculated to be  $\text{Ni}^{2.18+}$  and  $\text{W}^{6+}$ ; that means that Ni is partially oxidised in the pristine material, and the formula can be re-written as  $\text{Li}_{4.15}\text{Ni}^{3+}_{0.15}\text{Ni}^{2+}_{0.7}\text{WO}_6$ . Considering W as redox inactive, only Ni was supposed to be oxidised in this material. Redox reaction of  $\text{Ni}^{2.18+}/\text{Ni}^{4+}$  can only participate up to  $127 \text{ mAh g}^{-1}$  and this cannot explain the high initial charge capacity ( $400 \text{ mAh g}^{-1}$ ) and reversible discharge capacity ( $200 \text{ mAh g}^{-1}$ ). To understand the role played by Ni, W and O in the different electrochemical processes, several spectroscopic techniques were used for measuring selected *ex situ* samples.

X-ray absorption near edge structure (XANES) spectroscopy was used for analysis of the nickel and tungsten oxidation states, near the Ni K- and W  $\text{L}_{\text{III}}$ -edges, as shown in **Figure 5.5**. The data was calibrated using Ni/W metal foil references and normalised with the Athena software.<sup>9</sup>

XANES measurements at W  $\text{L}_3$ -edge (**Figure 5.5a.**) shows a very slight change in shape of the absorption peak from 4 to 4.5 V that cannot be assigned to a change of oxidation state but rather to a distortion of the W local environment. This is consistent with an irreversible transformation of the material with the 4.5 V process, as the double peak initially observed seems to coalesce and remains unchanged on further cycling.

The Ni K-edge was used to probe the activity of Ni, with  $\text{NiWO}_4$  and  $\text{LiNiO}_2$  as standards for +2 and +3 oxidation states, respectively. The edge position of the pristine sample is similar to that one corresponding to the  $\text{NiWO}_4$  standard (see **Figure 5.5b.**), as it was expected from a majority of  $\text{Ni}^{2+}$  ions in the starting material.

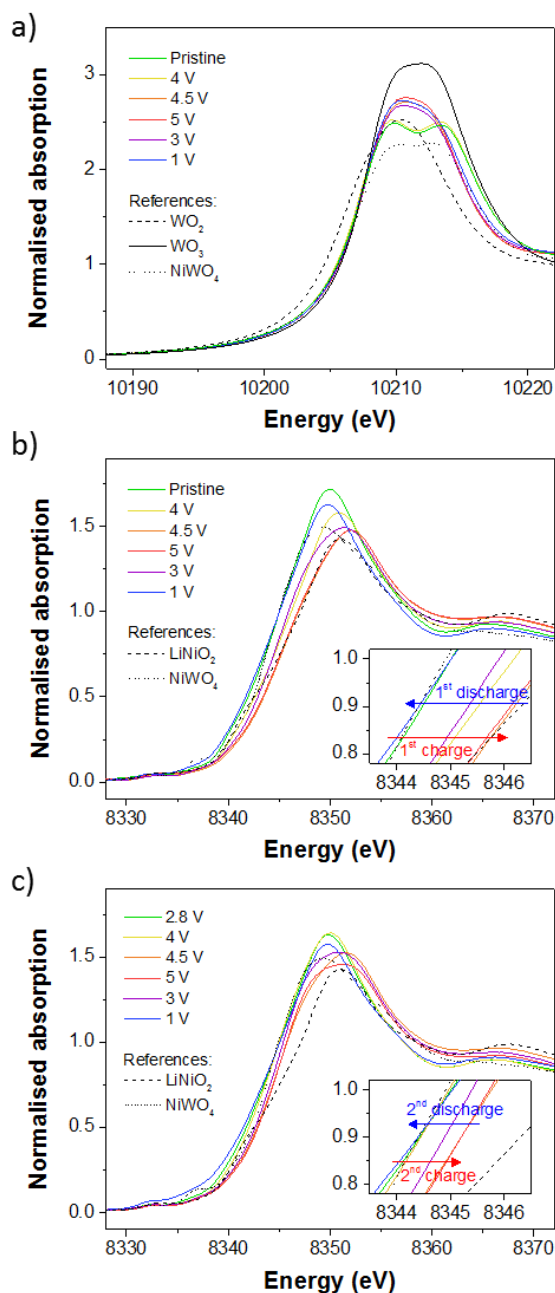


**Figure 5.5.** X-ray absorption spectroscopy data of cycled  $\text{Li}_{4.15}\text{Ni}_{0.85}\text{WO}_6$ . *Ex situ* spectra at W L<sub>3</sub>-edge on the first cycle (a) and Ni K-edge on the first (b) and second (c) cycles were measured for cycled samples at different states of charge / discharge. The spectra for  $\text{W}^{4+}\text{O}_2$ ,  $\text{W}^{6+}\text{O}_3$ ,  $\text{Ni}^{2+}\text{W}^{6+}\text{O}_4$  and  $\text{LiNi}^{3+}\text{O}_2$  are given as references. XANES measurements were carried out by Dr Zoe Taylor and Dr Michael Pitcher and analysed by Dr Arnaud Perez.

## ***Chapter 5. Electrochemical and surface behaviour of Li-rich nickel tungsten oxides***

---

Upon charging to 4 V, the edge gradually shifts to higher energies and finally reaches the edge position of the LiNiO<sub>2</sub> standard at 4.5 V, indicating oxidation of Ni<sup>2+</sup> to Ni<sup>3+</sup>. Further oxidation to 5 V does not affect the edge, which suggests that the Ni oxidation is limited to Ni<sup>3+</sup>, making Li<sub>4.15</sub>Ni<sub>0.85</sub>WO<sub>6</sub> a rare example of cathode material with the average oxidation state of nickel being considerably less than +4 after charging to 5 V. On discharge, Ni is partially reduced back to an oxidation state between Ni<sup>2+</sup> and Ni<sup>3+</sup> at 3 V, and to Ni<sup>2+</sup> when discharged to 1 V. During the second cycle, the oxidation of Ni seems to start at a higher voltage, between 4 and 4.5 V (**Figure 5.5c.**), but does not reach the full Ni<sup>3+</sup> oxidation state. This is possibly a consequence of structural reorganisation during the first cycle that leaves some Ni<sup>2+</sup> ions inactive in the material, resulting in a broadening of the Ni K-edge maximum but no clear shifts of the edge position.

According to what it is observed in XANES, only the Ni<sup>2.18+</sup>/Ni<sup>3+</sup> redox is active in the material. The specific capacity of this transition theoretically account for about 64 mAh g<sup>-1</sup> whereas the first discharge capacity reaches 200 mAh g<sup>-1</sup>, leaving two thirds of the capacity unexplained.

To investigate the possible participation of oxygen redox to the charge compensation mechanism, O 1s and W 4f XPS spectra were collected to probe the presence of oxidised oxygen species. **Figure 5.6.** compares the XPS results for these spectra at different voltages for the first and second cycle.

Charge correction was done using O 1s, implementing the strongest component after deconvolution at 530.6 eV, which corresponds to the non-oxidised O<sup>2-</sup> (blue colour). The oxidised O<sup>n-</sup> (0 ≤ n ≤ 2) at 532.2 eV is shown in red colour. Other contributions for these peaks are the surface deposits from decompositions products of the carbonate-based

## ***Chapter 5. Electrochemical and surface behaviour of Li-rich nickel tungsten oxides***

---

electrolyte and the CEI layer at ~534 eV (orange colour) and a small contribution at lower binding energy (~529 eV) attributed to an oxygen environment rich in nickel (green).<sup>10</sup>

Between the uncharged material and up to 4.5 V, the spectra are dominated by the signal of oxygen O<sup>2-</sup> and shows little variation, with only weak contributions of oxidised O<sup>n-</sup> at higher binding energy (appearing at 4 V) and environment rich in nickel at lower. When the sample is fully charged at 5 V, the contribution of oxidised O<sup>n-</sup> significantly increases; other contributions arising from deposited species are also very intense for this sample, as it is expected to have some electrolyte decomposition at the cathode surface at high voltage. Upon discharge, the relative intensity of the O<sup>n-</sup> peak decreases compared to that of the O<sup>2-</sup> one but does not fully disappear, suggesting that some of the O<sup>n-</sup> species formed are not reduced back to oxide. On the second cycle, the contribution at 532.2 eV increases again at 4.5 V, a lower voltage compared to the first cycle. The small contribution coming from the environment rich in nickel disappears at high voltages and appears when is fully discharged; the disappearance of this contribution with the increase O<sup>n-</sup> species suggests that this environment is independent of the oxidation state of Ni and only depends of the presence of O<sup>n-</sup> species.

The same observations can be made from monitoring the W 4f doublet position, which is very sensitive to changes in local environment of W ions. The doublet shown in blue (4f<sub>7/2</sub>) and cyan (4f<sub>5/2</sub>) for the contribution with non-oxidised oxygen environment and in red (4f<sub>7/2</sub>) and pink (4f<sub>5/2</sub>) for the contribution with oxidised O<sup>n-</sup>. At 5 V, the doublet shifts to higher binding energy suggesting an increase of ionicity of W-O bonds with decreasing Li content, and a new doublet appears, whose evolution closely follows that of the O<sup>n-</sup> peak on the O 1s spectra. This new doublet is therefore assigned to a new W

environment coordinated by the oxidised  $O^{n-}$  species, and its relative intensity is correlated with the amount of oxidised oxygen next to the surface of the sample.

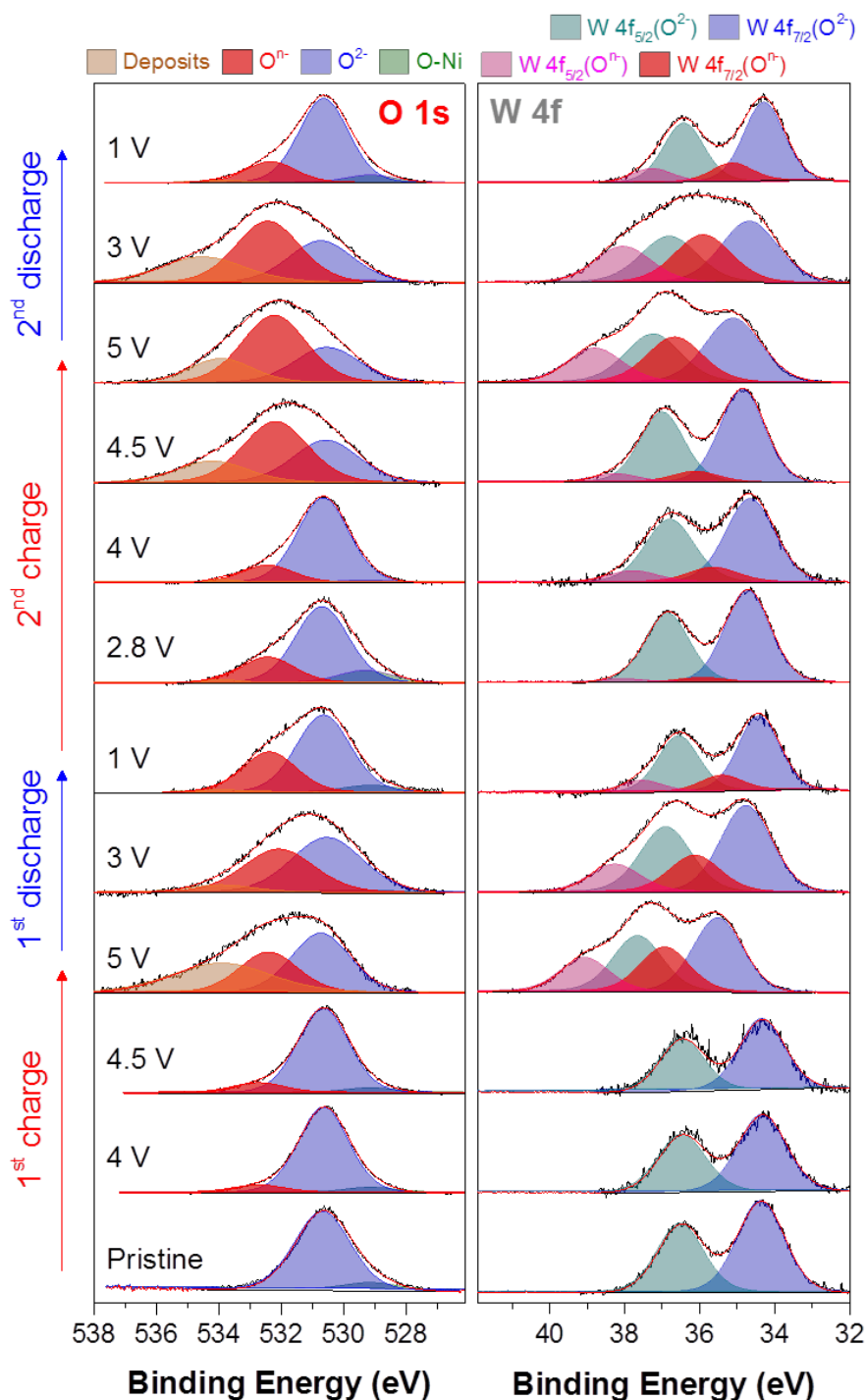


**Figure 5.6.** X-ray photoemission spectroscopy data collected at O 1s and W 4f energies on the first two charge / discharge cycles of  $Li_{4.15}Ni_{0.85}WO_6$ .

## Chapter 5. Electrochemical and surface behaviour of Li-rich nickel tungsten oxides

In order to support this assignment, the measurement of the XPS spectra of two reference samples with  $W^{6+}$  cations in different coordination environments, namely  $WO_3$  and  $WO_2(O_2)H_2O$  (which contains a peroxo  $(O_2)^{2-}$  ligand),<sup>11</sup> were done (**Figure 5.7**). The position of the O 1s peak (530.7 eV) and W 4f doublet (35.9-38.0 eV) of  $WO_3$  are in good agreement with the corresponding  $O^{2-}$  (530.6 eV) and W- $(O^{2-})$  (35.5-37.6 eV) peaks of the fully charged sample, whereas the position of the O 1s peak (532.7 eV) and W 4f doublet (36.9-39.0 eV) of  $WO_2(O_2)H_2O$  correspond to the  $O^{n-}$  (532.2 eV) and W- $(O^{n-})$  (36.9-39.0 eV) peaks in the fully charged sample. The charge correction was done with C 1s (graphitic carbon at 284.6 eV).

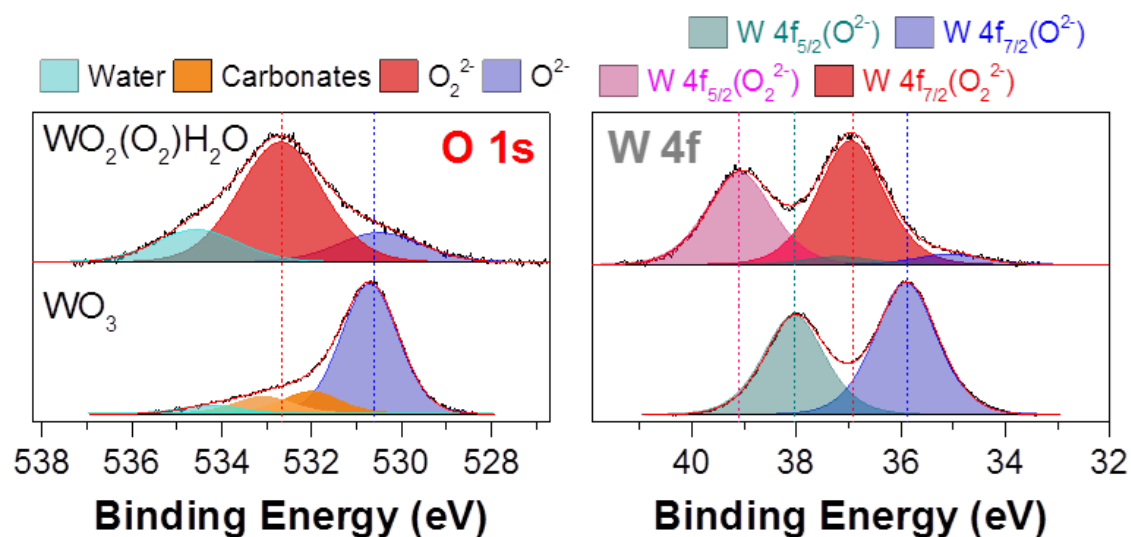


**Figure 5.7.** O 1s and W 4f X-ray photoemission spectroscopy data collected on standard W compounds. In the O 1s spectra, the contributions of  $O^{2-}$  and  $O^{n-}$  (or  $(O_2)^{2-}$  for  $WO_2(O_2)H_2O$ ) are shown in blue and red, respectively. Some contribution of water is also shown in cyan for  $WO_2(O_2)H_2O$ .

Finally, the splitting of both W-(O<sup>2-</sup>) and W-(O<sup>n-</sup>) doublets remains constant at any state of charge (2.14 eV), confirming that W has an oxidation state of +6 at all points along the charge / discharge curves.

**Figure 5.8.** shows the evolution of oxidised O<sup>n-</sup> in the first two cycles, as well as the change in oxidation state for O and Ni. The calculation of the oxidation state for Ni was made with the doublet separation of Ni 2p, and its evolution coincides with what was observed in XANES. The higher oxidation state for both O and Ni observed in the discharge of the second cycle is to charge compensate the Li loss.

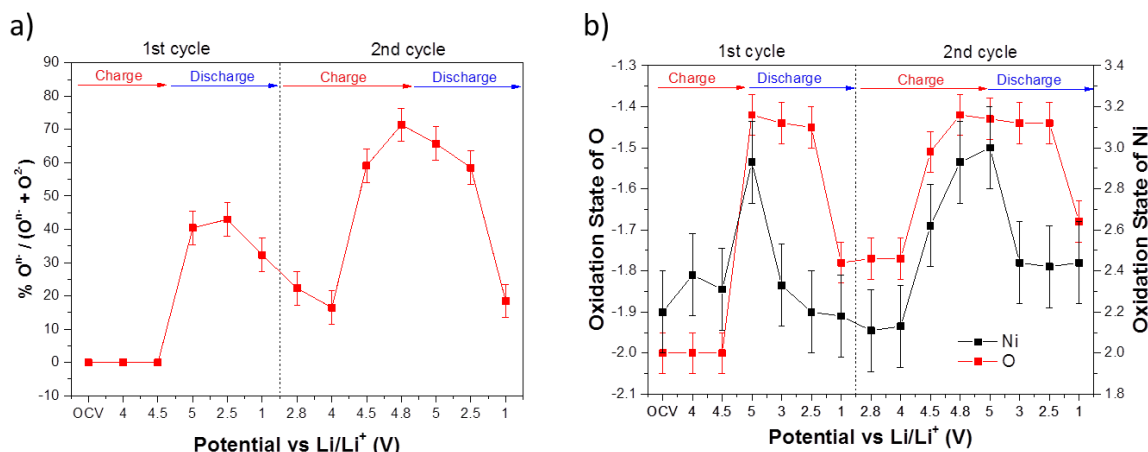


**Figure 5.8.** Evolution of oxidised oxygen O<sup>n-</sup> (a) and oxidation state for the redox active centres (b) on the first two charge / discharge cycles of  $\text{Li}_{4.15}\text{Ni}_{0.85}\text{WO}_6$ .

The possible explanation of why most oxidised oxygen species appears above 4.5 V on the first charge (and the subsequent difficulty to understand the charge compensation mechanism between OCV and 4.5 V) is that XPS, which is a surface sensitive technique, cannot detect the oxygen oxidised close to the surface if it evolves as oxygen gas. It is possible that oxygen is oxidised at lower potential in the bulk of the material, according

## ***Chapter 5. Electrochemical and surface behaviour of Li-rich nickel tungsten oxides***

---

to the low intensity contribution in the 4 and 4.5 V samples and further studies have to be done to understand what is happening in the bulk of the material.

In order to observe the evolution of oxygen in the bulk and to reproduce the obtained XPS results for O 1s and W 4f at different stages of charge and discharge during the first two cycles, HAXPES measurements were carried out in Diamond Light Source synchrotron. The energy of the beam was 2.1 and 6.45 keV.

The cathodic electrodes were prepared by Dr Arnaud Perez as mix of active material / Super C carbon / Polytetrafluoroethylene (PTFE) binder (85:10:5 by wt) and they were free-standing (the aluminium current collector was not used).

The measurement of the whole region gave place to the observation of the main core peaks of each material that form part of the composition of the electrodes, but also some contamination is observed in most of the analysed samples, mainly copper (with an  $E_B$  for Cu 2p<sub>3/2</sub> of ~933 eV) from the sample plate, but also some other elements such as Au and Ag were observed. The reason of this contamination remains unclear, but could occur during the transportation and/or manipulation of the samples inside glovebox or the HAXPES machine. An example of this contamination can be observed in **Figure 5.9a.**, where an example of measured electrodes (pristine electrode, fully charged at 5 V and fully discharged at 1 V during first cycle, respectively) are represented for HAXPES measurements with a beam energy of 2.1 keV, and the contamination peaks are observed; the Cu 2p peak observed in the electrode fully charged at 5V is the most intense and it is observed in the most of the analysed samples.



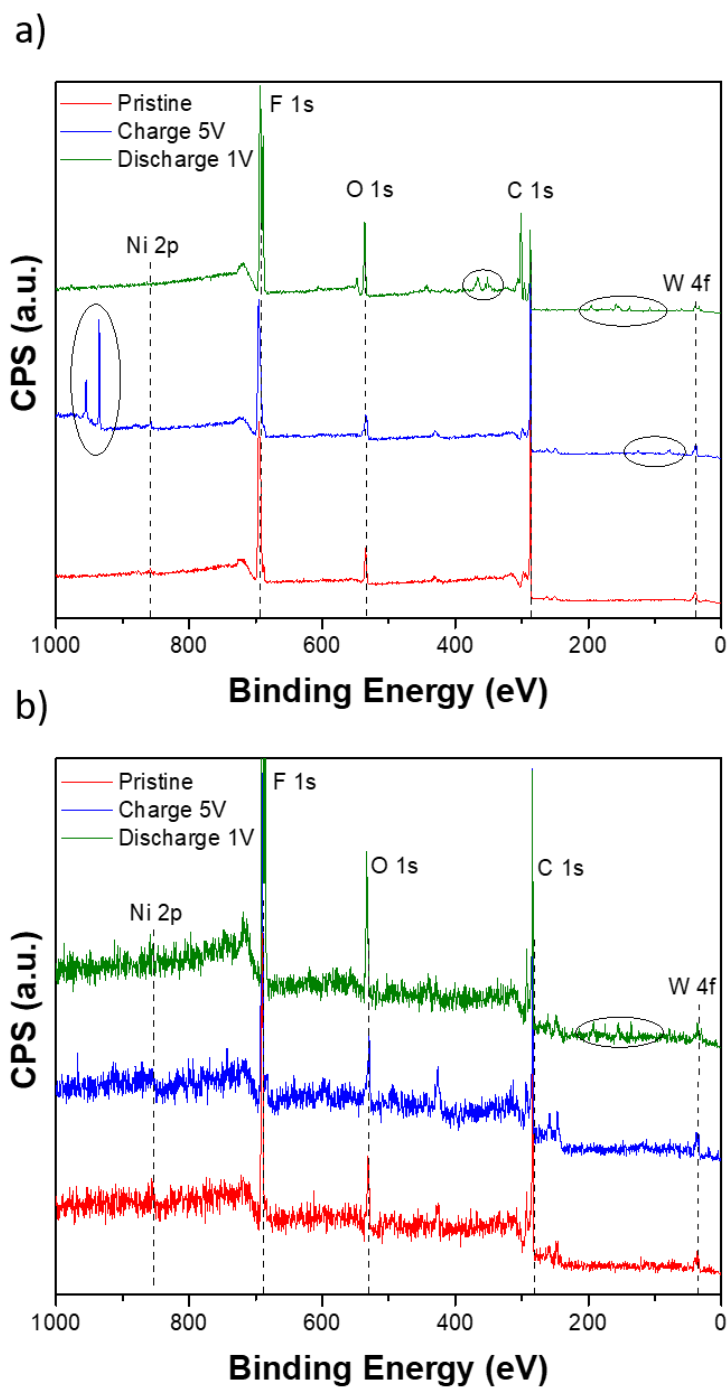


**Figure 5.9.** Survey spectra of HAXPES measurements at (a) 2.1 keV and (b) 6.45 keV for the pristine electrode and the electrodes fully charged at 5 V and fully discharged at 1 V during the first cycle. Ni 2p, F 1s, O 1s, C 1s and W 4f peaks are observed, but also some impurities were measured as circled and assigned as Cu, Ag and Au.

## ***Chapter 5. Electrochemical and surface behaviour of Li-rich nickel tungsten oxides***

---

In **Figure 5.9b.**, HAXPES measurements for a 6.45 keV beam energy for the same electrodes are represented. The signal for these spectra presents more noise compared with those coming from the 2.1 keV energy, but it is possible to distinguish the main core peaks of the different elements and additional peaks at ~250 and ~430 eV that correspond to W 4d and W 4p, respectively. These peaks from tungsten can barely be observed in soft XPS, which demonstrates the importance in the use of high energy to produce the photoemission of core electrons from orbitals of more difficult accessibility with the traditional Mg and Al anode sources.<sup>12-14</sup>

The absence of other peaks in the most of the samples suggests that the contamination does not reach the bulk, but some small peaks that could be observed (like in the region at ~150 eV in the electrode fully discharged at 1 V in **Figure 5.9b.**) remain unexplained.

Taking a look more in depth for the electrode fully discharged at 1 V in both energies, it is observed a variation in the F 1s peak, where the singlet is now a doublet, and the contribution of the C-F component in the C 1s increases significantly. This could mean that there is a change in the environment of PTFE binder during the discharge.

A detailed analysis of O 1s and W 4f were done in HAXPES in order to compare with the obtained results in XPS. In **Figure 5.10.**, the results for O 1s using energies of 2.1 and 6.45 keV are shown. An important contribution is observed at ~529 eV in both energies: in the case of the measurements using an energy of 6.45 keV, it is attributed to an oxygen environment rich in nickel; for the measurements with 2.1 keV, where the contamination with Cu was significant in most of the samples, this peak is a combination of Cu-O and Ni-O bond because both appear at the same  $E_B$ .

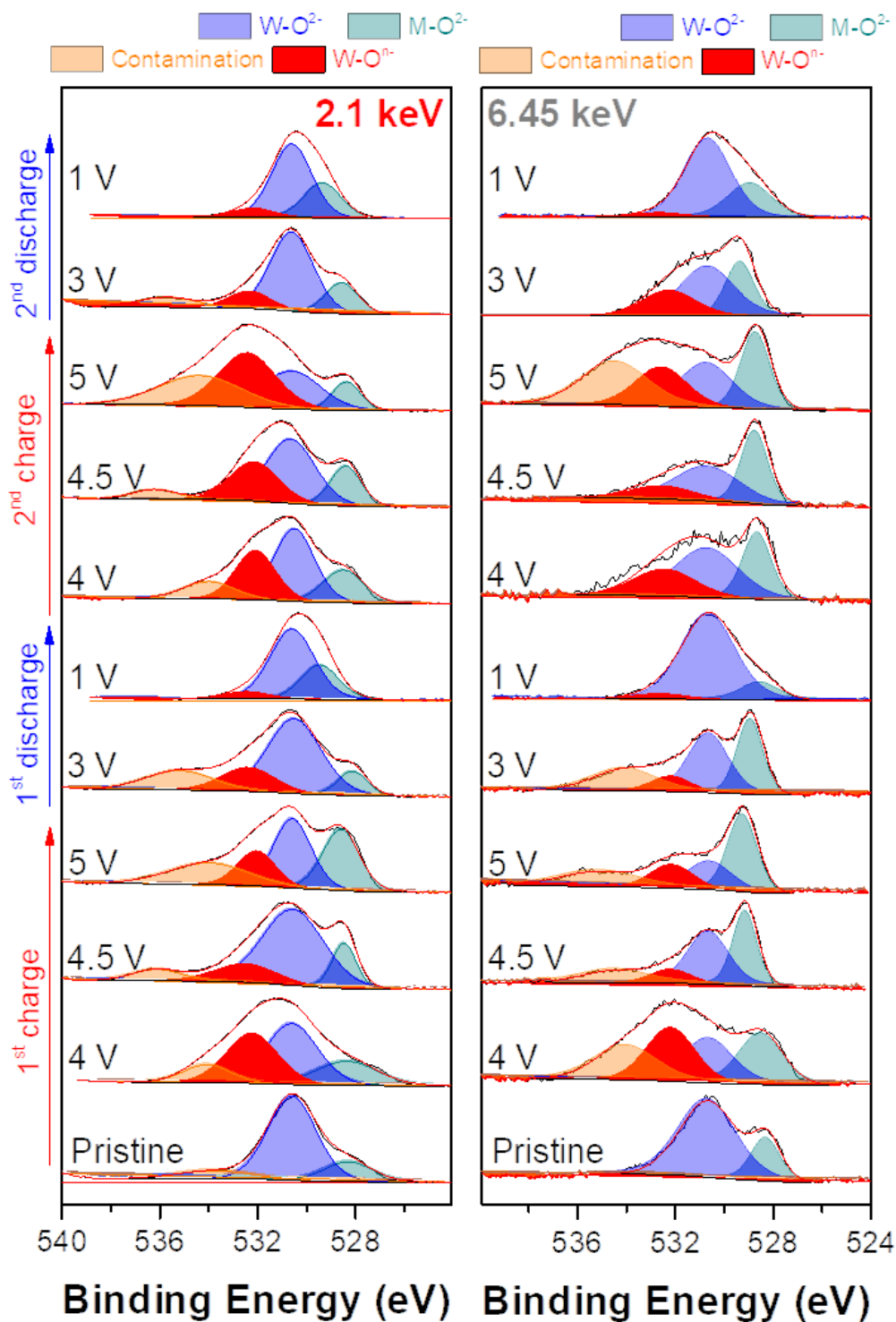


**Figure 5.10.** HAXPES data collected for O 1s using an energy of 2.1 keV and 6.45 keV on the first two charge / discharge cycles of  $\text{Li}_{4.15}\text{Ni}_{0.85}\text{WO}_6$ .

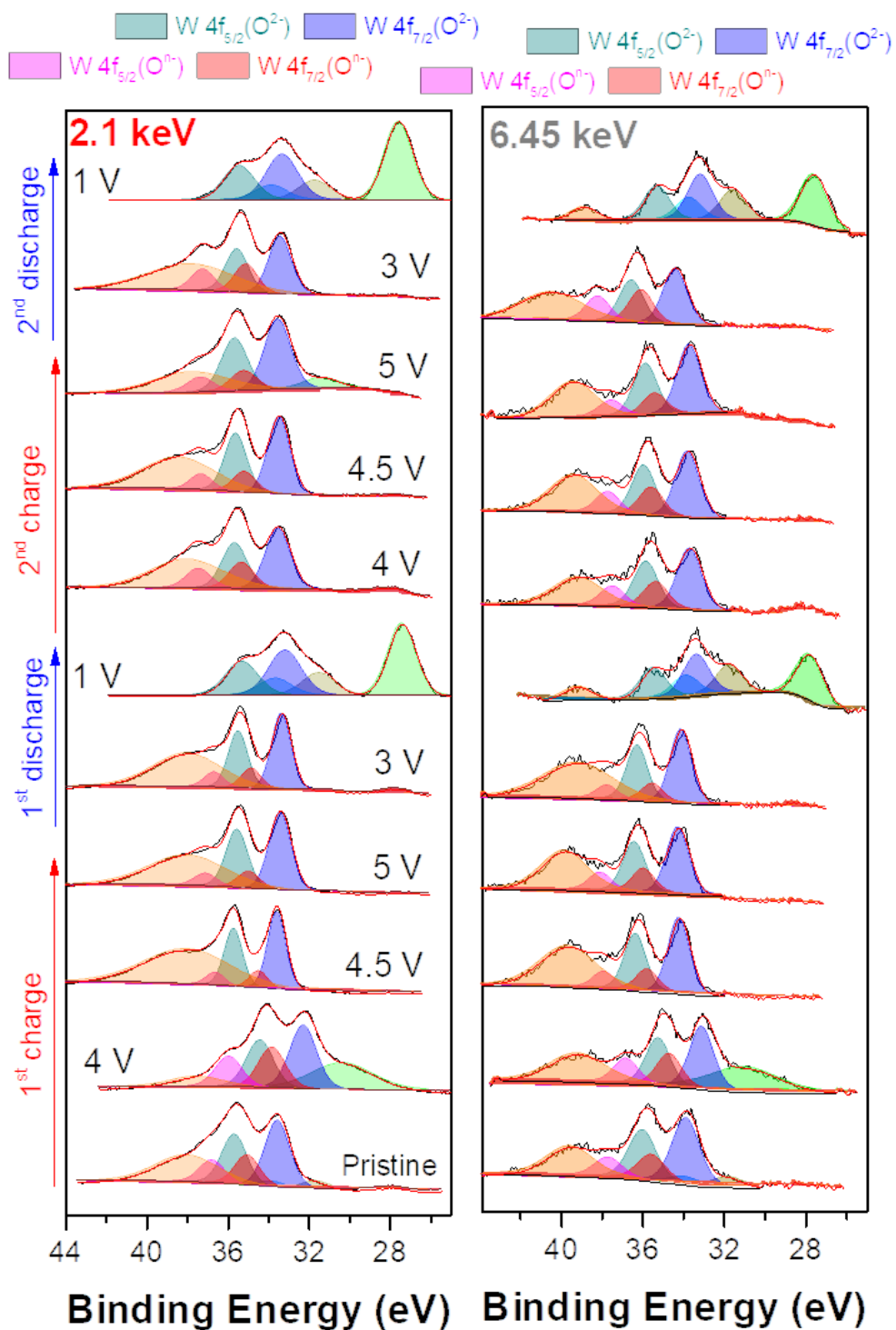


**Figure 5.11.** HAXPES data collected for W 4f using an energy of (a) 2.1 keV and (b) 6.45 keV on the first two charge / discharge cycles of Li<sub>4.15</sub>Ni<sub>0.85</sub>WO<sub>6</sub>. The contribution of F 2s and W 5p<sub>3/2</sub> can be appreciated in the spectra.

The contributions of non-oxidised  $O^{2-}$  and oxidised  $O^{n-}$  appear at 530.6 and 532.2 eV, respectively, the same  $E_B$  as observed in XPS. Non-oxidised  $O^{2-}$  and oxidised  $O^{n-}$  are shown in blue and red, respectively. Other contributions for these peaks appearing at ~534 eV (orange colour) are attributed to the presence of other oxides and hydroxides such as  $Cu(OH)_2$ .

The formation of oxidised  $O^{n-}$  in both energies follows a similar behaviour than observed in XPS except for the electrode charged at 4V, that differs from the XPS spectra, obtaining unexpected high values for oxidised  $O^{n-}$ . The most important difference regarding XPS is observed in the contribution at ~529 eV, above all with the use of 6.45 keV, where the peak increases in intensity.

**Figure 5.11.** shows the W 4f doublet position for both energies, and once again these results are comparable with those obtained in XPS. The doublet shown in blue ( $4f_{7/2}$ ) and cyan ( $4f_{5/2}$ ) (33.5-35.6 eV) corresponds to the contribution with non-oxidised oxygen  $O^{2-}$  environment and the doublet in red ( $4f_{7/2}$ ) and pink ( $4f_{5/2}$ ) (34.5-36.6 eV) is the contribution with oxidised oxygen  $O^{n-}$ . An important contribution observed in almost all the samples appears at ~39 eV (orange colour) and it is attributed to W  $5p_{3/2}$  (appearing in these measurements due to a different emission angle and cross section<sup>15, 16</sup> than used in XPS). Additional peaks are also observed, such as a doublet at lower  $E_B$  (32-34.1 eV) in the electrodes discharged at 1 V (first and second cycle) due to a different environment in these samples, and a green peak at ~28 eV attributed to F 2s can be also appreciated in these electrodes but also in the electrode charged at 4 V (1<sup>st</sup> cycle) and charge at 5 V (2<sup>nd</sup> cycle). The shift in position that was observed in XPS is barely significant in the measured HAXPES samples.

## Chapter 5. Electrochemical and surface behaviour of Li-rich nickel tungsten oxides

In **Figure 5.12.** the evolution of oxidised oxygen and the oxidation states for the used photon energies are observed. If these results are compared with those obtained for soft XPS (**Figure 5.8.**), and leaving apart the errors obtained in the measurement due to the contamination of the samples, the results follow a similar pattern, demonstrating that oxidised  $O^{n-}$  is also formed in the bulk of  $Li_{4.15}Ni_{0.85}WO_6$ . The fact that the sample charged at 4 V has those higher values for oxygen (and also a different shape in O 1s and W 4f spectra) could be related with a bad labelling during the handling in HAXPES measurements and that sample may be indeed the one that correspond at 5 V.

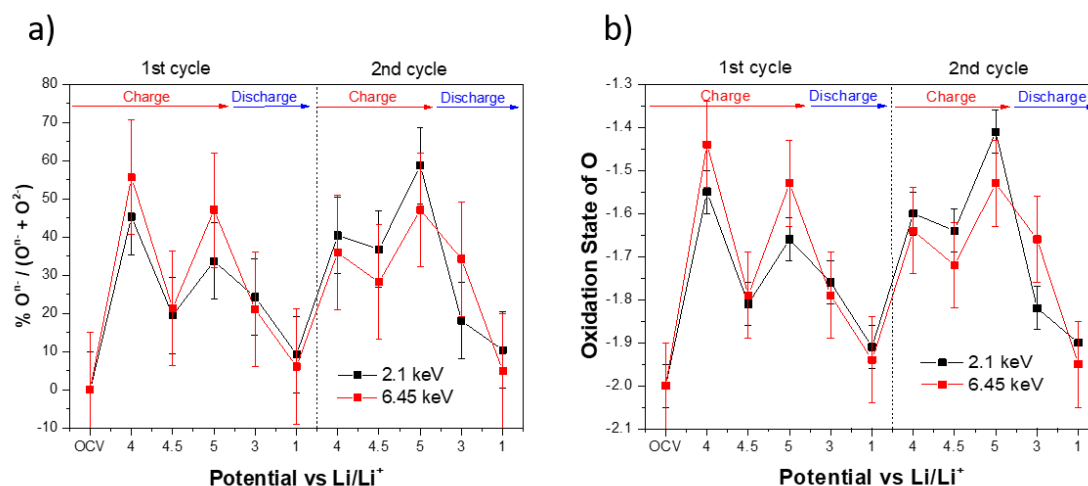


**Figure 5.12.** Evolution of oxidised oxygen  $O^{n-}$  (a) and oxidation state of oxygen (b) on the first two charge / discharge cycles of  $Li_{4.15}Ni_{0.85}WO_6$  using energies of 2.1 and 6.45 keV.

Additional HAXPES measurements were done previously to the presented one in beamline P09 of PETRAIII (Hamburg, Germany). Due to problems of handling and transportation, the analysis of these samples showed more problems of contamination than those measured in Diamond Light Source. Furthermore, the poor signal and the strong W  $5p_{3/2}$  peak due to the used emission angle and cross section<sup>15, 16</sup> causing that the

W 4f was not possible to observe and therefore to analyse, leaving O 1s the only peak with a successful signal to obtain reliable results as shown in **Figure 5.13**.

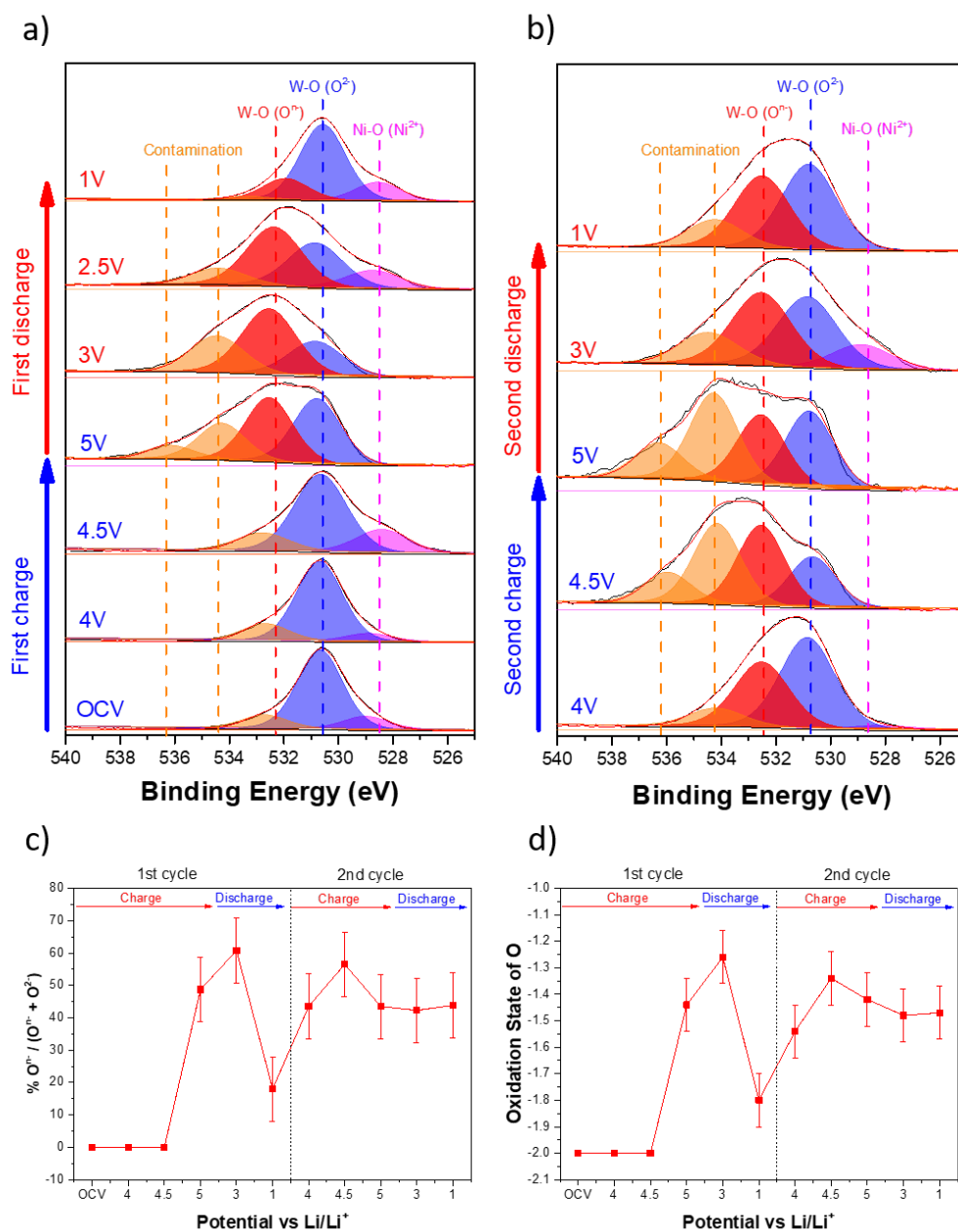


**Figure 5.13.** HAXPES data collected for O 1s for (a) first and (b) second cycle and the evolution of oxidised oxygen  $O^{n-}$  (c) and oxidation state of oxygen (d) on the first two charge / discharge cycles of  $Li_{4.15}Ni_{0.85}WO_6$  in beamline P09 of PETRAIII (Hamburg, Germany) with a photon energy of 5947.9 eV.

The evolution of oxidised oxygen and the overall oxidation state of oxygen is also shown, following a similar pattern as shown in previous data for soft XPS and HAXPES.

### **5.3.3. Formation of stable O-O bonds**

After measurements carried out via XANES, XPS and HAXPES, it is possible to confirm at this point that the high reversible capacity of  $\text{Li}_{4.15}\text{Ni}_{0.85}\text{WO}_6$  (200mAh  $\text{g}^{-1}$  on first cycle) can be explained by anionic redox despite the low participation of Ni to the charge compensation mechanism. The low voltage of the reduction plateau at 1.7 V confirms the difficulty to reduce back the oxidised  $\text{O}^{\cdot-}$  species formed during charge.

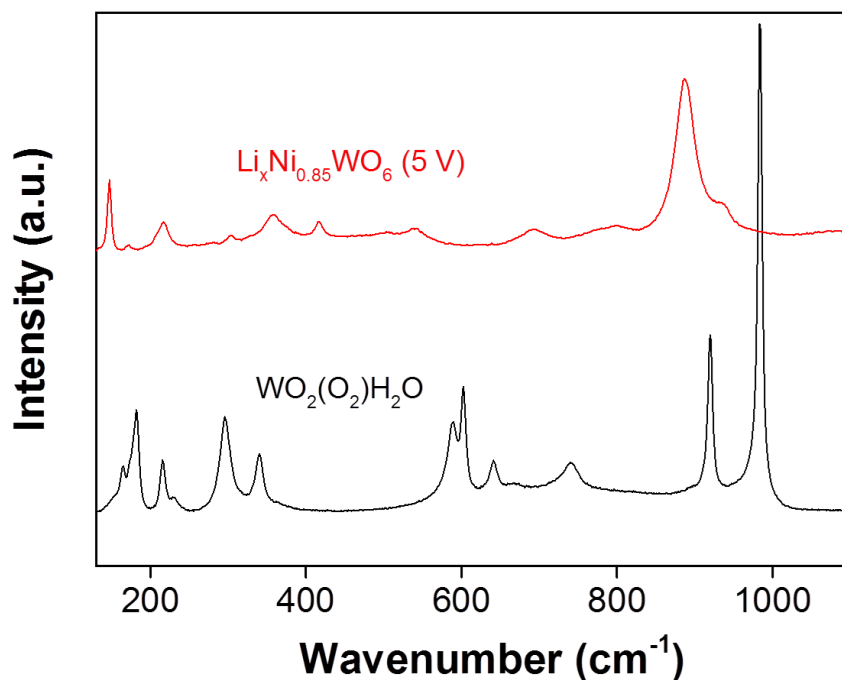


**Figure 5.14.** Experimental Raman spectra of  $\text{WO}_2(\text{O}_2)\text{H}_2\text{O}$  (black) and its comparison with  $\text{Li}_{4.15}\text{Ni}_{0.85}\text{WO}_6$  charged at 5V (red). Raman measurements were carried out and analysed by Dr Filipe Braga.



$W^{6+}$  can stabilise peroxo  $(O_2)^{2-}$  ligands in aqueous media through the formation of coordination complexes due to its  $d^0$  electronic configuration and associated  $\pi$  acceptor character.<sup>17</sup>  $WO_2(O_2)H_2O$  is a good example of this property, and shows clear signature peaks between 900 and 1000  $cm^{-1}$  in both infrared<sup>11</sup> and Raman spectroscopies as can be observed in **Figure 5.14**.

The most intense peak at 983  $cm^{-1}$  is generally assigned to the short W-O bond stretching mode,<sup>18</sup> and the less intense peak at 920  $cm^{-1}$  to the stretching of peroxo O-O bond. To check the formation of O-O bonds in the bulk structure of  $Li_{4.15-x}Ni_{0.85}WO_6$ , *ex situ* Raman spectra of samples at different states of charge and discharge were measured, and the results are shown in **Figure 5.15**.

The pristine material has one main broad Raman band at 810  $cm^{-1}$  corresponding to the W-O stretching mode and less intense peaks (327, 460, 515  $cm^{-1}$ ) at lower shifts where could correspond to bending / deformation modes. Upon charging to 4 V, the intensity of the main peak decreases and a sharper peak appears at 930  $cm^{-1}$ , joined by a second peak at 910  $cm^{-1}$  at 4.5 V. Finally, the fully charged sample (5 V) shows a very well-defined Raman spectrum, with relatively sharp and intense peaks, suggesting that the local structure of the fully charged sample is fairly ordered.

Focusing on the peaks in the 800-1000  $cm^{-1}$  region in the fully charged sample, there is a very intense peak at 890  $cm^{-1}$  and a second peak at 930  $cm^{-1}$  that appears as a shoulder. While the presence of the peak at 930  $cm^{-1}$  remains in all subsequent spectra, including the fully discharged samples, the most intense band at 890  $cm^{-1}$  progressively disappears again upon discharge and is replaced at 1 V by a broader band centred at 830  $cm^{-1}$ . On the second cycle, a perfectly reversible peak evolution is observed, consistent with the improved reversibility on subsequent cycles. The position of the peak at 930  $cm^{-1}$  is in

## Chapter 5. Electrochemical and surface behaviour of Li-rich nickel tungsten oxides

good agreement with that at  $920\text{ cm}^{-1}$  in  $\text{WO}_2(\text{O}_2)\text{H}_2\text{O}$  (Figure 5.14.), and can be assigned as the formation of an O-O peroxy bond.

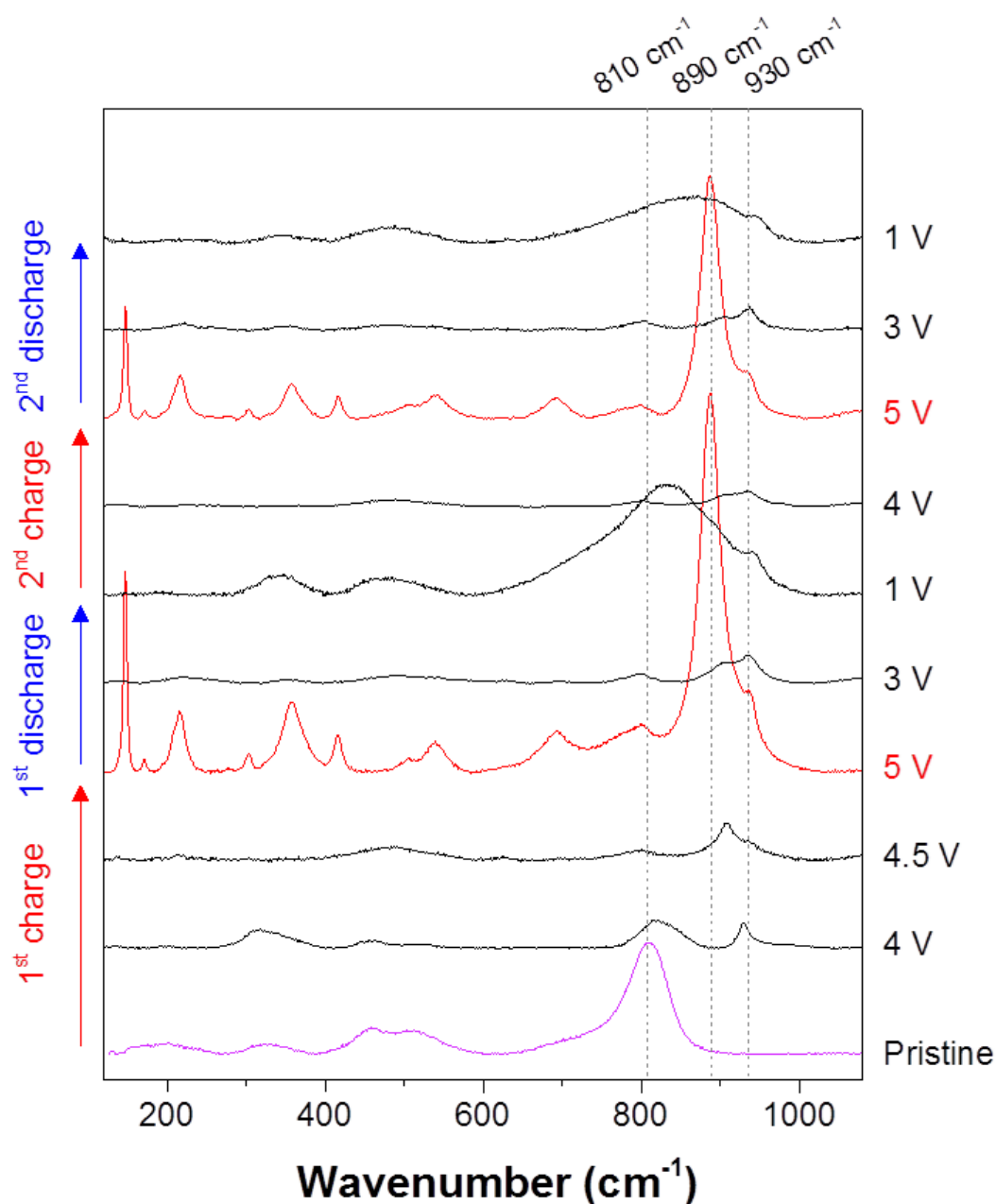


**Figure 5.15.** *Ex situ* Raman spectra for different states of charge / discharge of  $\text{Li}_{4.15}\text{Ni}_{0.85}\text{WO}_6$ . The pristine and fully charged spectra are highlighted in light purple and red, respectively. Raman measurements were carried out and analysed by Dr Filipe Braga.

The comparison with the hydrated tungsten peroxide  $\text{WO}_2(\text{O}_2)\text{H}_2\text{O}$  provide strong evidence for the formation of peroxo bonds upon full charge of  $\text{Li}_{4.15}\text{Ni}_{0.85}\text{WO}_6$ .<sup>19</sup> It is consistent with the information obtained from XPS and HAXPES, confirming that the oxidation of oxygen is not only happening at the surface, but also is a bulk effect. Finally, the fact that the peak at  $930\text{ cm}^{-1}$  does not completely disappear at the end of the first cycle is also consistent with the XPS data and indicates that some peroxo species are formed irreversibly and maintained through subsequent cycling, thus explaining some of the irreversible capacity of the first cycle.

## **5.4. Discussion**

The combination of different techniques helped us to obtain some insights in the electrochemical behaviour of  $\text{Li}_{4.15}\text{Ni}_{0.85}\text{WO}_6$ . Maybe the most important result is the impossibility to access the  $\text{Ni}^{3+/4+}$  redox, which suggests a tight competition between the redox activities of Ni and O. According to density functional theory (DFT) calculations used to investigate the electronic structure of this material, the computed voltage for  $x = 1$  in  $\text{Li}_{4-x}\text{NiWO}_6$  is found 0.2-0.4 V higher for the anionic redox compared to the cationic  $\text{Ni}^{2+/3+}$  model.<sup>19, 20</sup> This is consistent with Ni oxidation at 3.7 V observed in both XANES and XPS, and points the small difference in energy between cationic and anionic redox in this material. As no change in the oxidation state of Ni beyond +3 is observed experimentally and irreversibility increases when charging above 4 V, the material undergoes some irreversible oxidation of oxygen and gas release from the surface, corresponding to the process at 4.2 V on the first charge. This would explain that oxidised oxygen species are not observed via *ex situ* XPS in samples until 5 V. Nevertheless, the reversible formation of peroxo  $(\text{O}_2)^{2-}$  species on the second cycle, measured by Raman,

## ***Chapter 5. Electrochemical and surface behaviour of Li-rich nickel tungsten oxides***

---

XPS and HAXPES, proves that the large reversible capacity on discharge (200 mAh g<sup>-1</sup>) is due to both cationic and anionic redox, which the last one contributing to at least 2/3 of this capacity. Assuming that the Ni<sup>2.18+</sup>/Ni<sup>3+</sup> redox is fully used, 1.75 e<sup>-</sup> are to be accounted for by oxygen, i.e. 0.29 e<sup>-</sup>/O after normalizing by the number of oxygen in the formula unit, which is slightly higher than Li<sub>1.2</sub>Ni<sub>0.13</sub>Mn<sub>0.56</sub>Co<sub>0.13</sub>O<sub>2</sub> (0.25 e<sup>-</sup>/O) according to Luo *et al.*<sup>21</sup> Thereby reflecting the possibility of attaining considerable reversible anionic redox capacity from localised O-O bond formation.

About the large voltage hysteresis observed upon activation of oxygen redox, it should be pointed that this is a true concern for the development of Li-rich cathode materials,<sup>21-23</sup> as it results in a large penalty on the round-trip energy efficiency (< 90% for Li<sub>1.2</sub>Ni<sub>0.13</sub>Mn<sub>0.56</sub>Co<sub>0.13</sub>O<sub>2</sub>). Such hysteresis has been correlated with oxygen redox activity and cationic migrations,<sup>23-25</sup> with both resulting in different thermodynamic pathways on charge and discharge.

The use of high-valence d<sup>0</sup> cations to increase the lithium content leads to higher capacities, thanks to the combined participation of cationic and anionic redox. However, high-valence d<sup>0</sup> cations also stabilise the formation of O-O bonds with a bond order *n* close to 1, compared to open shell transition metals and main group elements, resulting in a large energy penalty to break the bonds upon reduction. The empty antibonding (σ\*) states of quasi molecular (O<sub>2</sub>)<sup>2-</sup> species are difficult to reduce back, as they lie well above the Fermi level.<sup>19</sup> Such reduction is possible in Li<sub>4.15</sub>Ni<sub>0.85</sub>WO<sub>6</sub>, at a very low discharge voltage of 1.7 V that makes the energy efficiency drop dramatically to 50%.

## **5.5. Conclusions**

In this work, the structural and electrochemical properties of  $\text{Li}_{4.15}\text{Ni}_{0.85}\text{WO}_6$  were explored. The fact that Ni could not be oxidised beyond  $\text{Ni}^{3+}$  even at high voltage (5 V) leaves the large reversible capacity mostly unexplained by a classical cationic redox mechanism. The capacity associated with oxygen redox in this material is thus considerably larger than that obtained with the oxidation of the cations (two thirds versus one third of the total capacity, respectively).

XPS was a key technique in the observation of the evolution of oxygen redox along the cycles, as well as the obtained oxidation state of Ni during charge and discharge process confirmed with XANES. Raman spectroscopy combined with DFT calculation show for the first time evidences of the formation of true peroxo species  $(\text{O}_2)^{2-}$  stabilised by the presence of  $5d^0 \text{W}^{6+}$  cations (also confirmed with HAXPES measurements). This results in a good reversibility of the anionic redox process after the first activation cycle, with however a very large voltage hysteresis between charge and discharge that we attribute to the difficulty in reducing stabilised  $(\text{O}_2)^{2-}$  species, highlighting the importance of balancing oxygen oxidation with enabling reversing it. Such findings can be generalised to other  $d^0$  containing Li-rich rocksalt oxides, which also struggle with large voltage hysteresis and low energy efficiency, although the origin of this issue had not been investigated until now.

To conclude, it is expected that this work could be very useful in a near future in defining new strategies to decrease the voltage hysteresis and bring high capacity rocksalt oxides closer to potential applications.

## **5.6. References**

1. E. Zvereva, *Dalton Trans.*, 2013, **42**, 1550.
2. A. Gupta, V. Kumar and S. Uma, *J. Chem. Sci.*, 2015, **127**, 225-233.
3. N. Bhardwaj, A. Gupta and S. Uma, *Dalton Trans.*, 2014, **43**, 12050-12057.
4. T. K. Mandal and J. Gopalakrishnan, *Chem. Mater.*, 2005, **17**, 2310-2316.
5. M. H. Dickman and M. T. Pope, *Chem. Rev.*, 1994, **94**, 569-584.
6. G. Amato, A. Arcoria, F. P. Ballistreri, G. A. Tomaselli, O. Bortolini, V. Conte, F. Di Furia, G. Modena and G. Valle, *J. Mol. Catal.*, 1986, **37**, 165-175.
7. R. Stomberg, *J. Less Common Met.*, 1988, **143**, 363-371.
8. M. Grzywa, W. Łasocha and D. Rutkowska-Żbik, *J. Solid State Chem.*, 2009, **182**, 973-982.
9. B. Ravel and M. Newville, *J. Synchrotron Radiat.*, 2005, **12**, 537-541.
10. B. V. Crist, *Handbook of Monochromatic XPS Spectra, The Elements of Native Oxides*, Wiley-VCH, 2000.
11. B. Pecquenard, S. Castro-Garcia, J. Livage, P. Y. Zavalij, M. S. Whittingham and R. Thouvenot, *Chem. Mater.*, 1998, **10**, 1882-1888.
12. E. Holmström, W. Olovsson, I. Abrikosov, A. Niklasson, B. Johansson, M. Gorgoi, O. Karis, S. Svensson, F. Schäfers and W. Braun, *Phys. Rev. Lett.*, 2006, **97**, 266106.
13. M. Gorgoi, S. Svensson, F. Schäfers, G. Öhrwall, M. Mertin, P. Bressler, O. Karis, H. Siegbahn, A. Sandell, H. Rensmo, W. Doherty, C. Jung, W. Braun and W. Eberhardt, *Nucl. Instrum. Methods Phys. Res., Sect. A*, 2009, **601**, 48-53.
14. F. Schaefer, M. Mertin and M. Gorgoi, *Rev. Sci. Instrum.*, 2007, **78**, 123102.
15. M. Mohai, *Surf. Interface Anal.*, 2004, **36**, 828-832.

***Chapter 5. Electrochemical and surface behaviour of Li-rich nickel tungsten oxides***

---

16. R. Cavell, S. Kowalczyk, L. Ley, R. Pollak, B. Mills, D. Shirley and W. Perry, *Phys. Rev. B*, 1973, **7**, 5313.
17. N. J. Campbell, A. C. Dengel, C. J. Edwards and W. P. Griffith, *J. Chem. Soc., Dalton Trans.*, 1989, 1203-1208.
18. J. Horsley, I. Wachs, J. Brown, G. Via and F. Hardcastle, *J. Phys. Chem.*, 1987, **91**, 4014-4020.
19. Z. N. Taylor, A. J. Perez, J. A. Coca-Clemente, F. Braga, N. E. Drewett, M. J. Pitcher, W. J. Thomas, M. S. Dyer, C. Collins, M. Zanella, T. Johnson, S. Day, C. Tang, V. R. Dhanak, J. B. Claridge, L. J. Hardwick and M. J. Rosseinsky, *J. Am. Chem. Soc.*, 2019, **141**, 7333-7346.
20. M. Sathiya, K. Ramesha, G. Rouse, D. Foix, D. Gonbeau, K. Guruprakash, A. Prakash, M. Doublet and J.-M. Tarascon, *Chem. Commun.*, 2013, **49**, 11376-11378.
21. K. Luo, M. R. Roberts, R. Hao, N. Guerrini, D. M. Pickup, Y.-S. Liu, K. Edström, J. Guo, A. V. Chadwick and L. C. Duda, *Nat. Chem.*, 2016, **8**, 684.
22. G. Assat and J.-M. Tarascon, *Nat. Energy*, 2018, 1.
23. J. R. Croy, K. G. Gallagher, M. Balasubramanian, Z. Chen, Y. Ren, D. Kim, S.-H. Kang, D. W. Dees and M. M. Thackeray, *J. Phys. Chem. C*, 2013, **117**, 6525-6536.
24. G. Assat, D. Foix, C. Delacourt, A. Iadecola, R. Dedryvère and J.-M. Tarascon, *Nat. Commun.*, 2017, **8**, 2219.
25. G. Assat, A. Iadecola, C. Delacourt, R. m. Dedryvère and J.-M. Tarascon, *Chem. Mater.*, 2017, **29**, 9714-9724.

# Chapter 6.

## Conclusions and further work

*“Always look on the bright side of life.”*

*Life of Brian*

A study of different positive electrode materials for Li-ion batteries have been provided along this thesis, and the structure, surface and electrochemical properties could be linked each other to understand the behaviour of these compounds.

Different synthetic routes for  $\text{LiCo}_{1/3}\text{Ni}_{1/3}\text{Mn}_{1/3}\text{O}_2$  were studied in **Chapter 3**, and the electrochemical characterisation showed different capacities directly related with the used synthesis. The use of different characterisation techniques, especially XPS, helped to provide an answer about why resorcinol-formaldehyde sol-gel polymerisation had the best electrochemical performance compared with the rest of the samples. SEM images showed that there is a direct relationship between the capacity and the particle size, concluding that the capacity improves with the decrease of the particle size. Sol-gel samples turned out to be very stable in the surface due to their small particles and narrow distribution, and they react less with humidity and carbon-based compounds that form part of the air.

In future measurements, it is recommended to synthesise fresh samples using both the co-precipitation and sol-gel synthetic methods, but with a better control in the



environment during the formation of the final product and heating the samples at high temperatures with pure O<sub>2</sub> gas that is not contaminated with either moisture or carbonates. This would likely result in better capacities, especially in the case of the co-precipitation samples, because the formation of the passivation layer could be avoided or, at least, reduced.

The study of Li-rich compounds in *Chapter 4* showed a very different behaviour according to the crystal structure that is formed for each sample. The different stoichiometry for each other (despite the used synthetic route is the same) showed that Li<sub>1.2</sub>Ni<sub>0.13</sub>Mn<sub>0.54</sub>Co<sub>0.13</sub>O<sub>2</sub> is more anion redox active than Li<sub>1.2</sub>Ni<sub>0.32</sub>Mn<sub>0.4</sub>Co<sub>0.08</sub>O<sub>2</sub> and therefore the electrochemical performance is much better.

A detailed XPS analysis showed that oxygen has an important redox activity for Li-rich materials, and an important evolution of oxygen at different states of charge and discharge could be observed for Li<sub>1.2</sub>Ni<sub>0.13</sub>Mn<sub>0.54</sub>Co<sub>0.13</sub>O<sub>2</sub>. However, this is not the same for Li<sub>1.2</sub>Ni<sub>0.32</sub>Mn<sub>0.4</sub>Co<sub>0.08</sub>O<sub>2</sub>, where the most of the redox activity is coming from Ni and Co and that explains the lower capacity for this last compound.

The possible observation of oxidised O<sup>•-</sup> for Li<sub>1.2</sub>Ni<sub>0.13</sub>Mn<sub>0.54</sub>Co<sub>0.13</sub>O<sub>2</sub> in *ex situ* Raman has to be studied more in detail in future measurements to make sure that this observed bond is indeed the expected O-O stretching bond. Additional computational calculations using density functional theory (DFT) technique can be developed in order to confirm that we have a real O-O stretching bond, as well as *in situ* Raman measurements to observe the same behaviour than in *ex situ* Raman studies. HAXPES measurements could also be a good option in order to confirm that oxygen redox activity takes place in the bulk and not only in the surface, as well as XANES measurements to

## **Chapter 6. Conclusions and further work**

---

confirm the oxidation state of the transition metals at different stages of charge and discharge.

Finally, a new family of Li-rich rocksalt oxides was studied in *Chapter 5*, with special attention in the case of  $\text{Li}_{4.15}\text{Ni}_{0.85}\text{WO}_6$  compound. Apart from the usual studies of the capacity and other lab-based characterisation techniques, the use of synchrotron energy techniques such as XANES and HAXPES were used, and a detailed study for this material was done.

The combination of XANES and XPS studies could confirm that Ni cannot be oxidised beyond  $\text{Ni}^{3+}$  and W is not redox active, concluding that the most of the capacity for this material is coming from oxygen redox activity. Raman spectroscopy could identify the presence of O-O peroxy bonds in the structure of the material. Despite the HAXPES data was affected by contaminants, similar trends were observed that support the formation of peroxide. However, future works include the careful repetition of the HAXPES measurements.

For the samples synthesised by myself, resorcinol-formaldehyde sol-gel polymerisation was found to be the optimum synthetic method to produce materials with superior electrochemical performance. Their simplicity consists in a relatively quick polymerisation and less control in the formation of their intermediates than other techniques and the final product have nanoparticles of considerable homogeneity and stability, as well as a stable surface that is responsible for their high capacity. In spite of their good electrochemical performance, sol-gel synthesis has some challenges that need to be solved in order to be reproduced in a big scale for their commercialisation: the fact that one of their steps during the synthesis implies a calcination of the samples in order to eliminate carbon-based compounds would give place to the production of a big amount

of CO<sub>2</sub> gas. For commercial purpose, there exist the possibility to apply different methods to trap CO<sub>2</sub> and other hydrocarbon gases in order to avoid their emission to the atmosphere, and some of these methods even allow to recycle these gases for other synthetic procedures.

These studied materials are a real option to be applied in the next generation of commercial batteries. LiCo<sub>1/3</sub>Ni<sub>1/3</sub>Mn<sub>1/3</sub>O<sub>2</sub> presents good electrochemical performance and it is relatively cheap to synthesise. However, Li<sub>1.2</sub>Ni<sub>0.13</sub>Mn<sub>0.54</sub>Co<sub>0.13</sub>O<sub>2</sub> is the best option to be used as cathode in a commercial battery due to its high capacity and stability, as well as a good voltage window. Li<sub>1.2</sub>Ni<sub>0.32</sub>Mn<sub>0.4</sub>Co<sub>0.08</sub>O<sub>2</sub> presents a lower capacity compared to Li<sub>1.2</sub>Ni<sub>0.13</sub>Mn<sub>0.54</sub>Co<sub>0.13</sub>O<sub>2</sub> but future studies and the use of alternative synthetic routes can help to obtain a better electrochemical performance.

In the case of Li<sub>4.15</sub>Ni<sub>0.85</sub>WO<sub>6</sub> compound, although it has a very similar capacity than Li<sub>1.2</sub>Ni<sub>0.13</sub>Mn<sub>0.54</sub>Co<sub>0.13</sub>O<sub>2</sub>, the high cost of tungsten, the large voltage window and the large hysteresis due to the difficulty of reducing back the oxygen causes the impossibility to be applied in commercial batteries, although this material can be used as a reference (and even a precursor) in the future development of high-energy commercial Li-ion batteries.



# CURRICULUM VITAE

José Antonio Coca Clemente

## Personal

Date of birth: 11/11/1987

Place of birth: Mazarrón (Spain)

Nationality: Spanish

Email: coka87@gmail.com

## Education

<b>2019 - Current</b>	<b>Post-doc position in Energy Storage.</b> <b>CIC Energigune, Spain</b> <b>Project title:</b> Formation of artificial SEI layer to protect Li metal anodes in Li-S batteries <b>Supervisor:</b> Miguel Ángel Muñoz
<b>2015 – 2019</b>	<b>PhD Degree in Energy Storage.</b> <b>University of Liverpool, UK</b> <b>Project title:</b> Electrochemical and Surface Study of novel lithium metal oxides used as cathodes in lithium-ion batteries <b>Supervisors:</b> Prof. Laurence J. Hardwick, Prof. Vinod R. Dhanak
<b>2014 – 2015</b>	<b>Master Degree in Electrochemistry, Science and Technology.</b> <b>University of Murcia, Spain</b> <b>Project title:</b> Multistep charge transfer reactions of surface confined polyoxometalates. Influence of the electrode in bromate catalysis <b>Supervisor:</b> Prof. Joaquin Gonzalez
<b>2005 – 2014</b>	<b>Bachelor Degree in Chemistry.</b> <b>University of Murcia, Spain</b> <b>Experience:</b> Research student in Inorganic Chemistry Department

## Publications

- Taylor, Zoe N., *et al.* “Stabilization of O-O bonds by  $d^0$  cations in  $\text{Li}_{4+x}\text{Ni}_{1-x}\text{WO}_6$  ( $0 \leq x \leq 0.25$ ) rocksalt oxides as the origin of large voltage hysteresis” *Journal of the American Chemical Society*, 2019, **141**, 7333-7346. (Chapter 5)

- Graham, Michael, *et al.* "Nanoencapsulated crystalhydrate mixtures for advanced thermal energy storage." *Journal of Materials Chemistry A* 5.26 (2017): 13683-13691.
- Serwar, Monazza, *et al.* "Template-free synthesis of nitrogen doped carbon materials from an organic ionic dye (murexide) for supercapacitor application." *RSC Advances* 7.86 (2017): 54626-54637.

### Conference attendance and presentations

#### ➤ 2019

- ❖ Oral Communication at 235th ECS Meeting, Dallas: "Anionic redox in Li-rich rocksalt oxides studied via X-ray photoelectron spectroscopy"

#### ➤ 2018

- ❖ Oral Communication at Electrochem 2018, Lancaster: "Study of the surface and electrochemical properties of novel lithium intercalation compounds used as cathodes in Li-ion batteries"
- ❖ Oral Communication at XXXIX Reunión del Grupo de Electroquímica de la Real Sociedad Española de Química, Madrid: "Study of the surface and electrochemical properties of novel lithium intercalation compounds used as cathodes in Li-ion batteries"

#### ➤ 2017

- ❖ Oral Communication at ECS Northwest Student Chapter Conference, Liverpool: "Effect of the synthetic routes on the surface properties and electrochemical performance of  $\text{LiNi}_{1-x-y}\text{Co}_x\text{Mn}_y\text{O}_2$ "
- ❖ Poster at 13<sup>th</sup> International Conference on Materials Chemistry (MC13), Liverpool: "Effect of the synthetic routes on the surface properties and electrochemical performance of  $\text{LiNi}_{1-x-y}\text{Co}_x\text{Mn}_y\text{O}_2$ "

#### ➤ 2016

- ❖ Poster at Energy Materials Symposium 2016, Bath: "An investigation into electrochemical and surface properties of lithium manganese mixed metal oxides"
- ❖ Oral Communication at XXXVII Reunión del Grupo de Electroquímica de la Real Sociedad Española de Química, Alicante: "An investigation into electrochemical and surface properties of lithium manganese mixed metal oxides"
- ❖ Poster at U.K. Northwest ECS Student Chapter Summer Symposium, Manchester: "An investigation into electrochemical and surface properties of lithium manganese mixed metal oxides"